683 | Juni 2015

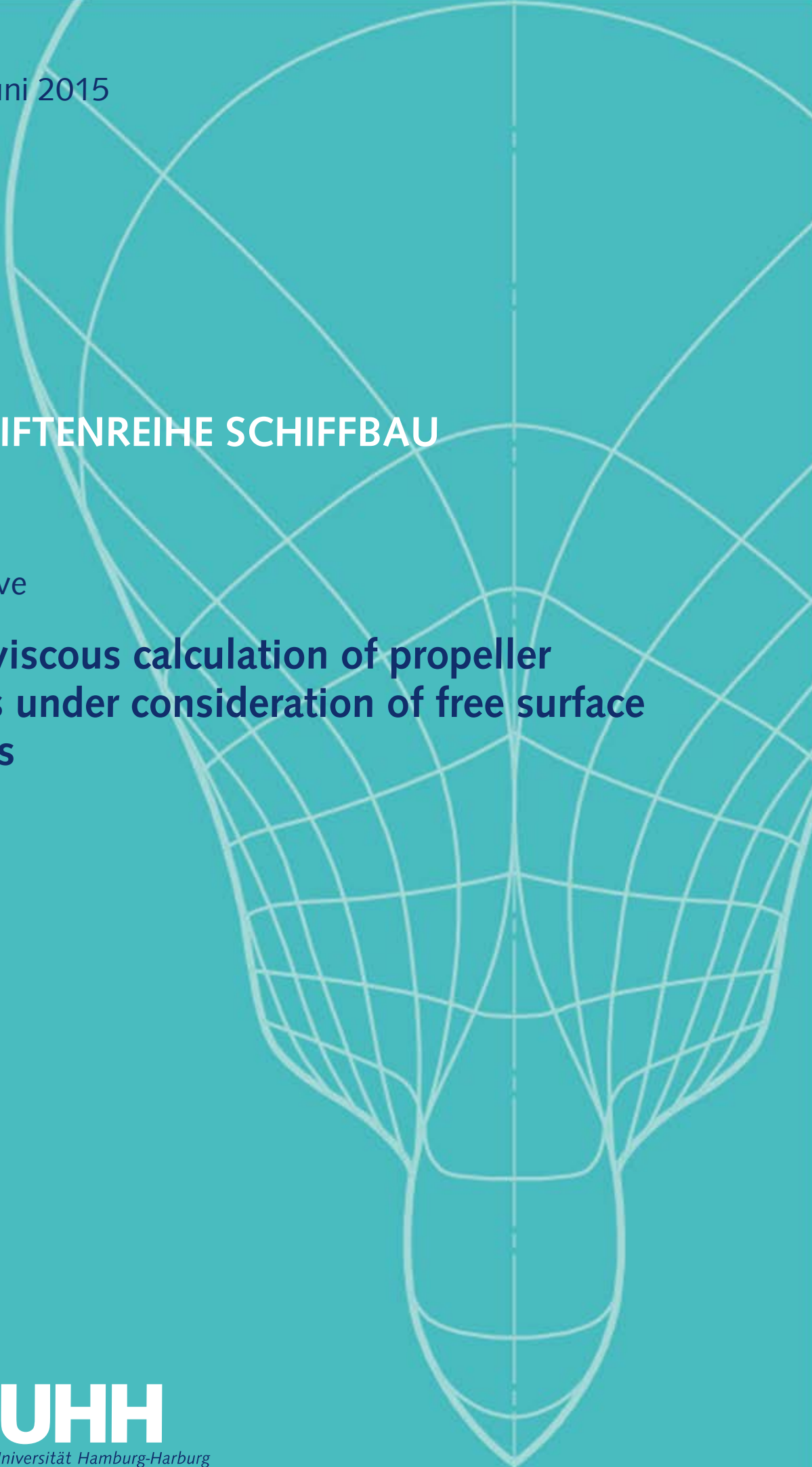

SCHRIFTENREIHE SCHIFFBAU

M. Greve

Non-viscous calculation of propeller forces under consideration of free surface effects

TUHH
Technische Universität Hamburg-Harburg

Non-viscous calculation of propeller forces under consideration of free surface effects

Vom Promotionsausschuss der
Technischen Universität Hamburg-Harburg

zur Erlangung des akademischen Grades

Doktor-Ingenieur (Dr.-Ing.)

genehmigte Dissertation

von
Martin Greve

aus
Halle/Saale

2015

Vorsitzender des Prüfungsausschusses
Prof. Dr.-Ing. Friedrich Wirz

Gutachter
1. Gutachter: Prof. Dr.-Ing. Moustafa Abdel-Maksoud
2. Gutachter: Prof. Dr.-Ing. Stefan Krüger
3. Gutachter: Prof. Dr.-Ing. Sverre Steen

Zusätzliche Gutachter
Prof. Dr.-Ing. Friedrich Wirz
Prof. Dr.-Ing. Heinz Herwig

Tag der mündlichen Prüfung
12. Juni 2015

Technischen Universität Hamburg-Harburg
Schwarzenbergstraße 95C
D-21073 Hamburg
http://www.tuhh.de/vss

Bericht Nr. 683
ISBN 978-3-89220-683-5

Abstract

This thesis addresses the issue of determining dynamic loads acting on propellers based on potential theory simulations. In particular, the focus is set on loads due to free water surface influences resulting from a shallow propeller immersion and due to ventilation when the propeller is only partly wetted. This situation occurs e.g. when vessels are supplying offshore platforms, which are usually relatively small and therefore ship motions can be large. Moreover, these vessels often operate in harsh weather conditions and also may operate in dynamic positioning mode. The resulting loads on a ventilating propeller can lead to mechanical failures of the propulsion system because the thrust and torque evolution shows large amplitudes.

The development of numerical methods follows a two-way approach. The first approach begins with purely potential simulations starting with a *BEM* for submerged bodies, in which the boundary conditions at the free water surface are introduced with different numerical implementations for the steady and the unsteady case. In the steady case, the kinematic and dynamic boundary conditions are combined and solved at the same time, whereas they are solved separately in the unsteady case by applying a numerical time-stepping scheme. The second approach is a hybrid method which is based on the coupling of a *BEM* and a *RANSE* solver. In this approach, the propeller forces are computed by the *BEM* under consideration of the viscous velocity distribution present in the *RANSE* domain. The propeller forces are computed by the *BEM* and act as a field of body forces distributed on the grid cells in the *RANSE* computation domain. The simulation method is capable of representing the three-dimensional propeller geometry and the actual blade positions.

The thesis gives insight into the flow phenomena occurring at a propeller in operating conditions and provides a literature survey on numerical methods that have been developed and experimental campaigns that have been conducted so far. This is followed by a discussion on the numerical methods and free water surface models applied. A comprehensive validation of the baseline methods with a concentration on propellers, unsteady effects and free water surface influences is given. The last section offers two application examples for propellers operating shallowly immersed in calm water and in waves. Comparisons are made towards experimental data obtained by *MARINTEK*.

Acknowledgements

This work was carried out during my engagementat the Institute for Fluid Dynamics and Ship Theory at Hamburg University of Technology. I would like to express my gratitude to my advisor Professor Moustafa Abdel-Maksoud for giving me the opportunity for this research work, for providing helpful discussions and suggestions and for always supporting and encouraging me. I would further like to acknowledge Professor Sverre Steen and Professor Stefan Krüger for beeing assessors of my thesis and Professor Friedrich Wirz for chairing the doctoral examination.

I would like to thank the norwegian partners in the *PropSeas* research project, namely Professor Sverre Steen from the Norwegian University of Science and Technology, Dr. Kourosh Koushan from Marintek and Dr. Hamid Amini for their generosity of providing me with most of the experimental data used in this work. The German federal Ministry of Economics and Technology is acknowledged for sponsoring my research work.

Furthermore I acknowledge my colleagues at FDS and the *pan*MARE group for creating an inspiring athmosphere on the fifth floor. The valuable contributions of the students Stephan Berger, Ulf Göttsche, Markus Pergande, Martin Scharf and Sebastian Sturm to various parts of this work are acknowledged.

I would particularly like to thank my wife Anna for her confidence and encouragement during the years of my dissertation.

Kiel, July 2015
Martin Greve

Contents

List of Symbols

In the following not all symbols employed are listed. Any notation not described here will be explained where it is first used. Time derivatives of quantities can be identified by a dot above the symbol. Tensor quantities are written in fat Latin letters, where small letters refer to vectors and large to matrices. The Kronecker delta δ_{ij} is used.

Latin Letters

$\hat{A}_w$	$[m]$	wave amplitude
A	$[m^2]$	surface area
C	$[\frac{m^2}{s^2}]$	constant in Bernoulli equation
c	$[m]$	chord length of a hydrofoil
D	$[m]$	propeller diameter
D_h	$[m]$	propeller hub diameter
F_d	$[N]$	drag force of a hydrofoil
F_l	$[N]$	lift force of a hydrofoil
f_y	$[N]$	propeller horizontal force (in ship-fixed coord. sys.)
f_z	$[N]$	propeller vertical force (in ship-fixed coord. sys.)
f_i	$[N]$	components of force vector
H	$[m]$	static propeller immersion
h	$[m]$	water depth
H_w	$[m]$	wave height
k		wave number, $k = \frac{2\pi}{L_w}$
L_w	$[m]$	wave length
m	$[kg]$	mass of a fluid inside a control volume
m_y	$[Nm]$	propeller horizontal moment around the y-axis (in ship-fixed coord. sys.)
n	$[\frac{1}{s}]$	propeller rotation rate
n_j	$[m, m, m]$	components of normal vector
P	$[m]$	propeller pitch
p	$[\frac{N}{m^2}]$	pressure
Q	$[Nm]$	propeller torque
R	$[m]$	propeller radius
r	$[m]$	distance between two points

R_w	$[N]$	wave resistance
S	$[m^2]$	surface area
S_ζ	$[\frac{m^2 s}{rad}]$	wave energy spectrum
T	$[N]$	propeller thrust
t	$[s]$	time
T_w	$[s]$	wave period
u, v, w	$[\frac{m}{s}]$	components of the velocity vector in the global Cartesian coord. sys.
V	$[m^3]$	volume
v_i	$[\frac{m}{s}]$	components of velocity vector
x, y, z		coordinate directions in the global Cartesian coord. sys.
z_p		number of propeller blades
$\mathbf{E}$	$[J]$	energy
$\mathbf{f}$	$[N, N, N]^T$	force vector
$\mathbf{n}$	$[m, m, m]^T$	normal vector of a surface
$\mathbf{v}$	$[\frac{m}{s}, \frac{m}{s}, \frac{m}{s}]^T$	vector of velocity

Greek Letters

α	$[^\circ]$	exemplary variable operator
ϵ		error rate
η_o		propeller open water efficiency, $\eta_o = \frac{K_T}{K_Q}\frac{J}{2\pi}$
Γ	$[\frac{m^2}{s}]$	circulation
γ	$[^\circ]$	direction angle of a long-crested wave
γ_0	$[^\circ]$	propagation direction of a seaway
λ		scale factor
μ	$[\frac{m^4}{s}]$	doublet strength
ω	$[\frac{rad}{s}]$	wave angular frequency
Φ	$[\frac{m^2}{s}]$	total potential
Φ_M	$[\frac{m^2}{s}]$	motion potential
Φ_∞	$[\frac{m^2}{s}]$	potential of undisturbed inflow
Φ_{ind}	$[\frac{m^2}{s}]$	induced potential
ρ	$[\frac{kg}{m^3}]$	density
σ	$[\frac{m^3}{s}]$	source strength
τ	$[^\circ]$	phase shift angle for a wave in a wave spectrum
τ_{ij}	$[Pa]$	tensor of shear stress
θ	$[^\circ]$	propeller skew angle
φ	$[^\circ]$	angular propeller blade position
ξ, η, ψ		coordinate directions in the local Cartesian coord. sys.

ζ	$[m]$	free surface elevation (positive upwards)

Coefficients

c_d	drag coefficient, $c_d = \frac{D}{0.5\rho v^2 A}$
c_f	friction drag coefficient, $c_f = \frac{R_f}{0.5\rho v^2 A}$
c_l	lift coefficient, $c_l = \frac{L}{0.5\rho v^2 A}$
c_p	pressure coefficient, $c_p = \frac{p}{0.5\rho v^2}$
c_r	Courant number, $c_r = \frac{v \cdot \Delta x}{\Delta t}$
c_w	wave drag coefficient, $c_w = \frac{R_w}{0.5\rho v^2 A}$
c_{th}	propeller thrust loading coefficient, $c_{th} = \frac{T}{0.5\rho v_A^2 A_p} = \frac{K_T}{J^2}\frac{8}{\pi}$
K_Q	propeller torque coefficient, $K_Q = \frac{Q_p}{\rho n_p^2 D^5}$
K_T	propeller thrust coefficient, $K_T = \frac{T_p}{\rho n_p^2 D^4}$
$K_{f,z}$	propeller vertical force coefficient, $K_{f,z} = \frac{f_z}{0.5\rho n_p^2 D^4}$
$K_{m,y}$	propeller horizontal moment coefficient, $K_{m,y} = \frac{m_y}{0.5\rho n_p^2 D^5}$

Sub- and Superscripts

$c.s.$	control surface
$c.v.$	control volume
i, j	indices
x, y, z	coordinate directions

Abbreviations

$b.c.$	boundary conditions
BEM	Boundary Element Method
$BEMT$	Blade Element Momentum Theory
BVP	Boundary Value Problem
CPP	Controllable Pitch Propeller
DP	Dynamic Positioning
EAR	propeller Expanded Area Ratio
$NACA$	National Advisory Committee for Aeronautics
OSV	Offshore Supply Vessel
$RANSE$	Reynolds-Averaged Navier-Stokes Equations

RHS	Right Hand Side
SLE	System of Linear Equations
VLM	Vortex Lattice Method
VoF	Volume of Fluid

1. Introduction

1.1. Motivation

With the large number of computational tools now available, potential-theory based simulation methods are the workhorses in the design of marine propellers today. At the same time, more questions have to be addressed by the designer in order to meet current demands concerning exact load prognosis in off-design conditions. For example, the effect that a propeller faces, when it is working in the vicinity of the free water surface is severe loads. While methods based on the *Reynolds Averaged Navier-Stokes Equations* (*RANSE*) can predict these loads in a quite reliable manner, the setup and simulation effort is large and not well suited for a design process. Therefore, possibilities for the computation of free surface effects acting on propellers using non-viscous, potential based solvers are highlighted within this work.

The effect of the water surface on the propeller loads is non-negligible for relatively small, ocean-going vessels sailing under severe conditions, where the wave amplitudes can be high and large amplitude ship motions can be exited. This is a typical operation situation for offshore supply vessels in transit or dynamic positioning mode. The propeller can operate close to the water surface and even penetrate it. Moreover, when the propeller is part of a thruster propulsion unit, additional loads can arise from the dynamics of the steering operation and especially in the dynamic positioning mode, where the ship motions can also be significant. This multitude of different conditions can cause large loads on the propeller blades, the gearbox, the propeller shaft and, when a controllable pitch propeller is present, to the pitch control mechanism. An in-depth understanding of the different phenomena taking place is fundamental to forecasting a more exact load and to creating an optimal design.

The motivation for the present work is to find a fast and accurate numerical method for the prediction of forces and moments acting on propellers of ships operating in the described harsh conditions. The main subject is to consider the operating conditions of the *Offshore-Supply Vessel* (*OSV*) depicted in Figure 1.1a, which is equipped with two azimuthing thruster units having controllable pitch propellers. One propulsion unit is displayed in Figure 1.1b. The investigations undertaken have been part of *ProSee*, a contribution to the *MARTEC* research project *PropSeas*, sponsored by the German

(a) The ship *Far Searcher* owned by *Farstad Shipping ASA*. Picture is taken from *www.farstad.com*

(b) *Rolls Royce Azipull*. Picture taken from *www.rolls-royce.com/marine*

Figure 1.1.: The objectives in the research project *PropSeas*

Federal Ministry for Economic Affairs and Energy. The cooperation partners within the project are the research institute *MARINTEK*, the Norwegian University of Science and Technology (*NTNU*), the University of Duisburg-Essen (*UDE*), the German Lloyd (now *DNV GL*), the shipping company *Farstad Shipping* and *develogic subsea systems*.

1.2. Present Contributions

Within this work, two main methods for calculating unsteady forces and moments acting on marine propellers under consideration of free surface effects are developed. The first is based on a *Boundary Element Method* (*BEM*) using potential theory. The boundary conditions (b.c.) at the free water surface are implemented, so its deformation can be determined in combination with the forces acting on submerged bodies. A second possibility for taking the free water surface into account in potential theory based simulations is to develop a solver coupling method between a *BEM* and a *RANSE* solver. The *RANSE* method is not presented here in detail as it can be found in Ferziger and Peric [28]. In particular, the description of *FreSCo*$^+$ applied in this study is given in Manzke et al. [69].

With the main aim to compute unsteady loads imposed by an operation in the vicinity of the free water surface, the starting point of this thesis is the surface panel method *pan*MARE, which was basically developed by Hundemer [45]. This methods is a sophisticated tool for determining steady and unsteady propeller forces and turned out to be a good starting point for my investigations.

The following technics are implemented in order to add the free water surface influence:

- The steady free surface boundary conditions are implemented in a combined approach and by twice using a fourth-order upwind scheme. This provides a fast and reliable solution for determining steady wave resistance. The unknown values of the doublet and the source strength are determined in one equation system and the elevation of the free water surface is computed thereafter.

- For the unsteady cases addressed here, the free surface b.c are implemented in an unsteady formulation. This is conducted using a scheme, where the source strength is solved in the main equation system and the doublet strength and the free surface elevation are stepped forward in time using a fourth-order Runge-Kutta method.

- Furthermore, for situations where the free surface boundary conditions are not satisfied and the body does not deform the surface, a wave potential formulation is implemented for incoming waves. As such, the potential and velocity components of long crested waves and wave spectra can be superposed to the perturbation potential of the body and the unsteady wave forces can be solved for in a very efficient manner.

- In situations where a propeller or any other body emerges out of the water, a panel split technique at free water surface is implemented. This refers to a possibility of switching off fully emerged panels and of treating partly emerged panels correctly in terms of the determination of the potential values and the pressure acting on the body. This technic can be applied both in combination with a geometrically modelled free water surface and a superposed wave potential.

- As another method of determining the unsteady propeller forces near the free water surface, a coupling between the *BEM* and a *RANSE* solver is developed. The main work is related to the implementation of the *BEM* solver. In this coupling procedure, the position of the water surface is not determined in the *BEM*, but within the *RANSE* method, where also all other bodies except the propeller are present. The propeller forces are modelled via source terms in the momentum equation and distributed on a number of cells within the *RANSE*

solver in an unsteady, three-dimensional manner, so that even the suction and pressure side of each blade is represented. The velocity distribution in front of the propeller and the water surface position, which is determined from the concentration of the fluids water and air, is transferred from the *RANSE* solver to the *BEM*. The free surface deformation is reconstructed in the *BEM* solution domain from Fourier series and the boundary conditions are fulfilled at its actual postion. The velocity distribution is used in the *BEM* to correctly determine the forces and moments acting on the propeller, so the solver coupling method can also be referred to as a propeller model in the *RANSE* method.

1.3. Outline of the Thesis

This thesis is structured as following:

In **Chapter 2 - Background**, the fundamentals for an understanding of the problems discussed in this thesis are described. These are the physical effects contributing to the unsteady loads acting on a propeller in operating conditions. This is followed by a literature review on the state of the art in unsteady numerical procedures for the determination of the above mentioned loads and experimental campaigns conducted in order to measure them.

Chapter 3 - Computational Model describes the basic equations for the potential flow model and the derivation of the free water surface boundary conditions. The solution method using a *BEM* is described and details of the numerical implementation are presented. This information is also given for the solver coupling method.

Chapter 4 - Validation and Verification provides various simulation cases in which the applicability of the method for the problems mentioned above is demonstrated. The focus of this chapter is to present different requirements, such as the computation of lift-, propeller-, wave- and water surface-forces separately.

Two main simulation campaigns are presented in **Chapter 5 - Applications**. These are shallowly immersed propellers in an open water setup and those operating in additionally imposed long-crested waves. For both campaigns comparisons to experimentally determined thrust forces are conducted.

In **Chapter 6 - Conclusions**, a short summary, a review on the presented results and an outlook to a possible continuation of the work is given.

2. Background

In this chapter the main aspects addressed in the present work shall be presented. First, a discussion on the theoretical background is given, where the single physical conditions contributing to the effects occurring at a ship propeller in operating conditions are considered separately. The second part offers a brief historical review and presentation of the state of the art of numerical methods for the computation of propeller flows. The last part gives examples for experimental campaigns conducted to determine unsteady loads acting on propellers. These include open propellers, thrusters and pods in open water conditions, in inclined inflow, motions and in waves.

2.1. Loads Acting on a Propeller in Operating Conditions

When a ship propeller is operating, many physical aspects contribute to the forces acting on it. If a propeller-fixed coordinate system is considered, all influences on the flow field affect the inflow to the propeller, which is highly unsteady for an operation at a ship which itself moves in a seaway. In this section the flow characteristics of ship propellers shall be described including all influences occurring in operation conditions. The geometric properties of propellers will not be discussed here; for further information the publications by Carlton [20] or Krüger [63] can be consulted. First, the flow conditions of a propeller in an open water test situation will be explained. This case is often simplified to a two-dimensional hydrofoil, when cylindrical blade sections are investigated because the flow field and the resulting forces and moments occurring at a hydrofoil are similar to the forces and moments at a propeller as the flow at a propeller blade is directed tangentially for large parts of the surface. Based on this knowledge, an expansion of the flow conditions will be given for propellers subjected to an unsteady flow situation when operating as the prime mover of surface ships without the influence of a free water surface. This again will be extended to the effects occurring at the propeller when the free water surface is taken into account. These are driven by the wave elevation and hence the motions of the ship. Furthermore, loads due to steering or - in extreme situations - ventilation of the blades can occur. In the last part of this section, an introduction on the loads acting on propellers within the described flow situations

and on the supporting structures, such as the shaft or thruster housings and struts is given.

Steady flow appears at a ship propeller when it is subjected to a constant inflow, which only can be achieved when neither a ship nor any other obstacle disturbs the flow field in front of it, and further, when the shaft is parallel to the inflow towards the propeller. This situation is generated at an open water test, which is conducted - often in line with simulations - for every propeller prior to its casting in order to provide basic insight into its performance. The geometry of the model propeller is similar, but smaller than the original by the scale factor λ. Often the model test is conducted at a constant propeller rotation rate and different propeller loadings, characterised by the advance ratio J, which are achieved by altering the inflow velocity. The rotation rate of the model scale propeller is chosen to be higher than those of the full scale in order to take into account the scale effects. A description of the similarity laws and a possible correction method for the scale effects is described by Kornev [57] (sec. 4.1). A measure for the propeller loading is the thrust loading coefficient c_{th}, which relates the actual thrust to the stagnation pressure, which corresponds to the advance velocity, times the propeller disc area.

A ship propeller is in general a three-dimensional hydrofoil with varying geometric properties and angle of attack over the blade radius. Therefore, the main physics of the flow and the work principle are often explained using radial propeller sections. These can be seen as two-dimensional hydrofoils operating at a prescribed angle of attack, which is determined by the pitch at the adjacent radius and is constant in the case of the propeller in open water conditions. As a result of the angle of attack and camber, a force applies at the profile, which has a portion of lift and drag, corresponding to the forces perpendicular to and in the direction of the undisturbed inflow. The velocity vector of undisturbed inflow is dependent on the rotation rate and advance speed. The portion of the resulting force acting in the propeller axis direction is the propeller thrust and the moment acting around the propeller axis and resulting from the tangential force is the propeller torque. Both are normally non-dimensionalised by the fluid density, the rotation rate and the propeller diameter resulting in the thrust (K_T) and torque coefficient (K_Q). An open water diagram can be produced from open water tests showing the propeller thrust and torque without the presence of a ship hull. Using the open water test setup, the open water efficiency η_O is determined and used to develop the optimum propeller under consideration of other constraints.

When the open water characteristics of *Controllable Pitch Propellers* (*CPP*) are observed, multiple curves for K_T, K_Q and η_O can be plotted and, considering Carlton [20], interpreted as a surface in the open water diagram on which the propeller can operate. Each of the curves belongs to a propeller pitch angle. An additional design constraint for a *CPP* is the spindle torque of the actuating mechanism, which has to be

(a) Deeply immersed propeller at the still-standing ship

(b) Ventilating propeller during ship operation in crossing seaway

Figure 2.1.: Figures from the *MARINTEK* experimental campaign within *PropSeas* (unpublished)

held up in order to keep the blade in its position and overcome by the hydraulic system for changing the pitch setting.

When the propeller is operating at a ship in behind condition, the inflow to the propeller is in any case non-uniform and the forces are unsteady per definition. The unsteadiness can be caused by several factors. One, accounting for every ship propeller is the ship hull being situated either directly in front of the propeller for conventional propeller arrangements or at some distance in the case of a pod or thruster application. Due to the possible operation in pulling or in pushing mode, the thruster housing and strut can contribute significantly to the non-uniformity of the inflow in the latter case. A typical situation of a thruster propulsor at an *OSV* is displayed in Figure 2.1a. Additional unsteadiness can be imposed by an inclined inflow to the propeller, which can be caused by the hull geometry, a shaft inclination or a manoeuvring ship.

For the propeller operating in a non-uniform inflow situation, again it is helpful to study the influences on a two-dimensional blade section of constant radius. In this situation, the effect can be divided into a fluctuation of the axial and tangential velocity components, which both contribute to a change of the hydrodynamic attack angle of the profile. When the axial velocity reduces, or the tangential increases, the angle also increases in line with the load of the propeller. This is the case for a smaller advance velocity or an increased rotation rate of the propeller. When the propeller alone is subjected to surface wave influences, two effects are dominant. The first is a dynamic change of immersion and the second - being more important for the non-ventilating

propeller loads - are the wave orbital velocities. They can be significantly high, e.g. in the range of $15 - 20\%$ of the ship speed for an OSV ($L = 80m, v = 14kn, H_W = 2m$) in simulations conducted by Greve et al. [35] for the ship-propulsor combination shown in Figure 2.1, leading to approximate thrust variations of 20%. This value is confirmed by experiments conducted by Koushan et al. [59] for a free running thruster model in waves.

When the propeller operates behind a ship, the static and dynamic behaviour in oblique inflow is of particular interest. The first is due to the fact that the flow is in general inclined in the propeller position due to the above-mentioned reasons. The second is of interest because of the ship motions and of the wave orbital velocities. An inclined inflow affects the propeller operation and has been subject to studies for a long time. Several experimental studies were carried out in the 1920s and 1930s for ship and airplane propellers operating in oblique flow. The dominant effects, though, for a ship occur as a result of its motions, mainly the pitch and roll motions. The latter are of minor importance for single screw ships, because the propeller is situated very close to the roll-axis. The ship motions lead to highly dynamic changes of the inflow conditions and to large changes in the angle of attack of the blade sections. Furthermore, the ship hull geometry, especially at the bow, has an important influence on this behaviour. The ship motions and sea loads lead to an increased ship resistance and a reduced ship speed. Following Carlton [20], the power increase can be up to 8% for a ship in head-waves compared to the calm water case, denoting an increase in propeller loading. This value is also found in model scale experimental results published by Ueno et al. [94] for a $300m$ container ship in regular head waves.

In very rare situations for ocean going ships, due to large amplitude ship motions, the propeller can ventilate, meaning that air is sucked down by its rotating motion or that the propeller even partly emerges out of the water. A situation in which this happens is shown in Figure 2.1b in a model-scale ship. Because the air density is a thousand times smaller than the water density, the forces on the propeller break down suddenly when it or parts of it emerge or ventilate. When the propeller is wetted again a sudden extreme load can occur and serious damage of the propulsion system can result. This is often referred to as *Tooth Interior Fatigue Fracture*[1] (*TIFF*) when it affects gear trains in the gearbox. It is necessary to distinguish between conventional ship propellers, which can ventilate or emerge out of the water in the above-mentioned extreme cases, and surface piercing propellers. The latter are designed for high-speed ships and are only partly wetted during normal operation. They have been subject to numerous experimental and simulation campaigns and will not be treated in this work.

[1] In this context, a simulation of the fluid mechanics is pursued. A description of the mechanical failure mode, which is reported to occur at thruster propeller gears according to Califano [16], is given by MackAldener [68].

When the unsteady loads on thruster or pod propellers due to the azimuthing of the device for steering operations at slow ship speeds are to be determined, additional effects must be considered. Following paper V in Amini [3], this case is more important when designing the thruster gearbox than the ship motions at normal cruising speed because of extreme loads occurring at the azimuthing thruster. The dynamic force fluctuations are larger for the thruster side forces and moments than for thrust and torque of the device. This also imposes large loads on the bearings of the propeller hub.

2.2. State of the Art in Numerical Procedures

The fundamental equations for fluid dynamics are the conservation equations for momentum, mass and energy. From these, several numerical simulation methods for propellers had been developed while the methods required very low computational costs with the absence of a personal computer before the 1950s. After that, more sophisticated models were established, including the *BEM* and *RANSE* solvers used within this work. A comprehensive overview on the history of propeller methods and theories is given by Carlton [20] and will not be discussed here in detail. This section gives a brief historical review on the development of Boundary Element Methods, focusing on ship propeller and free surface applications. Therefore, the propeller forces must be computed in an unsteady flow field. Examples are given for developments in unsteady propeller simulation tools and those accounting for free surface effects, followed by a presentation of further work related to ventilation of propeller blades. For these applications a solver coupling method between the *BEM* and a *RANSE* solver is established in order to account for the propeller action using the *BEM* propeller forces in the *RANSE* domain. An overview will be given on similar coupling methods that have been developed in the past.

Boundary element methods make use of the surface integral formulation of the conservation equations in a potential flow field. The first three-dimensional methods were developed for airplane applications and the groundwork was laid out by Hess and Smith [42] in the 1960s for non-lifting bodies using a source distribution. Later, the problem of lifting bodies was addressed by Hess [41], who first uses a source and dipole distribution on the surface of a body compared to the previously used vortex distribution on the mean camber line of airfoils, making it possible to determine the induced lift and drag. The early approaches address a steady flow situation of an airfoil moving in unbounded fluid. The first *BEM*s for propeller applications were developed in the 1980s by Hess and Valarezo [43] and by Kerwin et al. [52]. This work was further extended in the 1990s in the research group of Prof. Kinnas at the University of Texas (see e.g. [54], [53] and [55]) and also several other groups. Models for unsteady flow (see Hsin [44] or

Fine [29]), cavitation (see e.g. Kinnas and Young [56]) and surface-piercing propellers (see Young [100]) were subsequently developed.

As the flow at marine propellers is mostly lift-driven, the results computed with a *BEM* are realistic for moderately loaded conventional propellers. Differences occur at high loadings when frictional effects become more important and leading edge separation can occur. These effects are reported by Koyama [61] and an in-depth investigation on the result quality of a *BEM* is given by Caponnetto and Rolla in [18] and [19], where the effects on the propeller thrust and torque are discussed separately. Also, when the propeller geometry is more unconventional, e.g. having high skew angles or very thin profiles, the contribution of frictional effects is more pronounced. This leads to mandatory extensions of the purely potential model. Several aspects, such as frictional forces according to a skin friction formula, the influence of a propeller hub, leading edge separation as discussed by Hsin [44] and boundary layer (see Takinaci and Atlar [92]), can be addressed. For a propeller, the modelling of the trailing wake sheet is of major importance. The strength of the singularity distribution in the wake is determined by a Kutta condition, but also other numerical effects contribute significantly to the result. These are related to discretisation issues, the wake sheet length, the modelling of the propeller tip geometry and the method of deforming the wake panels in the trailing velocity field. A comprehensive investigation of several influences on the result quality is given by Greco et al. [32]. Also, the methodology of applying the Kutta condition can be quite different if a linear form, as introduced by Morino and Kuo [70] or an iterative form as proposed by Kerwin et al. [52], which takes cross-flow on the blade into account, is chosen. The implementation is furthermore different for steady and unsteady cases.

For calculating the forces and moments acting on propellers operating in unsteady conditions as discussed in Section 2.1, several developments have been made in *BEM*s. This subject has been recently addressed in the literature because of ships equipped with thruster drives. For example, *OSV*s, which often operate in severe weather conditions and hence are confronted with large amplitude ship motions and highly unsteady propeller forces and moments. Moreover, the propellers - which can be of pulling or pushing type - are often subjected to an inclined inflow when the ship is steering or in dynamic positioning (DP) mode. These aspects are considered in several numerical investigations, often conducted with *RANSE* solvers. The setup and simulation time of this type of simulation can be tremendous, but the results show promising agreement to experimental data, as shown by Carrica et al. [21] and by several research groups at the Gothenburg 2010 CFD workshop [64] for complete ship-propulsor-combinations. Another challenge is the high cost of simulations because wide range of time-scales and multiple-domain grid approaches, such as sliding or overlapping techniques, are needed to simulate the relative motion between the propeller and the non-rotating parts (the ship or a thruster housing). One example is given by Muscari and Di Mascio [72].

Because the frictional contributions to the wake flow cannot be determined with methods based on the potential flow theory, these methods cannot be used for the simulation of propeller flows in behind conditions. Types of problems addressed by *BEM* simulations can be podded propellers subjected to inclined inflow and under heaving motions as presented by Politis [76]. He also conducts an in-depth investigation of the trailing wake deformation process during the dynamic propeller motion. Sharma et al. [84] show results of unsteady simulations for a dynamic azimuthing propeller undergoing surge, roll and heave motions using a *BEM* and a *Vortex Lattice Method* (*VLM*). The dynamic loads acting on a pod-propeller is computed by Liu et al. [67] using a *BEM* without dynamically deforming the wake sheet aft of the propeller.

A parallel branch of developments in *BEM* is related to free surface applications, which can be divided into those concerning ship wave resistance and those solving ocean wave propagation. Several simplified theories computing a ships wave resistance have been established because the problem is to complex to be solved analytically. Similar to methods computing the flow field around propellers, the development of more sophisticated wave-resistance methods was driven by the availability of more computational power in the 1970s. One of those early linearised methods was proposed by Dawson [24]. Many researchers contributed to the development and in the late 1980s non-linear methods were also established, starting with the work of Ni [74] and Jensen [49]. Raven [78] pointed out that no further improvements could be found within the linear approaches and large errors occurred for higher wave elevations in cases of slender ships at higher speeds. Raven gives a comprehensive historical review on ship wave resistance methods and also proposes a method himself. The computational models for wave-flows are often highly non-linear in order to be able to compute steep waves, breaking waves and complex seaway shapes. Examples for those methods and literature reviews are presented by Tsai and Yue [93] and Grilli [37].

Propellers subjected to ventilation or - in this case - that emerge out of the water were already treated by Isay [46] in 1966 using the lifting line theory. Later, several similar models based on potential theory were developed; but with *RANSE* solvers becoming widely available in the late 1990s, no substantial improvement was reported. A special application in this context is the simulation of surface piercing propellers (which will not be focussed on in this thesis), because the free surface is extremely distorted and the forces acting on the propeller have to be treated specially. This is addressed by two-dimensional approaches which have been applied for propellers e.g. by Young [100].

For the simulation of dynamic processes several different solver-coupling procedures using various methods can be found in the literature. The underlying method is often a *RANSE* simulation, while the second method works in principle as a propeller model. With this approach, complex phenomena like pronounced unsteady behaviour, pod housing- or free surface-influences can also be addressed. First attempts to model

propeller effects by means of a force field in an inviscid flow were described as early as 1972 by Sparenberg [86], [87], who aimed to find the optimum actuator disc for a prescribed thrust. Schetz and Favin [82], [83] reported attempts to model propeller forces in an axisymmetric flow field employing a one-way coupling to the Navier-Stokes equations in a stream-function formulation. A more general two-way coupling was first reported by Stern et al. [89] in 1988. Computations were performed in steady state based on the circumferential averages of the propeller forces. They were determined by a vortex-lattice lifting-surface method and adjusted to the flow field upstream the propeller in an iterative procedure.

Several two-way coupling approaches with different levels of complexity have recently been developed. Typically, the ship and the appendages are resolved (i.e. geometrically modelled) by the *RANSE* mesh and the propeller effect is computed externally in order to limit the computational and mesh-generation effort. In most cases steady potential flow methods or even more simple assumptions, e.g. prescribed force parameterisations as described by Carrica et al. [22], are used to determine the propeller influence. An example is presented by Phillips et al. [75]. The authors describe a coupling procedure using the blade element momentum theory (BEMT) to model the propeller forces. These forces are applied in a *RANSE* domain with a ship hull and a rudder included. An averaged *RANSE*-calculated nominal wake fraction evaluated at prescribed radial positions serves as input to the BEMT. The calculated thrust and torque values obtained from the BEMT are transformed into radius averaged momentum source terms acting in a cylindrical region at the propeller position inside the *RANSE* domain. With these body-forces, the steady *RANSE* simulation is iterated to convergence. The authors employ this method to compute the rudder forces with fair accuracy.

Another possibility to model the propeller forces in a *RANSE* computation is described by Müller et al. [71]. The authors compare the performance of a coefficient-based force model with a geometrically resolved propeller. The propeller influence is not computed from an inviscid numerical analysis but is modelled based on force coefficients evaluated in different sections of the blade. They studied the influence of the propeller representation on the velocity distribution in the aft ship region as well as the associated computational and grid-generation efforts. Good accuracy was observed for the velocity distribution in conjunction with a significantly smaller computational effort for the simulations employing the propeller model due to the smaller amount of grid cells and the absence of sliding grid interfaces. In Müller‘s approach a simplified velocity distribution located at a short distance upstream the propeller serves as input for the coefficient-based model which determines the thrust and torque contributions for prescribed radial blade sections. The propeller model thus considers the variation of thrust and torque in radial and circumferential direction but not the actual blade positions.

2.3. Examples for Experimental Campaigns

The experimental determination of the forces and moments acting on ship propellers in open water conditions is a standard test for a propeller design prior to its casting. Also, the cavitation behaviour is investigated in the cavitation test and the interaction between ship and propeller is investigated in the self-propulsion test, where the ability to propel a ship to the designated speed using a given torque is tested. Nonetheless, no unsteady loads acting on the propeller or other components of the propulsion unit are usually determined. However, in the case of thruster drives investigated in this work, these loads can affect the design of the mechanical components of such a system, like gears and bearings. When the propeller operates behind a ship, the static and dynamic behaviour in oblique inflow is of particular interest. An aft ship geometry with ascending buttocks, a possible drift angle of the ship and - in some cases - a shaft inclination means that the flow is in general inclined in the propeller position. The dynamic behaviour is of interest because of the ship motions and of wave orbital velocities. They affect the propeller operation and have been subject to studies for a long time. Several experimental investigations were carried out in the 1920s and 1930s for ship and airplane propellers operating in oblique inflow. One exemplary study is published by Graff [31]. To eliminate the effect of the hull, the forces acting on a heaving and pitching propeller in open water condition were measured in a towing tank. Graff points out that oblique inflow as a result of the ship geometry leads to an eccentric centre of thrust and can affect the stability of course keeping. Graff also reported on thrust fluctuations on a single propeller blade and their effect on the structural design of the propeller.

Later, a large experimental study was carried out in Potsdam and published e.g. by Gutsche [38]. The motivation herein was to quantify the influence of geometrical properties of a propeller on the above-mentioned effects occurring at a propeller in oblique inflow conditions. The focus was set on propeller side forces, the force fluctuations on a single blade and the estimation of cavitation inception. The force fluctuations were of interest because of the increased usage of controllable pitch propellers at that time. For this kind of propeller the pitching moment acting on the pitch adjusting system can also change significantly due to a displacement of the load incidence point. An experimental study designed to find out the unsteady blade forces and moments including the pitching moment, is given by Bednarzik [11]. From experimental campaigns theoretical approaches were also developed for the propeller loads of a ship in waves, as published e.g. by Gutsche [38] and later by Stoeckert and Gatzer [90]. Many more investigations for propellers can be found addressing the operation of small, fast ships having shaft inclination. These will not be treated here.

More recently, experimental investigations have focussed on the determination of loads acting on thrusters and pods because large units with up to $23MW$ of power[2] have been developed in the last years. Examples for model scale experiments were given by Szantyr et al. [91] in 2001 and Heinke [40] in 2004, where they presented the stationary and dynamic loads acting on azimuthing podded drives. Later, Ball and Carlton [9], [10] reported on experimentally determined loads acting on a pod in calm water and in waves during manoeuvres, such as turning, zigzag and crash-stop and on the loads occurring during unberthing manoeuvres for a twin-pod frigate. They post-process the thrust and torque increase, as well as shaft bending moments. Another large experimental campaign is reported by Islam et al. [47] for a static and dynamic azimuthing podded propulsor. More recently, several investigations have been performed in Norway at the ship model tank and the ocean laboratory of *MARINTEK* on ships equipped with thruster drives. Of these, Amini [3] shows experimental results for the forces acting on a podded propeller in waves. Koushan et al. [59], [60] give a similar contribution for a thruster propeller in waves in terms of the dynamic propeller forces and the blade loadings and spindle torque. A comparison of the experimentally and numerically determined loads by means of *RANSE* simulations is given by Califano [16]. The author also provides detailed investigations of ventilation inception and the formation of vortex systems between propeller and free water surface. A comparison between the loads acting on a free-running compared to those acting on a ship-mounted thruster is given by Amini and Steen [5].

For the same ship, full-scale measurements were conducted and reported by Savio and Steen [81], who focussed on interpreting the vast amount of data collected during an 18-month phase of ship operations and on the identification of ventilation events. After the full-scale monitoring, ventilation events were reproduced with a free-running ship in the model test basin and compared to the full-scale results by Savio et al. [80]. Another approach to produce an improved prognosis of the ventilation phenomena compared to the full-scale case is given by Brouwer and Hagesteijn [13], who conducted experiments with a ventilating pod-propeller operating in a cruise liner in waves in a depressurized towing tank.

[2] This value refers to the max. output for an ABB XO2300-pod given in the product brochure. See ABB homepage (www.abb.com) for more details.

3. Computational Model

This chapter reports on the determination of equations describing the flow problem addressed in Section 3.1 and the simulation model used in this thesis in 3.2. Also, the implementation of a numerical procedure coupling two flow solvers is reported in Section 3.3. First, the equations used are derived from the conservation equations which fully describe the physics in a real flow problem. A body-fixed coordinate system is used and the equations are set up in a moving frame of reference. An exemplary flow problem is used to determine boundary conditions and - in the following - to derive a *BEM* formulation of the fluid flow and to set up the integral formulation of the velocity potential in Section 3.2.1. With this potential definition, all types of flow situations addressed in this work can be set up. The boundary conditions used at the free water surface are discussed separately in Section 3.2.2.

In Section 3.2.3, the solution method used to set up the *BEM* is described in line with the chosen singularities. Also, the implementation of additional features such as wave potential and viscous effects are discussed. This is followed by a description of the numerical implementation in Section 3.2.4, where some parts of the code are described and the process of determining a solution is presented. This features an in-depth explanation of the free surface treatment in the program.

The solver coupling method, which links the *BEM* to a *RANSE* solver is described in Section 3.3. This refers more to an implementation of a numerical technique than to a physical problem solution. The flow problem is divided in order to reduce the set-up effort and computational costs, while both parts of the problem can be addressed by a convenient solver. This means that the propeller, where the dominant forces are non-viscous and a thruster housing or a ship geometry, where the flow-situation is greatly influenced by non-viscous effects, are separated. The physical considerations upon which the method is based are first described in Section 3.3.1, followed by details on the numerical implementation in Section 3.3.2.

3.1. Governing Equations for Potential Flow

To derive the equations describing a flow field, the different properties of the fluid are studied as integral values inside a control volume (*c.v.*) in the fluid (see Katz and Plotkin [51], sec. 1.5). This control volume is considered as stationary and deeply submerged. Since there is no source of material, the mass $m_{c.v.}$ inside the control volume must be conserved. So the change of mass with time, which is only dependent on density and flow passing through the surface *c.s.* of the control volume, is zero:

$$\frac{dm_{c.v.}}{dt} = \frac{\partial}{\partial t}\int_{c.v.} \rho dV + \int_{c.s.} \rho(\mathbf{v}\cdot\mathbf{n})dS = 0. \tag{3.1}$$

With V being the volume and S the surface of the control volume. The term $\rho(\mathbf{v}\cdot\mathbf{n})$ describes the rate of mass passing through the boundaries S of the control volume, with the velocity vector $\mathbf{v}$ and the surface normal $\mathbf{n}$ pointing in the outward direction of each surface element dS.

Similar to the conservation of mass in Equation (3.1), the momentum inside the control volume can be balanced. The total momentum consists of the momentum in the fluid flow inside the *c.v.* and the change of momentum through the surface S:

$$\frac{d(m\mathbf{v})_{c.v.}}{dt} = \frac{\partial}{\partial t}\int_{c.v.} \rho\mathbf{v} dV + \int_{c.s.} \rho\mathbf{v}(\mathbf{v}\cdot\mathbf{n})dS = \sum \mathbf{f}. \tag{3.2}$$

Due to Newton's second law, the forces $\mathbf{f}$ acting on a system during the time interval dt are equal to the change of the total momentum of the system. The forces can be either body forces f_i or surface forces $n_j\tau_{ij}$[1]. The former act per unit mass and are independent of any contact with the fluid. They are proportional to the volume or mass of the body and can result from force fields, for example gravitation and magnetic or electrodynamic forces. The latter are exerted at the intersecting surface between an obstacle or physical boundary in the fluid domain and the surface of the control volume. When considering the sum of all parts in Equation (3.2) acting in the x_i direction, it reads

$$\frac{\partial}{\partial t}\int_{c.v.} \rho v_i dV + \int_{c.s.} \rho v_i(\mathbf{v}\cdot\mathbf{n})dS = \int_{c.v.} \rho f_i dV + \int_{c.s.} n_j\tau_{ij} dS. \tag{3.3}$$

Surface forces can be divided into pressure forces acting normal to the surface and tangential forces. Pressure forces result from normal stresses and tangential forces from shear stresses on the control surface.

[1] The simplifications $\begin{pmatrix} \tau_{11} & \tau_{12} & \tau_{13} \\ \tau_{21} & \tau_{22} & \tau_{23} \\ \tau_{31} & \tau_{32} & \tau_{33} \end{pmatrix} = \tau_{ij}$ and $\sum_{j=1}^{3} \tau_{ij}n_j \equiv \tau_{ij}n_j$ are used here according to the Einstein notation.

The third conservation law in the context of computational fluid dynamics is the energy conservation law. Because the energy equation reduces to the momentum equation for an isothermal fluid, it is neglected in this work.

The Equations (3.1) and (3.3) give a complete description of a fluid motion in the integral formulation. For the purpose of a numerical solution, in order to discretise the geometry, the differential form is more convenient. Following Katz and Plotkin [51] and transforming the surface integrals to volume integrals using the Gauss' theorem (see e.g. Bronstein et al. [12], sec. 13.3.3)

$$\int_{c.s.} \mathbf{n} \cdot \mathbf{v} dS = \int_{c.v.} \nabla \cdot \mathbf{v} dV, \tag{3.4}$$

the mass conservation Equation (3.1) can be transformed to

$$\int_{c.v.} \left(\frac{\partial \rho}{\partial t} + \nabla \cdot \rho \mathbf{v} \right) dV = 0. \tag{3.5}$$

Equation (3.5) is fulfilled when the integrand is set to zero. When considering incompressible flow, which is sufficient for most marine applications, the density is constant and the continuity equation reduces to

$$\nabla \cdot \mathbf{v} = \frac{\partial u}{\partial x} + \frac{\partial v}{\partial y} + \frac{\partial w}{\partial z} = 0. \tag{3.6}$$

When a system contains only non-rotating flow, a velocity potential Φ can be introduced, where $\nabla \Phi = \mathbf{v}$ and the continuity Equation (3.6) becomes

$$\nabla \cdot \mathbf{v} = \nabla \cdot \nabla \Phi = \nabla^2 \Phi = 0. \tag{3.7}$$

This is Laplace's equation, the essential equation describing the velocity field in a potential flow domain.

The momentum Equation (3.3) can be transformed in a similar manner using the Gauss' theorem to get a volume integral formulation

$$\int_{c.v.} \left[\frac{\partial}{\partial t}(\rho v_i) + \nabla \cdot \rho v_i \mathbf{v} - \rho f_i - \frac{\partial \tau_{ij}}{\partial x_j} \right] dV = 0, \qquad \text{for } i, j \in [1, 2, 3]. \tag{3.8}$$

Again the integrand can be set to zero:

$$\frac{\partial}{\partial t}(\rho v_i) + \nabla \cdot \rho v_i \mathbf{v} = \rho f_i + \frac{\partial \tau_{ij}}{\partial x_j}, \qquad \text{for } i, j \in [1, 2, 3]. \tag{3.9}$$

When again assuming an irrotational and incompressible flow field and using the continuity Equation (3.6), the left hand side can be transformed to

$$\frac{\partial}{\partial t}(\rho v_i) + \nabla \cdot \rho v_i \mathbf{v} = \rho \frac{\partial v_i}{\partial t} + v_i \frac{\partial \rho}{\partial t} + \rho v_i \nabla \cdot \mathbf{v} + \rho \mathbf{v} \cdot \nabla v_i = \rho \left(\frac{\partial v_i}{\partial t} + \mathbf{v} \cdot \nabla v_i \right). \tag{3.10}$$

For a Newtonian Fluid the stress tensor τ_{ij} can be related to the velocity field (see, e.g. Ferziger and Peric [28], sec. 1.4) by

$$\tau_{ij} = -\left(p + \frac{2}{3}\mu\frac{\partial v_j}{\partial x_j}\right)\delta_{ij} + \mu\left(\frac{\partial v_i}{\partial x_j} + \frac{\partial v_j}{\partial x_i}\right). \tag{3.11}$$

When inserting Equations (3.11) and (3.10) in Equation (3.9), the Navier-Stokes equations are established

$$\begin{aligned}&\rho\left(\frac{\partial v_i}{\partial t} + \mathbf{v}\cdot\nabla v_i\right) = \\ &\rho f_i - \frac{\partial}{\partial x_i}\left(p + \frac{2}{3}\mu\frac{\partial v_j}{\partial x_j}\right)\delta_{ij} + \frac{\partial}{\partial x_j}\mu\left(\frac{\partial v_i}{\partial x_j} + \frac{\partial v_j}{\partial x_i}\right), \quad \text{for } i,j \in [1,2,3].\end{aligned} \tag{3.12}$$

For an incompressible fluid, the Navier-Stokes equations can be simplified by applying the continuity Equation (3.6) and for a non-viscous fluid by neglecting the dynamic viscosity ($\mu_f = 0$). When using vector notation the Euler equation results as

$$\frac{\partial \mathbf{v}}{\partial t} + \mathbf{v}\cdot\nabla\mathbf{v} = \mathbf{f} - \frac{\nabla p}{\rho}. \tag{3.13}$$

The first term accounting for the time derivative of the velocity can be rewritten using the velocity potential Φ

$$\frac{\partial \mathbf{v}}{\partial t} = \frac{\partial}{\partial t}\nabla\Phi = \nabla\left(\frac{\partial\Phi}{\partial t}\right). \tag{3.14}$$

The second term can be transformed using the formulation for the gradient of the vector dot product

$$\begin{aligned}\nabla(\mathbf{v}\cdot\mathbf{v}) &= 2(\mathbf{v}\cdot\nabla)\mathbf{v} + 2\mathbf{v}\times(\nabla\times\mathbf{v}),\\ \text{and it reads}\quad (\mathbf{v}\cdot\nabla)\mathbf{v} &= \nabla\frac{v^2}{2} - \mathbf{v}\times(\nabla\times\mathbf{v}).\end{aligned} \tag{3.15}$$

The term $\nabla\times\mathbf{v}$ can be described as the vorticity of an infinitesimal flow element and is zero in the case of irrotational flow. The vector field of external forces $\mathbf{f}$ is assumed to be conservative and can be hence expressed in terms of a potential E as

$$\mathbf{f} = -\nabla\mathbf{E} \tag{3.16}$$

When substituting Equations (3.14), (3.15) and (3.16) into the Euler equation, it reads

$$\nabla\left(E + \frac{p}{\rho} + \frac{v^2}{2} + \frac{\partial\Phi}{\partial t}\right) = 0. \tag{3.17}$$

This is valid, when the term in parentheses is only time-dependent. Then, the following equation, called the Bernoulli equation, results for inviscid, irrotational and incompressible flow

$$E + \frac{p}{\rho} + \frac{v^2}{2} + \frac{\partial\Phi}{\partial t} = C(t). \tag{3.18}$$

3.2. Description of the Potential Flow Method

3.2.1. Statement of the Problem

In this thesis, a *BEM* is used to solve the Laplace Equation (3.7) derived above. The flow problem is reduced only to the physical boundaries of the flow domain using the Gauss theorem (3.4). A general flow problem addressed by the method is depicted in Figure 3.1, showing an airfoil and its trailing wake sheet in a flow domain bounded by the bottom, the free water surface and a wall at infinite distance.

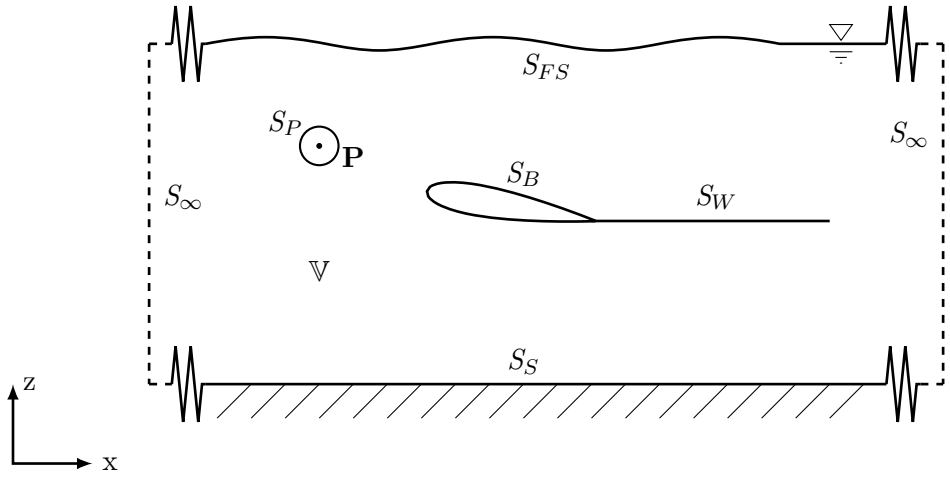

Figure 3.1.: Simulation domain

The airfoil displayed in the sketch is bounded by the surface S_B, which must not be penetrated by the fluid. Therefore it is required that the gradient of the total velocity potential (which is the total velocity) in the direction of the surface is zero

$$\nabla\Phi \cdot \mathbf{n} = 0. \tag{3.19}$$

With $\mathbf{n}$ being the direction normal to the surface. The total velocity potential Φ consists of the induced potential Φ_{ind} due to the presence of the body, the motion potential of the fluid Φ_M and an external potential Φ_{ext}. The coordinate system is defined as shown in Figure 3.2 with its origin at the position of the undisturbed free water surface and it is moving together with the body of interest having a horizontal velocity $\mathbf{v}_M(t)$. A requirement for the induced potential is that Φ_{ind} - the disturbance in the flow field due to the body - should vanish in far distance from the body. This makes it possible to neglect the outer boundary S_∞ and it reads

$$\lim_{r->\infty} \nabla\Phi_{ind} = 0. \tag{3.20}$$

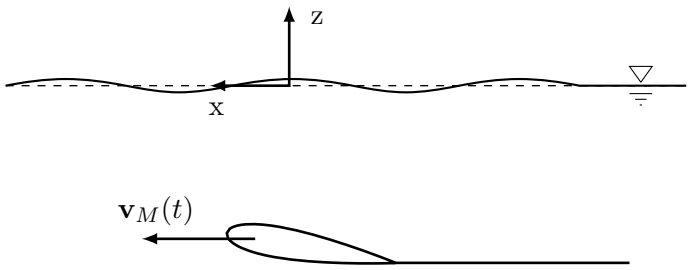

Figure 3.2.: Definition of the coordinate system

In order to maintain a formulation for Laplace's equation, the field function Φ is defined as a product of the two functions of position Φ_1 and Φ_2. Then the velocity $\mathbf{v}$ reads

$$\mathbf{v} = \nabla(\Phi_1\Phi_2) = \Phi_1\nabla\Phi_2 - \Phi_2\nabla\Phi_1. \tag{3.21}$$

Using this formulation for the velocity, Green's identity (see e.g. Bronstein et al. [12], sec. 13.3.3) can be used to get a surface integral form of the flow problem

$$\int_V \nabla^2\Phi dV = \int_V (\Phi_1\nabla^2\Phi_2 - \Phi_2\nabla^2\Phi_1)dV = \int_S (\Phi_1\nabla\Phi_2 - \Phi_2\nabla\Phi_1)\cdot\mathbf{n}dS. \tag{3.22}$$

From this conversation the ansatz of the *BEM* results because an integral formulation of the equations on the boundaries is sufficient to describe the complete flow field. The two Φ-functions are set to $\Phi_1 = 1/r$ and $\Phi_2 = \Phi$ according to Katz and Plotkin [51] (sec. 3.2). The former automatically fulfils the b.c. at infinity (3.20), with r being the distance from a point $P(x, y, z)$ and the latter is the potential in the flow field $\mathbb{V}$.

If we consider a flow regime as depicted in Figure 3.1 in an earth-fixed coordinate system, the bounding surfaces can be divided into different parts $S = S_B + S_W + S_{FS} + S_S + S_\infty$. Using the subscripts B for body, W for wake, FS for free water surface, S for symmetry (at the bottom) and ∞ for the infinite boundary. The flow domain is defined to be an enclosed volume, hence all bodies have to be closed. Using (3.22) together with the Laplace equation and the assumptions made above, the equation becomes:

$$\int_S \left(\frac{1}{r}\nabla\Phi - \Phi\nabla\frac{1}{r}\right)\mathbf{n}dS = 0. \tag{3.23}$$

When the potential is calculated for a point $P(x, y, z)$ located inside $\mathbb{V}$, the term $1/r$ is not defined for $\lim_{r\to 0}$, so the point itself must be excluded from the integration volume. This is done by a small volume V_P surrounding P. When considering this volume, the

integral in Equation (3.23) accounts for S and S_P, the bounding surface of the volume V_P

$$\int_S \left(\frac{1}{r}\nabla\Phi - \Phi\nabla\frac{1}{r}\right)\mathbf{n}dS + \int_{S_P} \left(\frac{1}{r}\nabla\Phi - \Phi\nabla\frac{1}{r}\right)\mathbf{n}dS_P = 0. \tag{3.24}$$

The small volume V_P can be situated either within $\mathbb{V}$ or on one of its boundaries. For the former case V_P is defined as a sphere, for the latter as a hemisphere. Analytical solutions for the value of the potential exist for both cases, when $r \to 0$:

$$\int_{S_P(sphere)} \left(\frac{1}{r}\nabla\Phi - \Phi\nabla\frac{1}{r}\right)\mathbf{n}dS_P = 4\pi\Phi(P) \tag{3.25}$$

$$\text{and} \quad \int_{S_P(hemisphere)} \left(\frac{1}{r}\nabla\Phi - \Phi\nabla\frac{1}{r}\right)\mathbf{n}dS_P = 2\pi\Phi(P). \tag{3.26}$$

For a point located inside $\mathbb{V}$ and not on the boundary, the potential at a point P becomes

$$\Phi(P) = \frac{1}{4\pi}\int_S \left(\frac{1}{r}\nabla\Phi - \Phi\nabla\frac{1}{r}\right)\mathbf{n}dS \tag{3.27}$$

$$\Leftrightarrow \boxed{\Phi(P) = \frac{1}{4\pi}\int_S \frac{1}{r}\frac{\partial\Phi}{\partial n} - \Phi\frac{\partial}{\partial n}\frac{1}{r}dS}. \tag{3.28}$$

Here, the local normal vectors of all boundaries are known and $\mathbf{n}\cdot\nabla$ can be replaced by $\frac{\partial}{\partial n}$. Equation (3.28) is the essential equation for the determination of the potential at any point *inside* $\mathbb{V}$. When P is on one of the boundaries, the factor $\frac{1}{4\pi}$ changes to $\frac{1}{2\pi}$ due to (3.26). For the flow domain depicted in Figure 3.1, a total potential can be constructed as the sum of all potentials present in the flow domain, being

$$\Phi(P) = \Phi_{ind}(P) - \Phi_M(P) + \Phi_{ext}(P). \tag{3.29}$$

Using the induced potential Φ_{ind} inheriting the potential due to the body of interest. The motion potential Φ_M is negative, which results from the moving frame of reference (see Figure 3.2). Because of the linearity of Equation (3.7), any additional potential Φ_{ext} can be superposed. These external potentials can be e.g. those induced by other bodies, a wave potential or a ship wake field. One possible total potential as defined in Equation (3.29) can be constructed when the problem is solved for an airfoil and its trailing wake sheet. The induced potential is $\Phi_{ind} = \Phi_A + \Phi_W$. In this case, the external potential consists of the free water surface and the bottom and will be solved iteratively with the airfoil solution. The induced potential of the airfoil Φ_A can be defined as the potential jump across the boundary, which is the difference between the

potential outside and inside the body. It reads

$$\begin{aligned}\Phi_A(P) &= \frac{1}{4\pi}\int_{S_A}\left(\frac{1}{r}\frac{\partial}{\partial n}(\Phi_A-\Phi_A^{(i)})-(\Phi_A-\Phi_A^{(i)})\frac{\partial}{\partial n}\frac{1}{r}\right)dS_A \\ &= \frac{1}{4\pi}\int_{S_A}\left(\frac{1}{r}\frac{\partial}{\partial n}\Phi-\Phi\frac{\partial}{\partial n}\frac{1}{r}\right)dS_A\end{aligned} \tag{3.30}$$

with the superscript i denoting the inner potential of the body.

The wake sheet S_W is a thin layer without a displacement effect. The total velocity $\frac{\partial\Phi}{\partial n}$ is continuous across it, but the potential is not. Because the wake sheet is aligned along the streamline leaving the trailing edge of an airfoil, the velocity across it is actually zero ($\nabla\Phi\cdot\mathbf{n}=0$) and the potential of the wake reads

$$\Phi_W(P) = -\frac{1}{4\pi}\int_{S_W}\Phi\frac{\partial}{\partial n}\frac{1}{r}dS_W. \tag{3.31}$$

For a free water surface the same assumptions as for a body can be made and the potential becomes

$$\Phi_{FS}(P) = \frac{1}{4\pi}\int_{S_{FS}}\left(\frac{1}{r}\frac{\partial}{\partial n}\Phi-\Phi\frac{\partial}{\partial n}\frac{1}{r}\right)dS_{FS}. \tag{3.32}$$

When a bottom is considered in a simulation, it can be modelled as a mirroring b.c. with the effect, that $\Phi^{(i)}=\Phi$ at the bottom, so that the second term in Equation (3.28) vanishes. The potential becomes

$$\Phi_S(P) = \frac{1}{4\pi}\int_{S_S}\frac{1}{r}\frac{\partial}{\partial n}\Phi dS_S. \tag{3.33}$$

The two remaining unknowns in this case are $\frac{\partial\Phi}{\partial n}$ and Φ on the surface of the airfoil and its wake sheet

$$\begin{aligned}\Phi(P) =& \frac{1}{4\pi}\int_{S_B}\left(\frac{1}{r}\frac{\partial}{\partial n}\Phi-\Phi\frac{\partial}{\partial n}\frac{1}{r}\right)dS_B-\frac{1}{4\pi}\int_{S_W}\Phi\frac{\partial}{\partial n}\frac{1}{r}dS_W \\ &+\Phi_{FS}-\Phi_M.\end{aligned} \tag{3.34}$$

Due to the general formulation of the problem in Equation (3.29), the method is very flexible. For every problem addressed by the method, the total potential $\Phi(P)$ can be constructed from different parts and numerous bodies can be solved for having different motions within a single problem setup, as long as Φ_{ind} is solved for bodies having the same motion. The external potential Φ_{ext} and its parts are known potential solutions and - in case of the potential at the free water surface Φ_{FS} - can be solved iteratively with the airfoil.

3.2.2. Free Water Surface Boundary Conditions

At a free water surface two boundary conditions have to be fulfilled. The first requires atmospheric pressure directly at the surface and is called the dynamic b.c. The second is the kinematic b.c., which relates the motion of the free surface to the normal component of the water velocity at the surface.

The dynamic b.c. is derived from the unsteady Bernoulli equation

$$-\rho\frac{\partial\Phi}{\partial t}-\frac{1}{2}\rho\left(\nabla\Phi\right)^2+p+\rho gz=C(t), \tag{3.35}$$

which is valid at the actual free surface elevation $\zeta = z$. In a steady flow situation, the free water surface and a body beneath it do not move and a constant advance velocity $-\mathbf{v}_M$ in horizontal direction can be applied acting towards the body in the body-fixed coordinate system. Moreover, a constant pressure $p = p_{athm.}$ is stated at the free surface, and Equation (3.35), stated for two points at the surface, becomes

$$-\frac{1}{2}\left(\nabla\Phi-\mathbf{v}_M\right)^2+g\zeta=-\frac{1}{2}\mathbf{v}_M^2, \tag{3.36}$$

$$\Leftrightarrow -\frac{1}{2}\left(\nabla\Phi\right)^2+\mathbf{v}_M\nabla\Phi+g\zeta=0. \tag{3.37}$$

The free surface elevation can be obtained using the dynamic b.c. by rearranging Equation (3.37)

$$\zeta=\frac{1}{g}\left[\frac{1}{2}\left(\nabla\Phi\right)^2-\mathbf{v}_M\nabla\Phi\right]. \tag{3.38}$$

The kinematic b.c. requires the normal components of the water velocity to be equal to the motion of the free water surface, say

$$\frac{Dz}{Dt}=\frac{D\zeta}{Dt}\quad\text{at}\quad z=\zeta. \tag{3.39}$$

Using a formulation for the material derivative $\frac{D}{Dt}=\frac{\partial}{\partial t}-\nabla\Phi\cdot\nabla$, the equation reads

$$-\frac{\partial\Phi}{\partial z}=\frac{\partial\zeta}{\partial t}-\nabla\Phi\nabla\zeta. \tag{3.40}$$

In this formulation, the sign of terms including the potential Φ is negative, because of the potential being positive downwards, pointing into the computation domain and against the z-direction. In the steady case, a combined free surface b.c is constructed from the dynamic (3.37) and the kinematic b.c. (3.40). Therefore, the derivative of the free surface elevation (3.38) is established and inserted in the kinematic b.c.

$$\frac{\partial\Phi}{\partial z}=\frac{1}{2g}\nabla\Phi\nabla\left(\nabla\Phi\right)^2-\frac{\mathbf{v}_M}{g}\nabla\Phi\nabla^2\Phi. \tag{3.41}$$

The combined b.c can be linearised by neglecting higher order terms and assuming an additional simplification $\frac{\partial \phi}{\partial z} = \frac{\partial \phi}{\partial n}$, which is only valid for linear waves

$$\frac{\partial \Phi}{\partial n} = -\frac{\mathbf{v}_M}{g} \nabla \Phi \nabla^2 \Phi. \tag{3.42}$$

Furthermore, a simplification can be made to the kinematic b.c. using the assumption that the disturbance velocity due to the body is small compared to the uniform inflow and the approximation $\nabla \Phi = \mathbf{v}_M$ is made

$$\frac{\partial \Phi}{\partial n} = -\frac{\mathbf{v}_M^2}{g} \nabla^2 \Phi. \tag{3.43}$$

This is the non-iterative combined b.c., which can only be derived for a steady flow situation. Equation (3.43) is a rather simple form of the combined free surface b.c. and several different linearisations of the condition (3.41) have been published. Examples for steady linearised formulations are e.g. given by Jensen [49], Raven [77] and Janson [48].

In an unsteady case, the free water surface is moving with a prescribed velocity $\mathbf{v}_M(t)$ in the horizontal plane, so the potential can be rewritten using the induced potential Φ_{ind} due to the body actually solved for, the motion potential Φ_M and the external potential Φ_{ext}, resulting in $\Phi = \Phi_{ind} - \Phi_M + \Phi_{ext}$. Now, the pressure computed by the dynamic b.c (3.35) is set in relation to a point moving with the reference frame at the undisturbed free surface height, but located far away, where the disturbance has decayed and it reads

$$-\rho \frac{\partial \Phi_{ind} + \Phi_{ext}}{\partial t} - \frac{1}{2}\rho \left(\nabla \Phi_{ind} - \mathbf{v}_M + \nabla \Phi_{ext}\right)^2 + p + \rho g z = p_{athm.} - \frac{\rho}{2} \left(\mathbf{v}_M\right)^2. \tag{3.44}$$

Again, the atmospheric pressure $p_{athm.}$ is set equal to zero and the free surface elevation is ζ. The dynamic b.c. becomes

$$-\frac{\partial \Phi_{ind} + \Phi_{ext}}{\partial t} - \frac{1}{2} \left(\nabla \Phi_{ind} - \mathbf{v}_M + \nabla \Phi_{ext}\right)^2 + g z = -\frac{1}{2} \left(\mathbf{v}_M\right)^2 \quad \text{at} \quad z = \zeta. \tag{3.45}$$

$$\Leftrightarrow \frac{\partial \Phi_{ind}}{\partial t} = -\frac{1}{2} \left(\nabla \Phi_{ind} - \mathbf{v}_M + \nabla \Phi_{ext}\right)^2 + g\zeta + \frac{1}{2} \left(\mathbf{v}_M\right)^2 + \frac{\partial \Phi_{ext}}{\partial t}. \tag{3.46}$$

The unsteady kinematic b.c. following Equation (3.40) can be written as

$$\frac{\partial \zeta}{\partial t} = -\frac{\partial \Phi_{ind} + \Phi_{ext}}{\partial z} + \left(\nabla \Phi_{ind} - \mathbf{v}_M + \nabla \Phi_{ext}\right) \cdot \nabla \zeta. \tag{3.47}$$

3.2.3. Solution Method

Within this section, a solution method for the potential equations derived above is given. The potential of the flow domain, which is derived in (3.28) and later in (3.34), must be solved by a numerical procedure for every point $P(x, y, z) \in \mathbb{V}$ where a boundary condition is enforced. This can be done by imposing a Dirichlet type b.c and solving directly for the potential. Equation (3.28) results in this case. A second possibility is to use a Neumann type b.c. on the bodies surface and (3.28) becomes

$$\nabla\Phi(P) \cdot \mathbf{n} = \frac{1}{4\pi} \int_S \nabla \left(\frac{1}{r} \frac{\partial \Phi}{\partial n} - \Phi \frac{\partial}{\partial n} \frac{1}{r} \right) \cdot \mathbf{n} dS = 0. \tag{3.48}$$

Because of the gradient used in the Neumann case, some authors refer to a velocity-based formulation, whereas the Dirichlet case is a potential-based formulation of the problem. A discussion on the validity of the formulations is given in Kerwin et al. [52].

In the following, some possibilities for solving typical *BEM* problems will be discussed.

superposition of singularity elements

Because of the linearity of the Laplace Equation (3.7), K potentials Φ_i, each of it fulfilling $\nabla^2\Phi_i = 0$, can be superposed. The result is a new potential Φ with

$$\Phi = \sum_{i=1}^{K} c_i \Phi_i \tag{3.49}$$

for which a linear combination of potentials Φ_i and constants c_i have to be found. These potentials are determined using singularity elements for the unknown values Φ_i and $\frac{\partial \Phi_i}{\partial n_i}$ on the boundaries of the flow domain. In order to solve the potential flow field using the present method, a distribution of sources and doublets with constant strengths over the adjacent surface elements is used. The singularity elements of a source in combination with a doublet are sufficient for the representation of a body having a displacement effect and producing lift. One source element consists of a point source with its strength $\sigma(P_0)$ and its potential $\Phi_S(P) = -\frac{\sigma}{4\pi r}$ integrated over the surface S of the element using the radial distance r between P and P_0. A source generates a velocity field having only a radial component diverging from the origin. The velocity value decays with the rate of $\frac{1}{r^2}$ and is singular at the radius $r = 0$. The potential of a

surface element is the integral value of the potential for local surface elements having the distance to the source r and the surface dS

$$\Phi_S(P) = -\frac{\sigma}{4\pi}\int_S \frac{1}{r} dS. \tag{3.50}$$

Now, consider a sink defined as a source with negative strength. When combining a source and a sink located very close to each other, the singularity element of a doublet is constructed. One point doublet produces a symmetric flowfield relative to its main axis and an axial flow component like a propulsor. Therefore, a doublet is a directional element and the potential of a doublet is defined so that its strength $\mu(P_0)$ accounts in the direction of the normal vector of the surface element. In a flow situation where a body is subject to an incident flow, a doublet element produces a lift component when the axis is not directed parallel to the inflow direction. The potential of one point doublet is $\Phi_D(P) = -\frac{\boldsymbol{\mu}\cdot\mathbf{r}}{4\pi r^3}$. Again, the basic point doublet is integrated over the surface of one element and it reads

$$\Phi_D(P) = -\frac{\mu}{4\pi}\int_S \mathbf{n}\cdot\frac{(x-x_0)}{r^3} dS. \tag{3.51}$$

Using the singularity elements defined above, the potential defined in (3.34) can be expressed in terms of a distribution of sources with source strength σ and doublets with doublet strength μ and the unknowns become

$$\frac{\partial\Phi}{\partial n} = \sigma \quad \text{and} \quad \Phi = \mu. \tag{3.52}$$

The total potential reads

$$\begin{aligned}\Phi(P) =& \frac{1}{4\pi}\int_{S_B}\left(\frac{1}{r}\sigma - \mu\frac{\partial}{\partial n}\frac{1}{r}\right) dS_B - \frac{1}{4\pi}\int_{S_W}\mu\frac{\partial}{\partial n}\frac{1}{r} dS_W \\ &+\frac{1}{4\pi}\int_{S_{FS}}\left(\frac{1}{r}\sigma - \mu\frac{\partial}{\partial n}\frac{1}{r}\right) dS_{FS} - \Phi_M + \Phi_W.\end{aligned} \tag{3.53}$$

Equation (3.53) defines the potential as a combination of sources and doublets. The strengths of these singularities is not unique and the same potential can be constructed with different distribution of σ and μ on the bounding surfaces.

blunt body in unbounded flow

The first problem discussed here is a body producing only a displacement effect (without circulation) and hence can be modelled by a distribution of sources on the body‘s surface. The body is moving at a constant velocity $\mathbf{v}_M$ in an unbounded fluid region

$\mathbb{V}$. Using the general formulation for the potential (3.28) and the formulation of source strength from Equation (3.52), the potential becomes

$$\Phi(P) = \frac{1}{4\pi} \int_{S_B} \frac{1}{r} \sigma dS_B - \Phi_M. \tag{3.54}$$

A Neumann type b.c. is enforced on the body and the potential in $\mathbb{V}$ reads

$$\nabla\Phi \cdot \mathbf{n} = \frac{1}{4\pi} \int_{S_B} \frac{1}{r} \nabla\sigma \cdot \mathbf{n} dS_B - \mathbf{v}_M \cdot \mathbf{n} = 0. \tag{3.55}$$

In the case that more than one body is present in $\mathbb{V}$, its influence can be taken into account by adding an induced potential Φ_{ind} in Equation (3.54). This leads to modifying the last term in Equation (3.55) to be $(\mathbf{v}_{ind} - \mathbf{v}_M) \cdot \mathbf{n}$.

airfoil in unbounded flow

In the case of an airfoil, the body has to be modelled with lift and the doublet type singularities presented above have to be taken into account. The total potential at point $P(x, y, z) \in \mathbb{V}$ becomes

$$\Phi(P) = \frac{1}{4\pi} \int_{S_B} \left(\frac{1}{r}\sigma - \mu \frac{\partial}{\partial n} \frac{1}{r} \right) dS_B - \frac{1}{4\pi} \int_{S_W} \mu \frac{\partial}{\partial n} \frac{1}{r} dS_W - \Phi_M. \tag{3.56}$$

This potential can be solved using a Neumann or a Dirichlet type b.c. as stated above. In both cases the number of unknowns for every collocation point on the body‘s surface is two, whilst only one equation is available. Therefore, one unknown has to be determined a priori to the formulation of an equation system. In order to do this, the Neumann b.c. on the surface of the body is used and the source strength σ can be determined

$$\begin{aligned} \nabla\Phi \cdot \mathbf{n} = \frac{\partial\Phi}{\partial n} &= \frac{\partial\Phi_{ind}}{\partial n} - \frac{\partial\Phi_M}{\partial n} + \frac{\partial\Phi_{ext}}{\partial n} = 0 \\ \Leftrightarrow \frac{\partial\Phi_{ind}}{\partial n} &= \sigma = \frac{\partial\Phi_M}{\partial n} - \frac{\partial\Phi_{ext}}{\partial n} \\ \Leftrightarrow \sigma &= (\mathbf{v}_M - \mathbf{v}_{ext}) \cdot \mathbf{n}, \end{aligned} \tag{3.57}$$

following Equation (3.29). Using this quite easy formula, the source strength only depends on the body‘s motion velocity, additional external velocities and the local normal direction on the surface of the body. The doublet strength remains unknown. One possible solution is to use the Neumann type b.c again to set up the potential problem and the equation becomes

$$\nabla\Phi \cdot \mathbf{n} = 0 = \frac{1}{4\pi} \int_{S_B} \frac{1}{r} \nabla\sigma \cdot \mathbf{n} dS_B - \frac{1}{4\pi} \int_{S_B + S_W} \mu \nabla \frac{\partial}{\partial n} \frac{1}{r} \cdot \mathbf{n} dS_{B+W} - \mathbf{v}_M \cdot \mathbf{n}. \tag{3.58}$$

In the case of a surface discretised with a source and doublet distribution, the usage of a Neumann b.c is mathematically not precise because it would be used twice together with Equation (3.57). Moreover, if the problem is solved using the velocity-based formulation, the value of the potential is not uniquely determined because of the unknown integration constant. Also, a larger grid dependency and a strong influence of thin trailing edges can be found because the induced velocity inherited in this model is much more sensitive to local effects than the induced potential used in the Dirichlet formulation. A detailed discussion on the effects is given by Hundemer [45].

For the reasons given above, it is preferred to impose a Dirichlet type b.c. on the body and to use the potential from Equation (3.56). In this case, the induced potential for a point $P(x, y, z) \in \mathbb{V}$ becomes

$$\Phi_{ind}(P) = \frac{1}{4\pi} \int_{S_B} \left(\frac{1}{r}\sigma - \mu \frac{\partial}{\partial n} \frac{1}{r} \right) dS_B - \frac{1}{4\pi} \int_{S_W} \mu \frac{\partial}{\partial n} \frac{1}{r} dS_W. \tag{3.59}$$

If P is shifted slightly inside the body, the problem can be solved for the potential inside the body, which is also valid for computing the singularities on the body‘s surface. The value of the inner potential can be chosen freely and is set to zero

$$\Phi_{ind}^{(inside)}(P) = 0 = \frac{1}{4\pi} \int_{S_B} \left(\frac{1}{r}\sigma - \mu \frac{\partial}{\partial n} \frac{1}{r} \right) dS_B - \frac{1}{4\pi} \int_{S_W} \mu \frac{\partial}{\partial n} \frac{1}{r} dS_W. \tag{3.60}$$

the Kutta condition

A basic principle of the potential theory is that a closed body does not experience any lift or drag forces when it is subjected to a constant inflow. This was stated by the mathematician and physician d'Alembert [65] in the 18th century, and is e.g. described by Anderson [7] (sec. 3.13) for a cylindrical body and is called *D'Alembert's Paradox*. The basic reason for a net zero drag and lift is that viscous effects are neglected. Furthermore, in a potential flow solution, the trailing edge of a hydrofoil is circulated around without an additional boundary condition and the aft stagnation point is situated on the suction side. This results in an infinite velocity at the sharp trailing edge because its radius is zero. Moreover, the total circulation Γ produced by a closed and connected body must be zero due to *Kelvin's Theorem*, which is described by Katz and Plotkin [51](sec. 2.3) and Carlton [20] (sec. 7.5). In reality, a so-called free circulation Γ_W is transported into the trailing flow field of a hydrofoil. It is modelled by a wake sheet with a circulation that equals the bound circulation Γ_H of the hydrofoil as displayed in Figure 3.3.

In order to obtain a finite velocity at and to move the aft stagnation point towards the trailing edge, a boundary condition has to be enforced. This is the Kutta condition

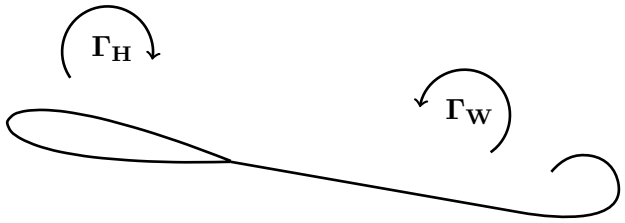

Figure 3.3.: Circulation of a hydrofoil (Γ_H) and its trailing wake surfaces (Γ_W)

and it states that there is a circulation leaving the hydrofoil at the trailing edge. The strength of the condition depends on the body's circulation and is chosen in a way that the flow leaves the trailing edge smoothly and the velocity is finite. The free circulation, together with the bound circulation on the body is, according to Kelvin's theorem, again zero, but the body itself is subject to lift and drag forces.

free surface influence

When looking at the free water surface, a significant difference between the steady and unsteady formulation of the equations becomes obvious. In the steady case, the combined b.c (3.43) can be substituted into the equation for the free surface potential (3.32) and it becomes

$$\Phi_{FS} = -\frac{1}{4\pi}\int_{S_{FS}} \frac{\mathbf{v}^2}{g}\nabla\nabla\Phi\left(\frac{1}{r}\right)dS_{FS} - \frac{1}{4\pi}\int_{S_{FS}} \Phi\frac{\partial}{\partial n}\left(\frac{1}{r}\right)dS_{FS}. \tag{3.61}$$

Now, this equation is solved using the Dirichlet formulation of the BVP and by shifting the collocation point slightly downwards so it is inside the computation domain $\mathbb{V}$. When implementing this into a solution process, a straightforward approach is to solve the free surface potential in an extra equation system and to account for other bodies on the RHS

$$-\frac{1}{4\pi}\int_{S_{FS}} \Phi\frac{\partial}{\partial n}\left(\frac{1}{r}\right)dS_{FS} - \frac{1}{4\pi}\int_{S_{FS}} \frac{1}{g}\mathbf{v}^2\nabla\nabla\Phi\left(\frac{1}{r}\right)dS_{FS} = RHS. \tag{3.62}$$

After the solution of the potential Φ on the free surface, the elevation is determined using the dynamic b.c. (3.38). These two steps can be iterated until the problem is converged.

In an unsteady case, the two boundary conditions at the free surface need to be stepped forward in time. The unknown potential Φ and elevation ζ can be determined using

Equations (3.46) and (3.47). The unknown source strength $\frac{\partial \Phi}{\partial n}$ at the free surface is determined in the equation system using the known doublet strength Φ

$$\frac{1}{4\pi}\int_{S_{FS}} \frac{1}{g}\frac{\partial \Phi}{\partial n}\left(\frac{1}{r}\right) dS_{FS} = \frac{1}{4\pi}\int_{S_{FS}} \Phi \frac{\partial}{\partial n}\left(\frac{1}{r}\right) dS_{FS} + RHS. \tag{3.63}$$

wave potential

One way of accounting for an effect due to waves is to superpose a wave potential to other potentials present in the flow domain. The wave potential used in the present method is that of a regular, long crested wave in deep water according to the linear wave theory (see e.g. Journée and Massie [50], sec. 5.2). In this theory, the water waves are approximated as sinusoidal elevation of the free surface. A deep water case can be assumed when the water depth h is larger than half the wavelength L_w due to the dispersion relation [2]. The potential of a three-dimensional wave having the global travel direction γ reads

$$\Phi_{Wave}(x, y, z, \gamma, t) = \frac{H_w g T_w}{4\pi} e^{kz} \cos\left[\omega t - k(x\cos(\gamma) + y\sin(\gamma))\right] \tag{3.64}$$

using the wave height H_w, the wave period $T_w = \frac{2\pi}{\omega}$ and the wave number $k = \frac{2\pi}{L_w}$. The still water surface is located in the xy-plane, the z-axis is pointing upwards (out of the water) and $P(x, y, z) \in \mathbb{V}$ is either a submerged point or located directly at the free water surface. The derivatives of the potential, with respect to the coordinate system, provide the orbital velocities in the respective direction:

$$\frac{d\Phi_{Wave}}{dx} = v_x = -\frac{H_w g T_w}{4\pi} e^{kz} \sin[\omega t - k(x\cos(\gamma) + y\sin(\gamma))] k\cos\gamma, \tag{3.65}$$

$$\frac{d\Phi_{Wave}}{dy} = v_y = -\frac{H_w g T_w}{4\pi} e^{kz} \sin[\omega t - k(x\cos(\gamma) + y\sin(\gamma))] k\sin\gamma, \tag{3.66}$$

$$\frac{d\Phi_{Wave}}{dz} = v_z = \frac{H_w g T_w}{4\pi} k e^{kz} \cos[\omega t - k(x\cos(\gamma) + y\sin(\gamma))]. \tag{3.67}$$

Now, when many sine waves having different amplitudes, lengths, periods, propagation directions and phase shifts are superposed, an irregular seaway can be composed. In the present method, this is done by discretising an energy wave spectrum

$$S_\zeta(\omega) = \varrho g S_\zeta(\omega_i)\Delta\omega. \tag{3.68}$$

[2] The dispersion relation correlates the wave height to its length and it reads $\omega^2 = kg \cdot tanh(kh)$. The value of the *tanh*- function is approx. one for arguments larger or equal π, so the dispersion becomes independent of the water depth for values larger than $h \approx 0.5 L_w$.

Using the energy E of a wave

$$E = \frac{1}{2}\varrho g|\hat{A}_j|^2 \tag{3.69}$$

we get a formulation for the wave amplitude $\hat{A}_j$:

$$|\hat{A}_j| = \sqrt{2 \cdot S_\zeta(\omega_j)\Delta\omega}. \tag{3.70}$$

A natural seaway usually has a dominating propagation direction, which is called γ_0 in the following. In order to get short crested waves, the wave energy is distributed over a range of directions $[\gamma_0 - 90°, \ldots, \gamma_0 + 90°]$. The energy is distributed around the global travel direction by the function $p(\gamma)$, by

$$S_\zeta(\omega_i, \gamma_j) = p_m(\gamma) \cdot S_\zeta(\omega_i), \tag{3.71}$$

which is a probability function. Two possible functions,

$$p_1(\gamma) = \frac{2}{\pi}\cos^2([(\gamma_0 - \frac{\pi}{2}), \ldots, (\gamma_0 + \frac{\pi}{2})]) \quad \text{and} \tag{3.72}$$

$$p_2(\gamma) = \frac{8}{3\pi}\cos^4([(\gamma_0 - \frac{\pi}{2}), \ldots, (\gamma_0 + \frac{\pi}{2})]) \tag{3.73}$$

are implemented, allowing to distribute the spectrum energy wider with a lower peak (p_1) or closer around γ_0 with a higher peak (p_2). A statistical phase shift $\tau[0, 2\pi]$ is introduced for each long-crested wave to result in a stochastical superposing of the elementary waves. The potential for the irregular sea reads

$$\Phi_{Seaway}(x, y, z, \gamma, t) = \sum_{i=0}^{I}\sum_{j=0}^{J} \frac{H_{w,i} g T_{w,i}}{4\pi} e^{k_i z} \cos\left[\omega_i t - k_i(x\cos(\gamma_j) + y\sin(\gamma_j)) + \tau_{i,j}\right] \tag{3.74}$$

Here i and j are the indices of the elementary waves and the travel directions, respectively. The value of $\Delta\omega = \omega_{i+1} - \omega_i$ is the increment of the spectrum in ω-direction and $\Delta\gamma_j = \gamma_{j+1} - \gamma_j$ in γ-direction. The free surface height for the irregular, short crested waves becomes

$$\zeta(x, y, \gamma, t) = \sum_{i=0}^{I}\sum_{j=0}^{J} \sqrt{2 \cdot S_\zeta(\omega_i, \gamma_j)\Delta\omega\Delta\gamma_j}\ \cos[\omega_i t - k_i(x\cos(\gamma_j) + y\sin(\gamma_j)) + \tau_{i,j}]. \tag{3.75}$$

computation of forces

The pressure at any point located in $\mathbb{V}$ can be computed with the Bernoulli Equation (3.18). In the context of a potential flow the right hand side of (3.18) is constant in the whole flow field and the equation can be set up for two locations in $\mathbb{V}$

$$\frac{1}{2}v_2^2 + \frac{p_2}{\rho} + gz_2 + \frac{\partial \Phi_2}{\partial t} = \frac{1}{2}v_1^2 + \frac{p_1}{\rho} + gz_1 + \frac{\partial \Phi_1}{\partial t}. \tag{3.76}$$

Now, let location 2 be the point of interest and point 1 be a position where the induced potential Φ_{ind} due to the body and to external potentials Φ_{ext} have decayed. Both points are moving with the body's motion velocity and the equation is stated in the moving frame of reference in line with the potential definition (3.34). Therefore, the motion induced potential and velocity effects are negative. In point 1 only the motion is present, whereas in point 2 induced potential and velocity entries from all effects employed in $\mathbb{V}$ are inherited. The pressure $\Delta p = p_2 - p_1$ becomes

$$\Delta p = -\frac{1}{2}\rho \left(\nabla \Phi_{ind} - \mathbf{v}_M + \nabla \Phi_{ext}\right)^2 + \frac{1}{2}\rho \mathbf{v}_M^2 - \rho g \Delta z - \rho \frac{\partial (\Phi_{ind} - \Phi_M + \Phi_{ext})}{\partial t}. \tag{3.77}$$

The term Δz refers to the immersion of point 2, which is determined towards the local elevation of the water surface in gravitation direction.

The pressure forces acting on the surface of a body are determined using the pressure and the local panel geometry for all L panels. The sign of the pressure force is negative because the force acting on the body is of interest and the local normal vector is pointing outwards:

$$\mathbf{F}_{press} = \sum_{i=0}^{L} \mathbf{F}_{press,i} = \sum_{i=0}^{L} -\Delta p_i \cdot A_i \cdot \mathbf{n}_i. \tag{3.78}$$

viscous effects

Due to the application of Laplace's Equation (3.7), the flowfield is defined as non-viscous. But the forces due to viscous effects can contribute significantly to the total forces acting on hydrofoils or ship propellers. Therefore, a friction force can be determined to improve the calculated results. In the context of the present method, the friction forces are referred to as corrections to the purely potential flow solution.

One possible correction is based on local resistance coefficients per unit area of flat plates, as e.g. published by Saunders [79] (sec. 5.14). For local Reynolds Numbers $Re_x \leq 1e^{-5}$, the flow is considered as laminar and the friction drag coefficient $c_{f,l}$ is used, whereas for turbulent flow ($Re_x > 1e^{-5}$) the coefficient is $c_{f,t}$,

$$c_{f,l} = 0.664 \cdot Re^{-0.5} \quad \text{and} \quad c_{f,t} = 0.059 \cdot Re^{-0.2}, \tag{3.79}$$

$$\text{using} \quad Re_x = \frac{v \cdot l}{\nu}. \tag{3.80}$$

The friction force $\mathbf{f}_f$ acting on a local (discretised) part of the surface area is

$$\mathbf{f}_f = c_f \cdot \frac{\rho}{2} \cdot \mathbf{v}^2. \tag{3.81}$$

When model scale propellers are investigated, a significant laminar portion of the boundary layer normally occurs and this method is reasonable. For full-scale propellers, the laminar region is insignificant and a fully turbulent boundary layer can be assumed. The correction is only valid for hydrofoils or propellers having moderate angles of attack, so no flow separation occurs.

3.2.4. Numerical Treatment

In this section, a numerical procedure to solve the integral equations describing a potential flow field is discussed. In a first step, the boundaries of the flow volume $\mathbb{V}$ introduced earlier are discretised into panels, for which the geometric properties are given. In this method, the finite surface fractions refer to quadrilateral panels, so all panel edges must be straight lines. Following Katz and Plotkin [51], this refers to a first-order geometrical approximation. The singularities have a constant strength over one panel, so the discretisation of singularity elements is of zero-order. The method refers to a low-order *BEM*. A typical problem in the context of this work is a hydrofoil under a free water surface, as depicted in Figure 3.4. The hydrofoil, its trailing wake surfaces and the free water surface are discretised with panels. Each panel influences values of velocity or potential on all other panels, which are determined in order to construct a common solution to the *BVP*, for which the equations are discretised and a sum is formulated. One of the different methods discussed in Section 3.2.3 can be used to set up a matrix and to solve this matrix for the unknown values.

The boundaries of the trailing wake and the free water surface need to be treated separately because they are not rigid like the bodies bounding surfaces. The trailing wake is defined as force-free and is deformed due to the local total velocities. The boundary of the free surface deforms due to the fluid pressure as stated in the dynamic b.c. (3.46). Numerical instabilities may occur when the influence of other boundaries on the free surface is large. So if a body is slightly below the surface, a damping of the influence is needed. If a body is penetrating the water surface, some parts of the geometry are emerged out of the water and leave the flow domain $\mathbb{V}$. The panels describing the emerged geometry must be excluded from the computation and the size of the matrix is reduced. The boundary of the free water surface is, in the unsteady case, sensitive to the time-stepping procedure, which will be discussed later.

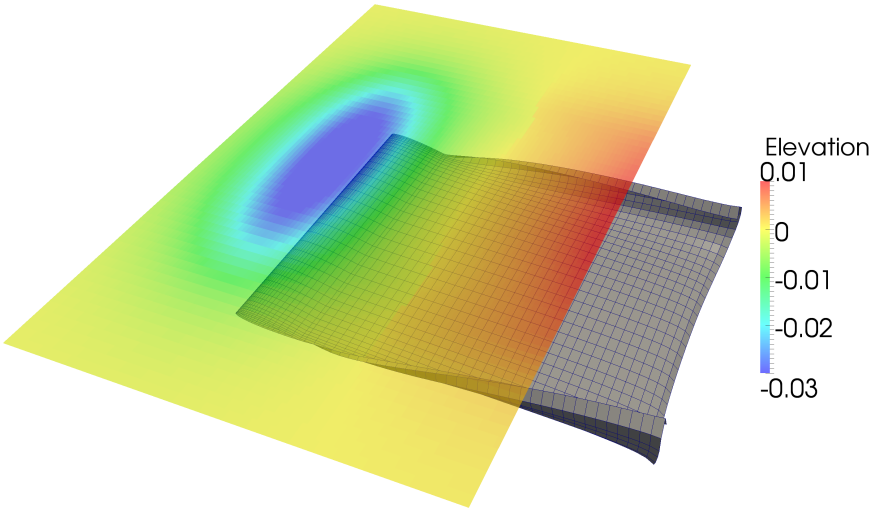

Figure 3.4.: Three-dimensional view of a NACA0012-hydrofoil at 10° angle of attack under a free water surface

panel geometry

When discretising a bounding surface with panels, the first step is to generate a grid of points, each of them located on the surface. In between the points, quadrilateral surfaces are built up with a right-handed numbering of points and edges as displayed in Figure 3.5. For several mathematical operations it is convenient to describe the panels in a local coordinate system (ξ, η, ψ). The normal vector $\mathbf{n}$ points in the local ψ-direction and is determined to be the normed sum of the normal vectors of the two triangles in which the panel can be split. Each of the triangle normal vectors are computed via the vector product of two of its edges. The ξ-axis is defined as the longest edge of the panel, which refers to e_2 in Figure 3.5. The η-axis is orthogonal to the ξ-axis and the normal vector. Both, the ξ- and the η-axis lie in the panel plane. The centre of the panel is determined by the weighted sum of the centres of both triangles and the panel area is the sum of the area of both triangles.

A quality criterion for the geometry of panels is introduced, consisting of its orthogonality and aspect ratio. The orthogonality is determined using the relation between the panels area and the square of the maximum bounds of the panel in the local coordinate system. For a nearly orthogonal panel, the panel quality equals the orthogonality, and even an elongated panel can have a perfect quality[3]. In the case of an orthogonality be-

[3] Here the assumption is made, that the flow is directed in one of the panels local coordinate directions.

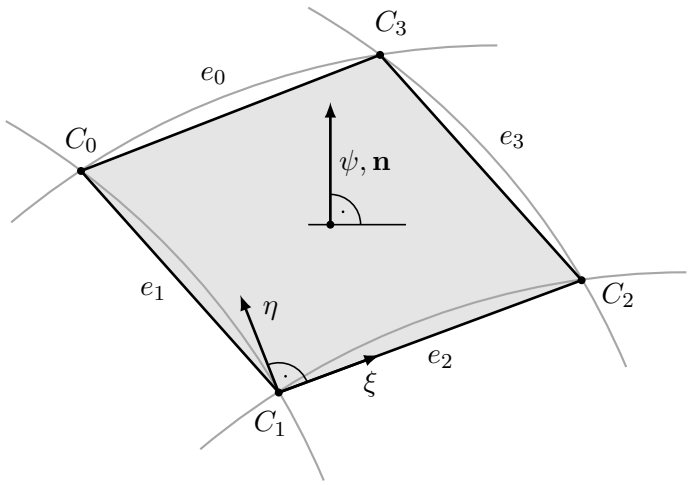

Figure 3.5.: Geometry definition of a quadrilateral surface panel and its local coordinate directions

low 0.9, the panel quality is the product of its orthogonality and an aspect ratio quality. This is determined by the relation between the minimum and the medium edge length of the panel. So, if a panel is stretched and non-orthogonal, the penalty is higher.

influence functions

With the influence functions, the induced potential and velocity due to the source and doublet strength of one panel on an arbitrary point $P(x, y, z)$ can be determined. The formulations used here were first derived by Hess and Smith [42] for a constant source distribution over a flat panel liing in the ξ-η-plane of a local coordinate system. Analytical formulas can also be found in the work of Newman [73] or Katz and Plotkin [51] (sec. 10.4) for a constant source distribution over a panel and a vortex ring element around the panel edges. Of course, the assumption of quadrilateral panels is only an approximation, because for three-dimensional geometries, the panels are not necessarily flat and untwisted. The influence coefficients only depend on the panels' geometry and its singularity strengths. The total induced velocity or potential is the sum of the influence coefficients of all panels on P. A panel does not necessarily have to be four-edged and can, in general, be a flat polygon with n corners and the integration would have to be carried out over n edges.

If this is not the case, an error would be made using the introduced criterions. Hence the user has to choose the grid according to the flow field he/she expects.

The induced potential and velocities are derived in a local, right-handed coordinate system for a flat panel in the ξ-η-plane with a normal vector pointing in the negative ψ-direction, which is different than the local coordinate directions shown in Figure 3.5. A left-handed numbering of corners and edges results. The potential induced by one panel with constant source strength in P following Equation (3.50) is $\phi_s(\xi, \eta, \psi)$, with

$$\phi_S = \frac{-\sigma}{4\pi} \int_S \left[(\xi - \xi_0)^2 + (\eta - \eta_O)^2 + \psi^2\right]^{-\frac{1}{2}} dS. \tag{3.82}$$

The constant distribution of source strength is integrated over the panel area and transferred to a formulation using four straight edges[4] in the case of a four-edged panel, which is given in the appendix in Equation (A.1). The velocity components induced by the panel are derived by differentiating the velocity potential in the three coordinate directions (see Equations A.7, A.8 and A.9).

For a panel with a constant doublet strength distribution over its surface area, the induced potential at P following Equation (3.51) reads

$$\phi_D = \frac{-\mu}{4\pi} \int_S \psi \left[(\xi - \xi_0)^2 + (\eta - \eta_O)^2 + \psi^2\right]^{-\frac{3}{2}} dS. \tag{3.83}$$

Again, the area-based formulation is transferred to an edge-based and the quadrilateral is represented by four straight line vortices forming a vortex ring. The induced potential is given in Equation (A.10) and the induced velocities in equations (A.11), (A.12) and (A.13).

In the near field when the distance between P and the panel edges is small, numerical instabilities can occur. When the distance approaches zero, the u- and v-components of the velocity would become infinite, so the influence is constrained. In the far field, the influence is independent of the panel geometry and the source or doublet distribution over the panel can be simplified to a point singularity. The formulation for the source-induced potential reads

$$\phi_S = \frac{-\sigma A_0}{4\pi\sqrt{(\xi - \xi_0)^2 + (\eta - \eta_O)^2 + \psi^2}}, \tag{3.84}$$

using A_0, the surface area of the adjacent panel. The velocities induced by a point source can be found in Equation (A.14). It is obvious, that this operation is much faster than the near field solution, which results in a greatly reduced simulation time when the far field solution is used. The formulation for the doublet-induced potential becomes

$$\phi_D = \frac{-\mu\psi A_0}{4\pi[(\xi - \xi_0)^2 + (\eta - \eta_O)^2 + \psi^2]^{\frac{3}{2}}} \tag{3.85}$$

[4] For details please refer to Hess and Smith [42] (sec. 4.4).

The velocities induced by a point doublet are derived in Equation (A.15). The distance from which the far field solution can be used is given by Katz and Plotkin [51] as three to five average panel diameters. This value can be confirmed based on the simulation conducted within this work.

In order to further reduce computational effort, it is possible to use a symmetric or periodic boundary condition. It is assumed that the singularity strength distribution is the same for all symmetric or periodic parts. The symmetric or periodic boundary is expressed in such way that the velocity induced by a panel with this type of boundary also includes the velocity induced by its equivalents. This leads to a much smaller set of linear equations and significantly reduces the computational time. A typical case making use of a symmetrical setup is a propeller in open water conditions, where simulating one blade is sufficient to compute the total forces and moments.

composing a matrix

In the following, the numerical representation of the *Dirichlet* formulation of the *BVP* with the collocation point inside the body according to Equation (3.60) is presented. If the body's surface is discretised with N_B quadrilateral panels and the wake of the body with N_W panels, the integral equation can be transferred to a summation over all panels and the governing equation in a collocation point $P(x_j) \in \mathbb{V}$ becomes

$$\sum_{k=1}^{N_B} C_k(x_j)\mu_k + \sum_{l=1}^{N_W} C_l(x_j)\mu_l = -\sum_{k=1}^{N_B} B_k(x_j)\sigma_k, \tag{3.86}$$

$$\text{with} \quad C_k(x) \mathrel{\hat{=}} \phi_D \quad \text{and} \quad B_k(x) \mathrel{\hat{=}} \phi_S, \tag{3.87}$$

following Equations (3.84) and (3.85). Equation (3.86) derived above outlines the influence of all panels on the adjacent panel k with its collocation point $P(x_j)$ and hence represents one row of the matrix for the determination of unknown doublet strengths. The *BVP* is set up for N_B body panels and N_W wake panels, and the following equation system results

$$\begin{aligned} &\begin{pmatrix} C_{1,1} & \cdots & C_{1,N_B+N_W} \\ \vdots & \vdots & \vdots \\ C_{N_B+N_W,1} & \cdots & C_{N_B+N_W,N_B+N_W} \end{pmatrix} \cdot \begin{pmatrix} \mu_1 \\ \vdots \\ \mu_{N_B+N_W} \end{pmatrix} \\ = -&\begin{pmatrix} B_{1,1} & \cdots & B_{1,N_B} \\ \vdots & \vdots & \vdots \\ B_{N_B+N_W,1} & \cdots & B_{N_B+N_W,N_B+N_W} \end{pmatrix} \cdot \begin{pmatrix} \sigma_1 \\ \vdots \\ \sigma_{N_B+N_W} \end{pmatrix} \end{aligned} \tag{3.88}$$

This equation system is not closed since we have $N_B + N_W$ unknowns and only N_B boundary conditions imposed on the body panels. Therefore, an additional condition is needed. This is the Kutta condition, the physical meaning of which has been discussed in Section 3.2.3 and which, at the trailing edge of an airfoil, requires the flow to leave the body tangentially. So, the position of the trailing edge has to be prescribed when setting up a simulation case and a mathematical formulation, which suppresses a cross flow, has to be applied. In a two-dimensional case, this can be achieved easily if the vortex strength at the trailing edge is set to zero. If there is no vortex remaining, the velocity and thus the pressure will be equal on both sides of the trailing edge. This is enforced by setting the doublet strength of the first panel in the trailing wake (μ_{TE}) according to the doublet strengths of the aftmost panels μ_U and μ_L on the upper and lower side of the body surface

$$\mu_{TE} = \mu_U - \mu_L. \tag{3.89}$$

Hence, if a panel is located directly at the trailing edge of the airfoil, its doublet strength is affected by the first trailing panel in the wake and the influence coefficient C_{TE} becomes

$$C_{TE}\mu_{TE} = C_{TE}\left(\mu_U - \mu_L\right). \tag{3.90}$$

Using the formulation above, the influence coefficient of the wake panel can be substituted in the matrix row belonging to the adjacent body panels with

$$A_L = C_L - C_{TE} \quad \text{and} \quad A_U = C_U + C_{TE}. \tag{3.91}$$

The resulting equation system reduces to N_B equations and unknowns, so it can be solved for the unknowns μ_k

$$\begin{pmatrix} A_{1,1} & \dots & A_{1,N_B} \\ \vdots & \vdots & \vdots \\ A_{N_B,1} & \cdots & A_{N_B,N_B} \end{pmatrix} \cdot \begin{pmatrix} \mu_1 \\ \vdots \\ \mu_{N_B} \end{pmatrix} = - \begin{pmatrix} B_{1,1} & \dots & B_{1,N_B} \\ \vdots & \vdots & \vdots \\ B_{N_B,1} & \cdots & B_{N_B,N_B} \end{pmatrix} \cdot \begin{pmatrix} \sigma_1 \\ \vdots \\ \sigma_{N_B} \end{pmatrix}. \tag{3.92}$$

As is apparent from the statements above, the Kutta condition used here is only physically correct when the flow follows the grid rows in a hydrofoil- or propeller blade-simulation. This is met in most hydrofoil applications. In a 3D-flow situation, the velocity component parallel to the trailing edge may be different on both sides, which may lead to a pressure difference at the trailing edge of propeller blades. Though this method is chosen quite often for marine propeller applications (see e.g. Kinnas et al. [54]), the error might be large if the velocity components parallel to the trailing edge have a significant value. This can be the case for highly skewed propellers or others where the main parameters vary strongly with radius. The error can be reduced when an adapted grid is chosen according to the expected flow situation.

In such cases, an improvement can be achieved if a different Kutta condition is applied. This should directly lead to pressure equality at the trailing edge and not imply it.

Hence a scheme originally introduced by Kerwin et al. [52] was implemented and discussed by Hundemer [45]. An initial linear condition is used and an additional potential is calculated in a non-linear, iterative manner. The solution is non-linear, as the relation between the linear calculated potential and the pressure on the blade is, according to the Bernoulli equation, of quadratic type. To find such a non-linear solution, the gradient of the pressure difference at the trailing edge due to a change of the wake potential is calculated and used as an input for a Newton-Raphson method. This scheme minimises the remaining pressure difference at the trailing edge by adding a radially adapted potential, that fulfils the normal b.c. on the blade and the pressure equality on suction and pressure side. Because the convergence behaviour of the scheme is not satisfying, it is not used in this method.

treatment of the trailing wake

Due to the different nature of the flow field in steady and unsteady simulations, the wake-field aft of a hydrofoil has to be treated differently in both situations. In a steady flow situation, it is convenient to set the strength of all wake panels originating from one panel at the trailing edge of a hydrofoil to a constant value. This is because one row of wake panels represents the change of trailing vorticity over time, which only changes during the iteration process depending on the initial solution and must be constant in time for steady flow. The location of the trailing wake panels is a priori unknown and has to be determined in an iterative manner until it follows streamlines starting from the trailing edge. At the beginning of each iteration, the corners of the wake panels are shifted. To do this, the induced velocities from all panels (all singularities) present in the simulation domain have to be calculated. With these velocities, the new corner positions are determined. Because the panel doublet distribution is transformed to a vortex ring element as described above, the induced velocity in a corner is not defined, and an interpolation using the induced velocities in the surrounding panel centres is used. Following the direction of the streamlines, the induced velocity interpolated from two neighbouring panel centres (see M_{PS} and M, or M and M_{STB} in Figure 3.6, respectively) is used to move the trailing corner of the edge between the adjacent panels. This refers to corners C_1 and C_2 of the highlighted wake panel in Figure 3.6.

In case of an unsteady simulation, the motion of the hydrofoil or the free-stream velocity changes with time, so the strength of one panel row in the trailing wake cannot be set to a constant value. Hence, in every time step the trailing vorticity, together with the wake panels, are transported away from the hydrofoil and a new row of panels is inserted at the trailing edge. The strength of the new panels has to be determined and the strengths of the panels already existing in the wake remain constant. Because the circulation is transported away from the hydrofoil in the unsteady situation, the

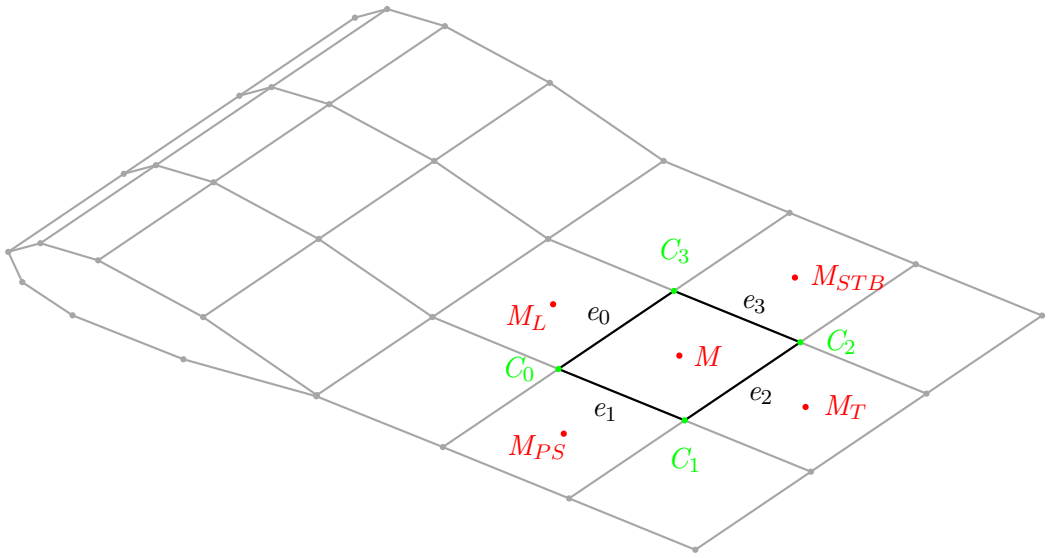

Figure 3.6.: Geometric description of a wake panel and relation to its neighbours. The panel midpoints (M), corners (C) and edges (e) are depicted. The subscripts L, T, PS and STB denote *leading*, *trailing*, *portside* and *starboard* neighbours.

distortion of the leading corners C_0 and C_3 of each wake panel is determined using the induced velocity in the displayed panel centres. The edges are shifted after half the time step when they are in the position at which the induced velocities are calculated. A representative simulation result showing a 3-D hydrofoil and its trailing wake surfaces is depicted in Figure 3.7.

The method using induced velocities as described above cannot be applied to the sides of the trailing wake sheet, because no interpolation partners exist. The scheme described by Hundemer [45] is used, which interprets the outmost edge row in length direction as a vortex filament rotating around its inner neighbour edge row starting at the trailing edge of the hydrofoil. When one panel is considered, the length of edge e_0 defines the distance between the vortices. The strength of the circulation is the difference between the doublet strengths of the panel and its sidewise neighbour. An angle is determined using this circulation, the distance between the vortices and the length of the panel. To prevent unphysical behaviour resulting from discretisation effects, such as large panel areas, the value of the angle is bounded. Finally, the position of the aft corner C_1 (for portside edges) or C_3 (for starboard edges) is set and the next trailing panel in streamwise direction is treated.

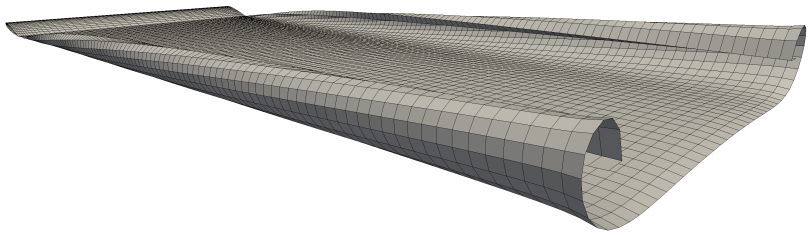

Figure 3.7.: Geometry of the wake panels aft of a 3-D NACA0012-hydrofoil at 12° angle of attack

free surface treatment

On a free water surface, the boundary conditions derived in Section 3.2.2 are applied. In the case of a steady simulation, the combined b.c. (3.43) is used and the following free surface potential Equation (3.61) can be constructed

$$\Phi_{FS}(P) = -\frac{1}{4\pi}\int_{S_{FS}} \left(\frac{1}{r}\frac{1}{g}\mathbf{v}_M^2\nabla^2\mu + \mu\frac{\partial}{\partial n}\frac{1}{r}\right) dS_{FS}. \tag{3.93}$$

The unknown doublet strength μ can be determined in the *SLE*. The discretised form of the free surface potential, following the notation of Equation (3.86), becomes

$$\phi_{FS,j} = \sum_{m=0}^{N_{FS}} C_m(x_j)\phi_m - \sum_{m=0}^{N_{FS}} \frac{\mathbf{v}_M^2}{g} B_m(x_j)\frac{\partial^2\phi_m}{\partial x^2}. \tag{3.94}$$

This formulation inherits the second spatial derivative of the potential $\frac{\partial^2\phi_m}{\partial x^2}$ induced from all N_{FS} panels in each panel collocation point j, which is determined by using a scheme twice that was introduced by Dawson [24] for a first derivative of the potential. This concept is described by Bal and Kinnas [8] and is implemented in the following

$$\frac{\partial^2\phi_j}{\partial x^2} = \frac{\partial \mathbf{v}_j}{\partial x} = CA_j u_j + CB_j u_{j-1} + CC_j u_{j-2} + CD_j u_{j-3}. \tag{3.95}$$

Here, the subscript j denotes for the position of a panel and $j-1$ for the upstream neighbour. The factors CA, CB, CC and CD are computed from the distances between the four collocation points[5]. The derivative is set up in the body's motion direction

[5] The determination of CA, CB, CC and CD is given by Dawson [24].

$\mathbf{v}_M$ in the assumption that the flow is directed mainly in that direction. Hence, the x-direction of the free surface has to be parallel to $\mathbf{v}_M$, so the velocities given in Equation (3.95) can be determined by

$$u_j = \frac{\partial \phi_j}{\partial x} = CA_j\phi_j + CB_j\phi_{j-1} + CC_j\phi_{j-2} + CD_j\phi_{j-3} \tag{3.96}$$

and Equation (3.95) becomes

$$\begin{aligned}\frac{\partial^2 \phi_j}{\partial x^2} =& CA_j \cdot (CA_j\phi_j + CB_j\phi_{j-1} + CC_j\phi_{j-2} + CD_j\phi_{j-3}) \\ &+ CB_j \cdot (CA_{j-1}\phi_{j-1} + CB_{j-1}\phi_{j-2} + CC_{j-1}\phi_{j-3} + CD_{j-1}\phi_{j-4}) \\ &+ CC_j \cdot (CA_{j-2}\phi_{j-2} + CB_{j-2}\phi_{j-3} + CC_{j-2}\phi_{j-4} + CD_{j-2}\phi_{j-5}) \\ &+ CD_j \cdot (CA_{j-3}\phi_{j-3} + CB_{j-3}\phi_{j-4} + CC_{j-3}\phi_{j-5} + CD_{j-3}\phi_{j-6})\end{aligned} \tag{3.97}$$

$$\begin{aligned}=& CA_j^2\phi_j + (CA_j \cdot CB_j + CB_j \cdot CA_{j-1})\phi_{j-1} \\ &+ (CA_j \cdot CC_j + CB_j \cdot CB_{j-1} + CC_j \cdot CA_{j-2})\phi_{j-2} \\ &+ (CA_j \cdot CD_j + CB_j \cdot CC_{j-1} + CC_j \cdot CB_{j-2} + CD_j \cdot CA_{j-3})\phi_{j-3} \\ &+ (CB_j \cdot CD_{j-1} + CC_j \cdot CC_{j-2} + CD_j \cdot CB_{j-3})\phi_{j-4} \\ &+ (CC_j \cdot CD_{j-2} + CD_j \cdot CC_{j-3})\phi_{j-5} + CD_j \cdot CD_{j-3}\phi_{j-6}.\end{aligned} \tag{3.98}$$

This second derivative uses six upstream collocation points. When the *SLE* is set up, the terms given in Equation (3.98) are determined subsequently. So, for each panel j representing one line in the *SLE*, the corresponding ϕ-terms of downstream-situated panels can be assigned. When using constant grid spacing, the complexity can be greatly reduced because the factors CA, CB, CC and CD are constant for all panels. The derivatives become

$$\frac{\partial^2 \phi_j}{\partial x^2} = CAu_j + CBu_{j-1} + CCu_{j-2} + CDu_{j-3} \tag{3.99}$$

$$\begin{aligned}=& CA^2\phi_j + (CA \cdot CB + CB \cdot CA)\phi_{j-1} \\ &+ (CA \cdot CC + CB \cdot CB + CC \cdot CA)\phi_{j-2} \\ &+ (CA \cdot CD + CB \cdot CC + CC \cdot CB + CD \cdot CA)\phi_{j-3} \\ &+ (CB \cdot CD + CC \cdot CC + CD \cdot CB)\phi_{j-4} \\ &+ (CC \cdot CD + CD \cdot CC)\phi_{j-5} + CD \cdot CD\phi_{j-6}\end{aligned} \tag{3.100}$$

$$\begin{aligned}=& \frac{25}{9(\Delta x)^2}\phi_j - \frac{25}{3(\Delta x)^2}\phi_{j-1} + \frac{115}{12(\Delta x)^2}\phi_{j-2} - \frac{50}{9(\Delta x)^2}\phi_{j-3} \\ &+ \frac{11}{6(\Delta x)^2}\phi_{j-4} - \frac{2}{6(\Delta x)^2}\phi_{j-5} + \frac{1}{36(\Delta x)^2}\phi_{j-6}\end{aligned} \tag{3.101}$$

This differencing scheme is strongly upwind-directed, so no upstream waves occur even at slow speeds. Because six panels in the upstream direction are needed, the scheme is only applied from the seventh row of panels and on their downstream neighbours. It is not applied on both panel columns at the outer sideways borders to supress wave reflections.

After solving the *SLE*, the unknown values ϕ and $\frac{\partial \phi}{\partial n}$ are set in the collocation point of each panel and the free surface elevation ζ is determined. Following Equation (3.38), the linearised free surface elevation becomes

$$\zeta = -\frac{1}{g}\mathbf{v}_M \nabla \mu = -\frac{1}{g}\mathbf{v}_M \frac{\partial \phi_{FS}}{\partial x}. \tag{3.103}$$

The term $\frac{\partial \phi_{FS}}{\partial x}$ is determined using a central differencing scheme, which cannot be established at the last panel row in the downstream direction. For this panel row the elevation is zero.

In the unsteady case, analogue to unsteady simulations without the free water surface, the coordinate system is defined as moving along with the body of interest. In contrast to the steady b.c., the boundary conditions are not combined in the unsteady case. In the *SLE*, the unknown quantity is $\frac{\partial \phi}{\partial n}$ and the remaining two unknowns, the potential ϕ and the free surface elevation ζ, are determined with the free surface boundary conditions. Therefore, these are reorganised and Equations (3.46) and (3.47) are used. Here, the partial time derivatives of the unknowns can be stepped forward in time, which is done using a fourth-order Runge-Kutta iteration method. In the literature, several other methods are described, e.g. predictor-corrector schemes, or those based on a Taylor-series expansion. A review and numerous references are given by Grilli [37] (ch. 1). In this work, the classical Runge-Kutta method (see Bronstein [12], sec. 19.4.1.2), as e.g. described by Vinayan [97], for free surface flows is used. In order to determine the variables correctly for this method, four supporting points referring to the order of the scheme are needed and the *BVP* has to be solved four times within one time step. The initial values for the potential ϕ and the free surface elevation ζ are *zero* in the first time step and for every consecutive $t_m = t_{m-1} + \Delta t$, the values of the last are used. Those of the actual time step are determined by

$$\zeta_m = \zeta_{m-1} + \Delta t \sum_{j=1}^{4} b_j k_{\zeta,j} \tag{3.104}$$

$$\text{and} \quad \phi_{ind,m} = \phi_{ind,m-1} + \Delta t \sum_{j=1}^{4} b_j k_{\phi,j}, \tag{3.105}$$

using the coefficients b_j, which are determined based on a Taylor-series expansion given by Bucher [15] (ch. 3), and the values of the ζ- and ϕ-equations determined on the

intermediate time levels $k_{\zeta,j}$ and $k_{\phi,j}$. Because the potential flow field has to be solved four times on these time levels, intermediate values ζ_i and $\phi_{ind,i}$ are computed after solving the *SLE* by

$$\zeta_i = \zeta_{m-1} + \Delta t \sum_{j=1}^{i} a_{ij} k_{\zeta,j}, \qquad \text{for } i \in [1:4] \tag{3.106}$$

$$\text{and} \quad \phi_{ind,i} = \phi_{ind,m-1} + \Delta t \sum_{j=1}^{i} a_{ij} k_{\phi,j}, \qquad \text{for } i \in [1:4], \tag{3.107}$$

using the control variable i for the actual intermediate iteration step. The factors a_{ij} result from the Taylor-series formulation[6] and they read

$$A = \begin{pmatrix} 0 & 0 & 0 & 0 \\ 0.5 & 0 & 0 & 0 \\ 0 & 0.5 & 0 & 0 \\ 0 & 0 & 1 & 0 \end{pmatrix} \tag{3.108}$$

The intermediate function values are defined using the free surface boundary conditions and are determined by

$$k_{\zeta,j} \equiv \frac{\partial \zeta_i}{\partial t} = -\frac{\partial(\phi_{ind} + \phi_{ext})}{\partial z} + (\nabla \phi_{ind,i} - \mathbf{v}_M + \nabla \phi_{ext}) \cdot \nabla \zeta \tag{3.109}$$

$$\text{and} \quad k_{\phi_{ind,j}} \equiv \frac{\partial \phi_{ind,i}}{\partial t} = -\frac{1}{2} (\nabla \phi_{ind,i} - \mathbf{v}_M + \nabla \phi_{ext})^2 + g\zeta + \frac{1}{2} (\mathbf{v}_M)^2 + \frac{\partial \phi_{ext}}{\partial t}. \tag{3.110}$$

The gradients inherited in Equations (3.109) and (3.110) are determined numerically. The gradient of the potential in local z-direction is defined as the source strength of the panel $\frac{\partial \phi}{\partial n} = \sigma$, while the gradient of the free surface elevation $\frac{\partial \zeta}{\partial n}$ is zero. In the local x- and y-directions, a quadratic central differencing scheme is used to determine the gradients. Beforehand, the values ϕ and ζ are linearly interpolated from the neighbouring panel-centres to the panel edges, as these local in-plane directions are defined to be the coordinate directions[7]. A sketch of a free surface grid including information on the determination of the gradient is given in Figure 3.8. Here, the panel actually treated is displayed in dark grey with the centre C_0. The midpoints of the neighbouring panels are C_E (east), C_S (south), C_W (west) and C_N (north). From these panel centres (red), the linearly-interpolated intermediate values on the panel edges (green) together with the value at C_0 are used to determine the gradients $\frac{\partial}{\partial x}$ and $\frac{\partial}{\partial y}$ for the potential and the elevation with a quadratic ansatz. At the borders of the water surface grid,

[6] See Butcher [15] (ch. 3) for a comprehensive explanation.

[7] This is only exact for panels having a perfectly rectangular shape. For distorted panels, the determination of the local in-plane gradients becomes inaccurate (see the definition of the local coordinate directions further above in this chapter).

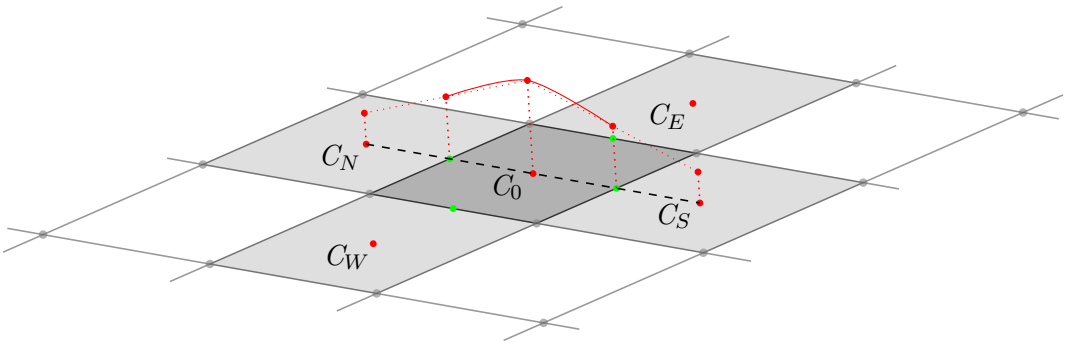

Figure 3.8.: Example for neighbouring relations for a free surface panel. When in-plane gradients are determined on the free water surface, the neighbour values are interpolated from their collocation points (red) to the edges-midpoints (green). The solid red line displays the quadratic ansatz function.

the gradients cannot be computed as explained because not all neighbours are present. In order to prevent numerical errors, a different treatment of the local gradients for the two variables is chosen. When the induced potential is determined, the gradient is built by assuming a linear characteristic between the two remaining panel centres. The gradient of the elevation is determined by assuming that its value does not change outside of the discretised part of the water surface and the value of C_0 is copied to the border panel edge[8].

At some stage of an unsteady simulation, point-to-point oscillations can occur for the variables at the free water surface because of the inherited central differences. Therefore, a numerical damping can be imposed for the elevation ζ using

$$\zeta_0^* = a\zeta_N + (1-2a)\zeta_0 + a\zeta_S, \tag{3.111}$$

using the indices given in Figure 3.8. Here, the superscript * denotes the corrected value. A value of $a \approx 0.1$ already provides a significant amount of damping sufficient for most of the simulations presented within this work. The smoothing is only performed in inflow direction. For simulations with small forward speed, a smoothing in the transverse direction may also become necessary.

At the inflow border of the discretised part of the free water surface, non-smooth gradients of the variables ϕ and ζ can be observed for most cases. This is due to the lack of information for the gradients above discussed, and the disturbance is transported through the whole discretised free surface. In order to prevent this, the calculation of time derivatives $\frac{\partial \zeta}{\partial t}$ and $\frac{\partial \phi_{ind}}{\partial t}$ is damped in the inflow area and the values are set to

[8] See Göttsche [30] (sec. 3.5) for further details.

zero for the first row of panels. Within the inflow area, a smoothing factor is assigned to every free surface panel in a non-linear fashion. At the sideways- and aft-borders of the simulation domain no smoothing is necessary, because disturbances are transported out.

panel split technique

With the implementation of either the free water surface or a wave potential, the necessity of taking emerged parts of a body out of the simulation arises. This is met by the so-called panel split technique. A split factor $f_S \in [0:1]$ is computed against the local elevation, which is determined either from the wave potential or from the deformed free surface and assigned to each body panel. For $f_S = 0$, the panel is emerged, its variable values are set to zero and it is not taken into account for establishing the *SLE* nor for the determination of induced values. Hence, the simulation becomes faster with a large number of emerged panels. For $0 < f_S < 1$, a panel is partly immersed and the value of the split factor refers to the ratio between wetted and total panel area. To reduce its impact, the quantity calculated in the *SLE* is modified. Therefore, the diagonal matrix element is divided by f_S, as proposed by Söding [85].

The split factor is calculated for each panel prior to establishing the *SLE*. Because this can contribute significantly to the simulation time, a fast calculation of f_S is needed and the wetted area is not computed exactly. The simplified equation reads

$$f_S = c_1 \frac{I}{\bar{a}} + c_2, \tag{3.112}$$

with the immersion of the panel centre I, which is determined towards the centre of the nearest free surface panel in gravitation direction or towards the exact free surface height when a wave potential is used. The medium panel edge-length is $\bar{a}$ and c_1 and c_2 are constant values. A medium edge length is introduced to account for elongated panels and it reads

$$\bar{a} = \frac{\sqrt{S}}{\frac{min(a_1;a_2)}{\sqrt{S}}} = \frac{S}{min(a_1;a_2)}. \tag{3.113}$$

This allows for a fast computation of $\bar{a}$, but it introduces a grid dependency to the panel split technique which results in different immersed parts of a body for equal simulations with unequal grid-spacing. For a coarser grid, the immersed part of the body will be smaller, than for a fine grid. This dependency can be managed by the constants c_1 and c_2 in Equation (3.112), where $0 < c_1 < 1$ reduces this grid dependency, while $c_1 > 1$ increases it. The constant c_2 can be used to shift the *virtual* free surface height in order to stabilise a simulation where a body imposes a strong influence on the water surface.

The values of f_S are confined to the range [0:1] and set to zero if < 0 and to one if > 1.

When using the panel split technique, the pressure computation on the panels is slightly different. On emerged panels, the pressure is set to atmospheric pressure. If the split factor is $f_S < 1$, a modified Bernoulli equation is used for the immersed part of the body and Equation (3.77) becomes

$$\Delta p = f_S \cdot \rho \left[-\frac{1}{2} \left(\nabla \Phi \right)^2 + \frac{1}{2} \mathbf{v}_M^2 - gI - \frac{\partial \Phi}{\partial t} \right]. \tag{3.114}$$

The panels located on the emerged part of a body still contribute to the forces acting on it, as atmospheric pressure is imposed.

3.3. Description of the Potential Flow / Viscous Flow Coupling Method

This section reports on the procedure developed in this study for coupling two 3-D flow solvers. A comparable validation in line with an application example is given by Greve et al. [36]. The solvers refer to the *BEM pan*MAREx as described in detail above and the viscous flow *RANSE* solver *FreSCo*$^+$[9]. The aim in developing such a procedure is to combine the advantages of both methods in order to be able to conduct complex simulations in a shorter amount of time compared to *RANSE* simulations but with little loss of accuracy. Determining the exact position of the free water surface is an important constraint because this has a large influence on the computed forces. In order to give an in-depth comparison, complete *RANSE* simulations were also conducted in the *ProSee* project by Wöckner-Kluwe [98]. The main advantage of the coupling method is that the propeller does not have to be geometrically modelled in the *RANSE* solver, so it can be referred to as a propeller model. Using this, the size of the *RANSE* grid can be greatly reduced because neither the geometry nor the boundary layer need to be resolved by the numerical grid. Furthermore, in a complete *RANSE* simulation comprising a pod-housing or a ship and a propeller, a multi-grid technique has to be used. This results in a large computational and setup effort, which can be greatly reduced if the propeller does not need to be physically modelled. Another advantage of the coupling method is that the wake field of a propeller does not need special treatment in a *RANSE* simulation when meeting another geometric boundary like the pod strut and housing, whereas

[9] A description of the *RANSE* method is not given in the context of this work. For general information see Ferziger and Peric [28], for specific information on *FreSCo*$^+$ see Manzke et al. [69], Stück and Rung [88] or Yakubov et al. [99].

the modelling in a *BEM* simulation is quite complex[10]. Furthermore, the different time-scales for the propeller with a large rotation rate compared to a wave with a slow progressive movement due to usual period values are problematic for purely *RANSE* simulations. A second important constraint is that the time step size can be larger in a simulation utilizing the coupling method, so in addition to the faster computation per time step, a lower total number of time steps is needed.

In the following, only the parts of the solver coupling method implemented in the *BEM* are presented. The developments made in the *RANSE* method are described by Wöcker-Kluwe in [98]. For more details on the method and an in-depth validation, see Greve et al. [36].

3.3.1. Physical Considerations

The coupling procedure is based on the exchange of two vector fields, namely the velocity and force distribution between the solvers. In the *BEM*, the velocity distribution in front of the propeller (the wake field) is taken from the *RANSE* domain. This wake field refers to a total wake in the common naval architecture definition[11], due to the fact that it inherits the propeller-induced velocities. These velocities are taken into account in an unsteady *BEM* simulation employing all propeller blades, so they have to be subtracted from the total wake field in order to compute the correct forces based on the effective wake field. Because determining propeller-induced velocities is a crucial aspect in the developed coupling procedure, a detailed validation will be given in Section 4.1.3. The wake field is applied as constant in propeller shaft direction because it is assumed that it represents the velocity distribution at the actual propeller location. In the *BEM* simulation only the propeller is present, so an unsteady simulation using the velocity field from the *RANSE* domain can be easily conducted. In the *RANSE* solver, the forces computed by the *BEM* are used as a volume-force distribution, which is present at the geometrically correct position. By doing this, a 3-D representation of each propeller blade with its pressure and suction side is achieved, and lift as well as displacement effects can be represented. Because of this exact representation, the main flow phenomena induced by the propeller, such as the wake sheet, the leading edge and the tip vortex, can be found in the flow field.

[10] For a detailed investigation of the potential wake field behind hydrofoils and propellers, the work of Lee [66] and He [39] in the research group of Prof. Kinnas at the University of Texas at Austin is recommended.

[11] For an explanation see Carlton [20], sec. 5.5.

3.3.2. Numerical Treatment

Three algorithms controlling the coupling process are implemented. They are depicted in Figure 3.9 and refer to an explicit, an implicit and a semi-implicit scheme. In the explicit scheme, the transfer of velocities and forces between the solvers is conducted once in a time step, whereas in the implicit scheme the transfer can be done multiple times together with new solutions of the individual flow problem. At the beginning of the coupling cycle within both solvers, a converged solution of the sub-problem, referring to a fully developed flow situation, is required. Then, at the start of each time step, the wake field is transferred from the *RANSE* solver to the *BEM* (*Transfer of Velocities*). The wake field is determined in a plane typically located 0.5 to $1.0R$ in front of the propeller position on a pre-defined and structured circular grid. In the *BEM* every panel on the propeller is subjected to an inflow velocity, which is interpolated from this wake field. The velocity is a vector quantity, so the three-dimensionality of the flow regime, especially the tangential velocities, is represented. In the explicit case, the viscous velocities are based on the solution of the last time step. After transferring the total velocity field, in the *BEM*, the propeller-induced velocities are determined and subtracted from the received data. The *BEM* solution is determined and the basic result is one force vector per panel on the propeller blades. This averaged force field is transferred to the *RANSE* solver and distributed on the adjacent cell-centres and their neighbouring cells using a cell-search algorithm described by Brunswig et al. [14], so the effect of body forces is smeared over a certain volume. Although the grids are completely different between the solvers, the algorithm is force conservative. In the explicit scheme, the time step is finished with the solution of the *SLE* in the *RANSE* solver.

In the implicit scheme, several coupling cycles can be conducted in one time step for the *BEM* when embedded in the outer iteration loop of the *RANSE* solver. In every time step, for each outer iteration, a cycle similar to an explicit step is undertaken by using a time-accurate viscous velocity distribution upstream of the propeller. This results in a larger simulation effort. The propeller-induced velocities and hence the effective wake field are also determined by the *BEM* in a time-accurate manner. The time step is finalized when both solvers have converged and the solution advances in time. In the semi-implicit scheme, which is not displayed in Figure 3.9 for clarity reasons, the global cycle is in line with the explicit, but the propeller-induced velocities are iterated until convergence is reached. Therefore, the *BEM* solution is conducted multiple times. The velocity distribution utilised by the *BEM* is thus based on the *RANSE* wake field of the last time step and the actual propeller-induced velocities.

For simulations employing a free water surface, a transfer algorithm from the *RANSE* solver to the *BEM* is developed. It is based on a Fourier series representation of the

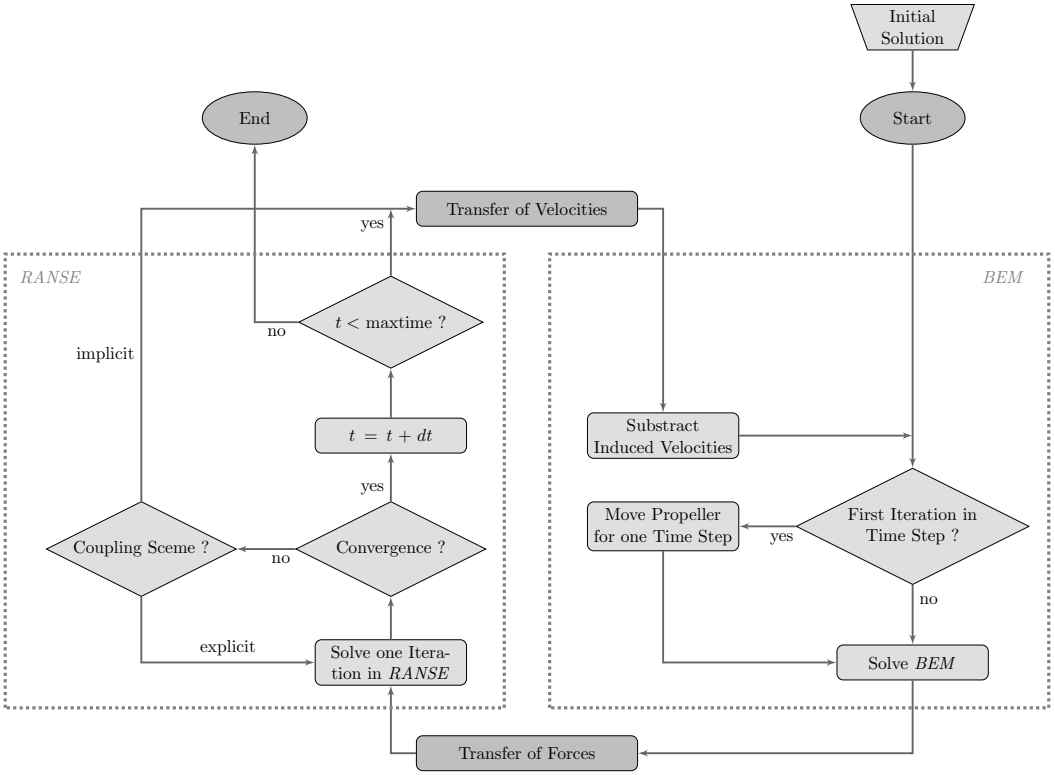

Figure 3.9.: Flowchart describing the implemented coupling algorithms

interface between air and water, which is determined by the *RANSE VoF* model and reconstructed with a constant position in the *BEM*. As for bodies in the case of the free water surface, the grids are completely different in each method, especially with respect to their densities. Furthermore, a transfer from a volume-based to a surface-based formulation is needed. Because only the Fourier coefficients are transferred between the solvers, the algorithm is robust and the surface, or parts of it, can be reconstructed anywhere in the *BEM*. Therefore, the area of the free water surface and the number n of discrete Fourier series are defined. Secondly, the coefficients of the Fourier series are determined by the *RANSE* solver and the free surface height h at a point $P(x, y)$ is computed in the *BEM* by

$$h(P) = \frac{h_0}{2} + \sum_{k=1}^{n} \left[A_k \cdot cos(k \cdot \frac{2\pi}{L} \cdot P_0) + B_k \cdot sin(k \cdot \frac{2\pi}{L} \cdot P_0) \right]. \tag{3.115}$$

Here, $\frac{h_0}{2}$ is the mean value of wave elevation, L is the total length of the Fourier series in longitudinal direction and P_0 is the actual position in the range between zero and L. For each longitudinal strip of panel edges, a single Fourier series is needed. It is reconstructed using n discrete height values $h(P)$ in longitudinal direction and the Fourier coefficients A_k and B_k.

So, the transfer of the free water surface is reduced to transferring the Fourier coefficients for a number of parallel, longitudinal slices of the surface, which is very fast. On the water surface in the *BEM*, only the kinematic b.c. is fulfilled and the surface position is not updated.

4. Validation and Verification

This chapter is devoted to validating and verifying the inherited methods in order to correctly compute the forces acting on propellers subjected to a free water surface and to seaway influences. This is conducted in several steps, whilst the involved physical effects are validated separately. Beforehand, the geometrical properties of the bodies computed in this thesis are given. Three grid studies are discussed in Section 4.1. The first refers to a two-dimensional NACA0012 hydrofoil outlined in Section 4.1.1, for which the convergence of lift and drag forces with grid size and a detailed validation with experimental data are given. Also, the geometrical order of accuracy of the linear *BEM* is displayed. This case can be seen as a pre-study for propeller simulations because the forces on ship propellers are mainly produced by lift effects. Secondly, a grid study on a ship propeller in open water situation is given in Section 4.1.2 in order to display the result quality of the *BEM* simulations. In a third step, a validation of the coupling algorithm is reported, again for the case of a propeller in open water conditions. The first case presented in Section 4.1.3 inherits only one propeller blade because special attention is paid to the propeller-induced velocities. Afterwards, a four-bladed propeller is investigated. The free surface transfer is not validated here, as it is has been published by Wöckner-Kluwe [98] (sec. 4.2.3).

In Section 4.2, the dynamic loads on fully submerged propellers without the interaction with a free water surface are computed. Here, the focus is set on determining free surface- or seaway-influenced loadings. For a propeller in oblique inflow-conditions, a comparison of computed forces and moments to published experimental values is given in Section 4.2.1. This is extended to a propeller in dynamic conditions, which is subjected to wave orbital velocities in Section 4.2.2. Again, a validation with experimental results is given. For a similar situation, the propeller side forces are determined and validated against the results of a different experimental campaign in Section 4.2.3.

The interaction between a submerged body and the free water surface is studied in Section 4.3. Section 4.3.1 investigates a submerged, two-dimensional hydrofoil for which extensive experimental data exists. A validation is given for the lift-induced deformation of the free water surface, which is also a major effect in case of a propeller. Also, three-dimensional simulation results are included in order to investigate the effect of finite span. Secondly, three-dimensional, displacement-driven effects of a submerged spheroid deforming the water surface are displayed in Section 4.3.2 and verified against available

computational and experimental results. This chapter starts with a description of the geometries used for the validation simulations.

hydrofoil geometry

The hydrofoil geometry used in the simulation cases in this thesis refers to a NACA0012. The *NACA four-digit-series* is one of several and surely among those with the most experimental and numerical data available. Along with the development and improvement of airplane wings and helicopter blades, especially in the mid of the 20th century, numerous experimental studies have been undertaken with this airfoil-series. Because numerical methods were first created in the 1950s before an empirical development of wing sections was state of the art for airfoil geometries, very large experimental campaigns were carried out in order to determine the aerodynamic characteristics of wing sections. Many improvements were made and several airfoil sections were developed, mostly driven by military research undertaken in the context of the Cold War armament. In this work, the geometrical description and dimensionless pressure data published by Abbott and von Doenhoff [1] and results given by Gregory and O'Reilly [34] and Duncan [25] will be used. The NACA0012 is non-cambered with a maximum breadth of 12% of the chord length c at 30% of the profile length measured from the leading edge.

Propeller A geometry

The first propeller used in the simulations within this thesis is a *Rolls-Royce* design called P1440, which is used on an *Azipull* azimuthing thruster. It is a controllable pitch propeller with four blades and a diameter of $3.2m$. The pitch is kept constant at the design pitch ratio of $P/D = 1.2$ for all the simulations conducted in the following. The main data of the propeller is presented in Table 4.1 and a three-dimensional view is given in Figure 4.1a. A hub is only considered in the open water cases. The experimental data used for the validation and application cases has been provided by numerous campaigns conducted at the model test basin *MARINTEK*. Results are published by Koushan et al. [60], Kozlowska et al. [62] and can also be found in the doctoral thesis of Wöckner-Kluwe [98].

Propeller B geometry

The second propeller investigated is the fixed pitch propeller P1374 operating at a thruster unit. It has four blades and a larger expanded area ratio and less pitch than Propeller A. Only the model propeller data is given in Table 4.2 because all available data used for validating the numerical results of Propeller B inherit model test data. A three-dimensional view of the propeller is given in Figure 4.1b. This propeller geometry is taken into account because several experimental campaigns have been performed with it at *MARINTEK*, where the quasi-steady behaviour in oblique inflow and the dynamic behaviour in deeply- submerged and ventilating conditions were investigated. Results

Data	Unit	Value
Diameter (D)	$[m]$	3.2
Hub diameter (D_h)	$[m]$	0.86
Number of blades (z_p)	$[-]$	4
Design pitch ratio at $r/R = 0.7$ (P/D)	$[-]$	1.2
Expanded area ratio (EAR)	$[-]$	0.447
Scale factor (λ)	$[-]$	0.0625
Model scale rotation rate (n)	$[1/s]$	18

Table 4.1.: Main data of propeller P1440 (Propeller A)

Data	Unit	Value
Diameter (D)	$[m]$	0.25
Hub diameter (D_h)	$[m]$	0.06
Number of blades (z_p)	$[-]$	4
Design pitch ratio at $r/R = 0.7$ (P/D)	$[-]$	1.1
Expanded area ratio (EAR)	$[-]$	0.6
Skew angle (θ)	$[°]$	25
Model scale rotation rate (n)	$[1/s]$	11.79

Table 4.2.: Main data of propeller P1374 (Propeller B) in model scale

are published by Koushan [58], Amini [3], Califano and Steen [17] and Califano [16]. The thruster is investigated both in pushing and pulling mode, whereas in this thesis comparisons with the results of the latter are undertaken because the thruster body is not present in the simulations.

thruster coordinate system conventions

Results will be presented in the following for Propeller A and B operating at a thruster unit. The coordinate system conventions are depicted in Figure 4.2. Two different coordinate systems, the propeller coord. sys. (x, y, z) and the thruster coord. sys. (x', y', z') are used. The simulations are conducted at negative azimuth angles around the z'-axis, denoting a range of positive angles of the inflow velocity vector towards the propeller. The forces and moments are presented in the propeller coordinate system.

spheroid geometry

For validating the forces acting on submerged bodies, a prolate spheroid is considered. Using this basic, rotational symmetric body, various experimental studies (see Chey [23] or Farell and Güven [27]) and numerical simulations (see Farell [26] or Uslu and

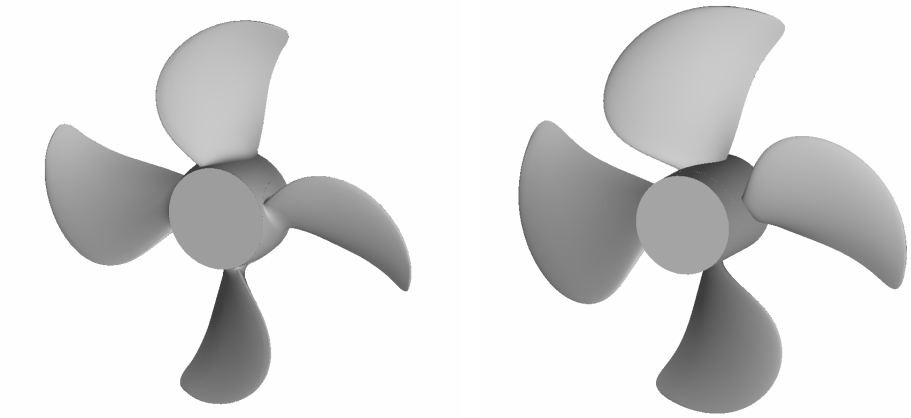

(a) Propeller A (b) Propeller B

Figure 4.1.: Three dimensional view on propellers A and B

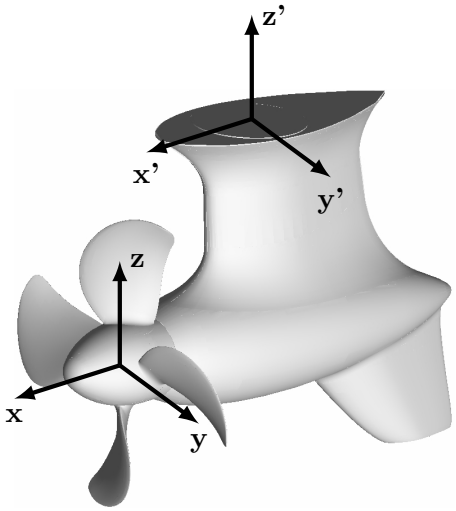

Figure 4.2.: Definition of coordinate systems at the thruster

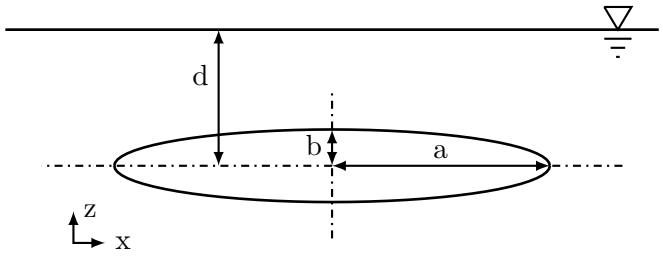

Figure 4.3.: Definition of coordinate system and labelling of the spheroid case

Bal [95]) were conducted in the past. In this work, comparisons are made with the simulations presented by Uslu and Bal [95] and the experimental results obtained by Chey [23]. The case is set up as depicted in Figure 4.3 according to the notation used by Farell [26]. The radii of the body are a and b, its immersion, measured from the axis of symmetry to the undisturbed free surface height, is d and the length $2a$ is $12m$ in all simulated cases. The wave resistance coefficient c_w is formulated according to Chey, who uses the notation inheriting the stagnation pressure, as other forms based on length parameters are used in other publications. Several length to diameter (a/b) ratios are investigated at different Froude numbers. The immersion of the spheroid, interpreted as d/a-ratio, is also varied.

4.1. Validation of the Numerical Procedures

4.1.1. Grid Study on a 2-D Hydrofoil

A grid study on a NACA0012 hydrofoil is conducted in order to test the method's geometrical order of accuracy. Because there are several dependencies, the geometry is treated as two-dimensional in order to reduce the complexity of the problem. The results for the different grids are evaluated using the error measure ϵ, which relates the computed value α to an extrapolated *exact* value α_0. For example, the lift coefficient $c_{l,0}$ is determined using the error estimates of the solution obtained with the finest grid with $2m$ panels and the second finest grid with m panels. Assuming a linear convergence behaviour (because of the linear geometric approximation), the following formula is used to identify α_0:

$$2 \cdot \frac{\alpha_{2m} - \alpha_0}{\alpha_0} = \frac{\alpha_m - \alpha_0}{\alpha_0}, \tag{4.1}$$

$$\Leftrightarrow \alpha_0 = 2\alpha_{2m} - \alpha_m. \tag{4.2}$$

For the grid study, the number of panels on the hydrofoil is varied in conjunction with the number of panels in the trailing wake. Hence, a smooth transition of the panel size on the body into the wake is achieved. The wake length is constant in this case, the angle of attack is six and ten degrees and the number of body panels is altered between six and 1536 with a factor of two between the adjacent grids. The numerical grid on the hydrofoil is strongly refined towards the leading edge in order to resolve the steep pressure gradients in this area. Also, a refinement towards the trailing edge is made. The number of wake panels is determined to result in a constant wake length and the number of iterations has to be large enough for the wake shape and thus the forces on the blade to converge. The more panels are present in the wake, the more iterations have to be conducted because the iteration process itself converges in line with the position of the wake panels. The results of the grid study on the hydrofoil are depicted in Figure 4.4 and they show a nearly linear convergence behaviour, so the error is halved between two consecutive grids. The lift forces in Figure 4.4a show an identical behaviour for six and ten degrees of attack-angle when the number of panels is altered, whereas the drag forces in Figure 4.4b show a larger error for the smaller angle. The lift forces show a more favourable behaviour, having smaller errors than the drag forces at the coarser grids. Although the results for the grid with 96 panels on the hydrofoil (fifth grid in Figure 4.4) are not converged to the value of the finest grid, it is chosen for further investigations because the other effects will contribute to a better result. In order to provide as much information as possible, the non-dimensional lift and drag values for the different grids are given in Appendix B.1, Figure B.1.

In a second stage, the length of the trailing wake is varied, which is a factor point for the accuracy of panel methods[1]. Because the circulation of the wake induces effects on the hydrofoil itself, the wake length influence on the lift and drag forces of the foil is strong and must be chosen carefully to meet the requirements of the simulation case.

The results of the study on the wake length are displayed in Figure 4.5 for a length from approx. 0.3 to 80 times the chord length of the hydrofoil, while 16 wake panels represent one chord length. Again, the convergence rate shows a nearly linear behaviour. Like in the hydrofoil grid study, the error using a small wake length is larger on the drag forces, as shown in Figure 4.5b, and the absolute error of the lift forces shown in Figure 4.5a is smaller. Because the influence of each wake panel on the foil has a quadratic relation to their distance, the convergence rate is more than linear in this case. The wake with 160 panels (sixth grid in Figure 4.5) and a length of ten times the chord length is chosen for further investigations. Again, the non-dimensional force values are also presented in Figure B.2.

[1] For further information on the modelling of the wake sheet behind hydrofoils and marine propellers, the contribution given by Greco et al. [32] is recommended.

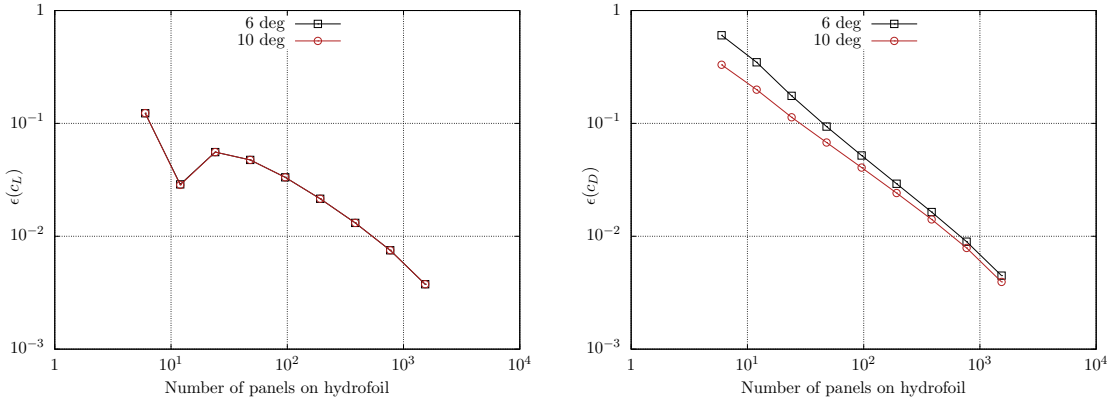

(a) Error of lift forces (b) Error of drag forces

Figure 4.4.: Error of forces acting on the NACA0012-hydrofoil for different grid resolutions (wake panel length $\hat{=} 1/16c$, 80 wake panels, converged result)

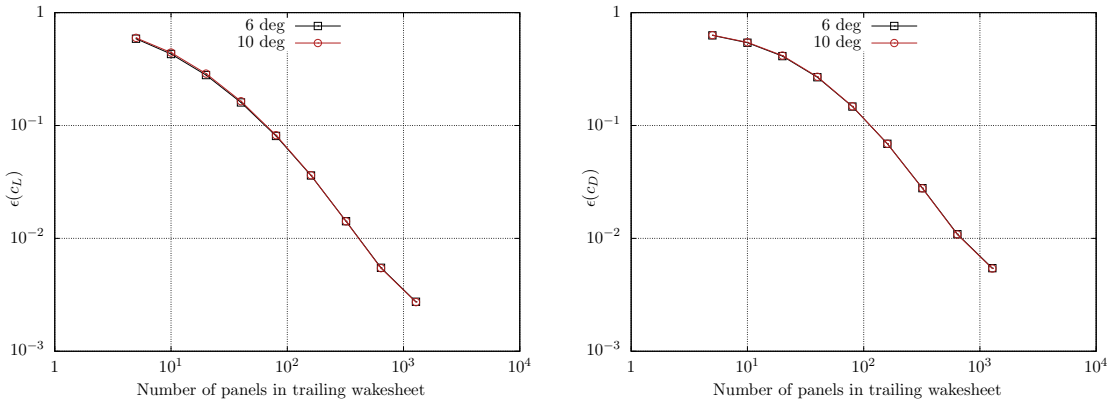

(a) Error of lift forces (b) Error of drag forces

Figure 4.5.: Error of forces acting on the NACA0012-hydrofoil for different lengths of the trailing wake-sheet (96 panels on hydrofoil, wake panel length $\hat{=} 1/16c$, converged result)

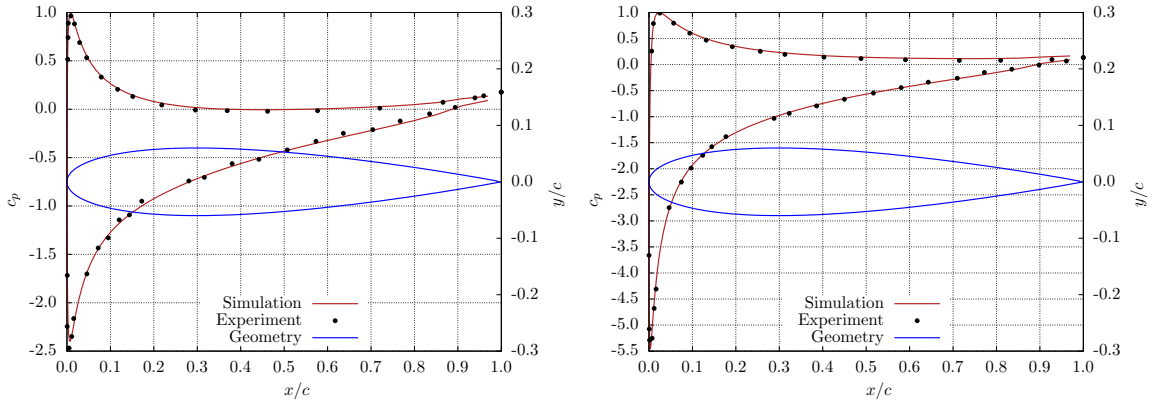

(a) 6° angle of attack (b) 10° angle of attack

Figure 4.6.: Geometry of the 2-D NACA0012 hydrofoil and comparison of the pressure distribution to experimental results given by Gregory and O'Reilly [34] (96 panels on hydrofoil, wake panel length $\hat{=} 1/16c$, 160 wake panels, converged result)

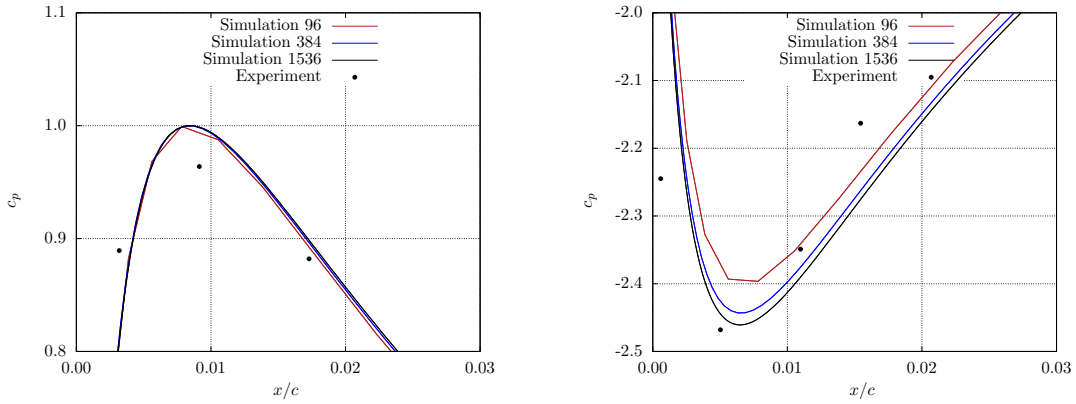

(a) pressure side (b) suction side

Figure 4.7.: Discretisation influence on the pressure peaks for 6° angle of attack (wake panel length $\hat{=} 1/16c$, 160 wake panels, converged result)

The final results of the study are presented in Figure 4.6, showing the pressure distribution at an angle of attack of six degrees (4.6a) and ten degrees (4.6b). The results given by the red lines are obtained with the grid described above with 96 panels on the hydrofoil and 160 in the trailing wake, referring to a wake length of ten chord lengths. The blue lines show the hydrofoil geometry; the experimental data obtained by Duncan [25] is represented by black dots. The pressure distribution and the peaks at the stagnation point on the pressure side and in the low-pressure area on the suction side are well predicted for both investigated angles. The line indicating the computed results ends slightly before the trailing edge because the c_p-values are computed for the collocation points in the centre of each panel. An important indication for a good result quality is the stagnation point shift towards the trailing edge at higher angles of attack, which can be seen in Figure 4.6.

In Figure 4.7 a closer investigation of the pressure-peak areas for different discretisations of the hydrofoil is given. The curves converge to a single characteristic for the fine grids in both figures, whereas the stagnation pressure and the curve progression are already perfectly reproduced by the coarse grid with 96 panels on the body. In the low-pressure area a clear dependency of the minimum value on the grid size can be observed and the curve meets the experimental value for the very fine grid and shows only minor deviations for the coarser.

4.1.2. Propeller Open Water Performance

In order to show the capability of the *BEM* to compute forces on propellers, a grid study on a propeller in open water conditions is given in the following. The propeller refers to the *MARINTEK*-design Propeller A. For each of the following simulations, the results are iterated until convergence. The different grids are made in such a manner, that the panels on the blade have a good panel quality as described in Section 3.2.4. Seven grids having between 8 and 32 panels in radial direction and between 12 and 48 in tangential direction per blade are used. This results in grids having between 96 and 1536 panels per blade. One exemplary propeller blade grid with 28x42 panels is displayed in Figure 4.8a. In the picture, the hub is not displayed in order to give a larger image of the blade panels, but it is included in the calculations. When simulations are conducted on even finer grids, numerical errors can occur due to a declining panel quality when more geometrical details are represented by the panel grid. On the other hand, the simulation time rises approximately in a quadratic manner compared to the panel number. The grid study is conducted at an advance ratio of $J = 0.9$.

The K_T and K_Q-values for the blade grid study are presented in Figure 4.8b, non-dimensionalised by the value of the finest grid. The convergence of the thrust and torque coefficients with the number of panels is satisfactory. A noticeable effect is that

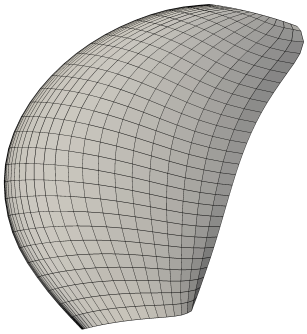

(a) Blade grid with 28x42 panels

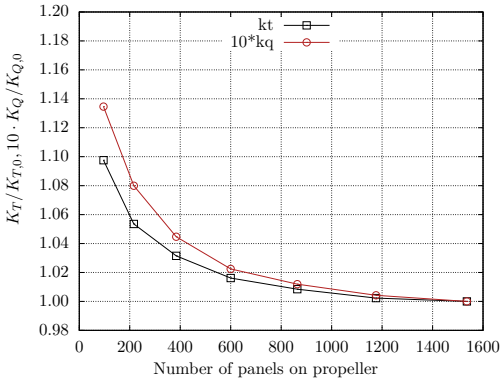

(b) Convergence with blade grid size

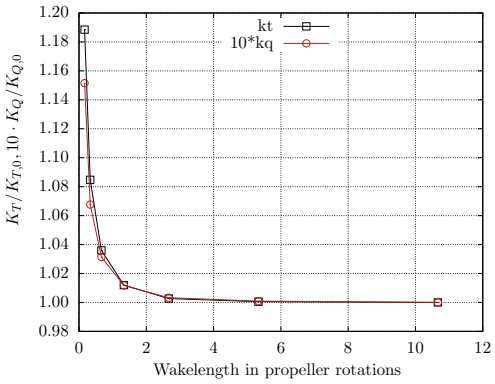

(c) Convergence with wake length

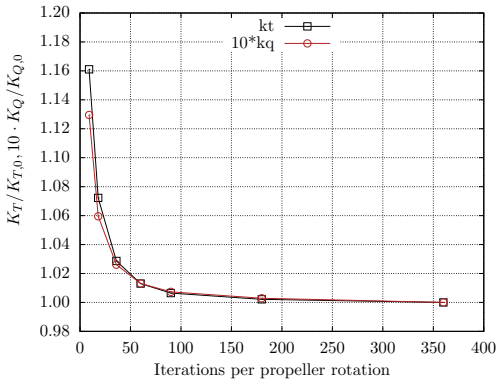

(d) Convergence with iteration step size

Figure 4.8.: Example for numerical grid and grid study on convergence of K_T and K_Q-values ($J = 0.9$)

the rate of convergence can be, by some extent, triggered by a directional refinement on the blade. With a more pronounced refinement towards the blade's leading edge, a faster convergence rate results. This has an upper limit when the panel geometry distorts in the area near the tip or the panel edge length-ratio becomes too large at the leading edge. The second finest grid with 1176 panels ($28x42$) is chosen for further investigations because the difference to the finest grid is below 0.5%.

When the grid sensitivity is investigated in a *BEM*, the grid of the trailing wake sheet must also be taken into account. The length of the trailing wake has a strong influence on the results because the wake sheet leaving the trailing edge induces velocities on the blade. This effect is investigated in Section 4.1.1. In return, the pressure and hence

Parameter	Value
Blade grid size	28 x 42 panels
Iteration step size	6° of one propeller rotation
Length of trailing wake	480° of one propeller rotation

Table 4.3.: Simulation parameters obtained from Propeller A grid study

the forces computed on the blade are too large when the length of the trailing wake sheet is insufficiently short. The computed thrust and torque values reduce, the longer this sheet is modelled. An influence of the trailing vorticity can even be found when the wake sheet is modelled for ten propeller rotations behind the blade, which is in line with the information published by Greco et al. [32]. In the actual study, the range of $\frac{1}{12}$ to $10\frac{2}{3}$ propeller spirals for a freely deforming wake sheet is considered. The results displayed in Figure 4.8c show a good convergence behaviour, and the difference in the computed coefficients are below one per cent for the three longest wake representations. For further studies, the wake length referring to 480° of a propeller rotation is chosen because the error compared to the longest wake is about 1%.

The iteration step size chosen in a steady simulation determines the length of each wake panel because it refers to the steady motion of the propeller within this time interval. Large iteration steps usually result in a poor convergence behaviour because the wake roll-up can only be smooth with a sufficient number of supporting points in the circumferential direction. The refinement in radial direction is already determined by the blade grid. On the other hand, with a finer representation of the wake sheet, the simulation time increases drastically. A study on the forces computed with different iteration step sizes is given in Figure 4.8d. A large effect of the iteration step size on the computed thrust and torque values can be seen. The iteration step size referring to 60 iterations per rotation or 6° per iteration step is chosen for further investigations because the results show an approx. 1%-difference to the results computed with the smallest iteration step size. An overview on the results obtained from the grid study for Propeller A is given in Table 4.3. These values can also be chosen for other propellers, although care has to be taken to obtain a proper resolution of the leading edge and the blade tip geometry. Usually, a good indication of a suitable grid for the *BEM* is a fast convergence of the results and a smooth rollup of the wake panels in the tip region.

In Figure 4.9, the open water data for Propeller A and B with a geometrically modelled hub is depicted showing a reasonable agreement with the experimental values. This can only be applied when the propeller has a relatively low loading near the design point. Then, the flow situation is mostly potential-driven and can be properly computed with a *BEM*. When the loading of the propeller is high, the hydrodynamic angle of attack

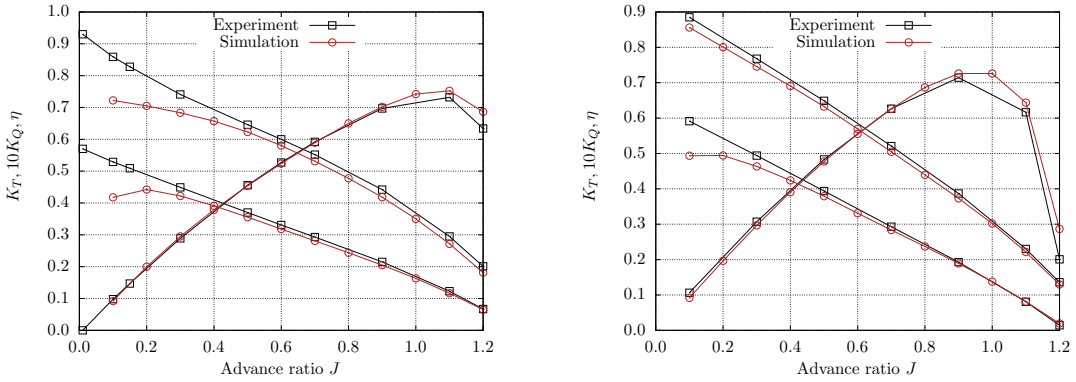

(a) Propeller A (b) Propeller B

Figure 4.9.: Propeller open water diagrams

of the profile sections is and viscous effects also become more pronounced. Therefore, the thrust and torque values computed by purely potential-based simulations become too small compared to experimental results at low advance ratios[2]. To overcome this, a fixed-wake approach with prescribed pitch of the trailing wake sheet is used as a function of J. The resulting open water diagrams are in satisfying agreement with the experimental values, showing slightly underpredicted values for both the thrust and torque coefficient. The ratio between thrust and torque is well predicted and the propeller efficiency shows a good agreement compared to the measured values.

4.1.3. Validation of the Coupling Procedure

A validation of the coupling procedure is given in the following for the model-scale propeller, starting with grid studies in both solvers described in Section 3.3. Because the computational grids are not the only parameters determining the solution, a study on the induced velocities computed by the involved methods is given next. Therefore, one blade of Propeller A is simulated in open water conditions without considering the hub. This case aims to exactly determine the propeller-induced velocities and to compare them with the results of the involved solvers, which is a crucial point in the verification process of the coupling procedure. The induced velocities are determined inside the *BEM* and subtracted from the *RANSE* velocity-field, in order to acquire the effective wake field as described in Section 3.3.1. This assumption is only reasonable when the induced velocities computed by the two solvers are identical. If only one blade

[2] For a discussion on viscosity-driven effects occurring on propellers, which cannot be determined by a *BEM*, see e.g. Greeley and Kerwin [33] or Caponetto and Rolla [18], [19].

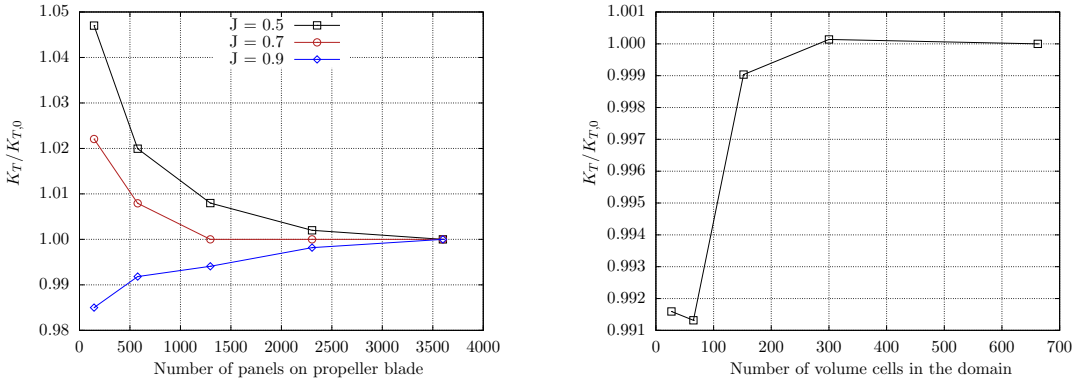

(a) *BEM* results (b) *RANSE* results

Figure 4.10.: Grid study for Propeller A

of a propeller is present in the simulation domain, no interaction effects are inherited in the velocity field and the induced velocity of the single blade is equal to the total perturbation velocity.

The domain used in the *BEM* is unbounded, following the assumptions resulting in Equation (3.20) and only the blade is present. It is represented in the *RANSE* grid by a body-force distribution as discussed above. The *BEM* grid consists of n x m panels per blade with n being the number of panels in the blades radial direction and m in the blade sections circumferential direction. Five different grids with $n \in [8, 16, 24, 32, 40]$ and $m \in [18, 36, 54, 72, 90]$ are used in the simulations conducted with the solver coupling method together with a $300k$ *RANSE* grid in order to investigate grid dependency of the numerical procedure. The error related to the thrust found in the finest-grid solution is shown in Figure 4.10a. A dependency of the solution on the advance ratio of the propeller can be observed, showing a faster convergence with grid size for the propeller operating at low load near the design point. The overall convergence towards the finest-grid solution is satisfactory. The *BEM* grid with 16 x 36 panels is chosen for further investigation, showing a deviation to the finest grid of above 1% for the highest loading at $J = 0.5$, because the main motivation for the solver coupling method is a reduction of computational time. Therefore, a minor loss in the result quality is accepted.

The second step in the validation procedure of the coupling algorithm is a *RANSE* grid study, which is conducted at $J = 0.5$ and presented in Figure 4.10b. The *RANSE* grid is an empty cuboid because the geometry is completely inherited in the *BEM*-simulation domain for this case. In the unstructured, hexahedral volumetric grid, the propeller and its slip-stream are refined and the grids generated contain $27k$, $65k$, $152k$, $300k$

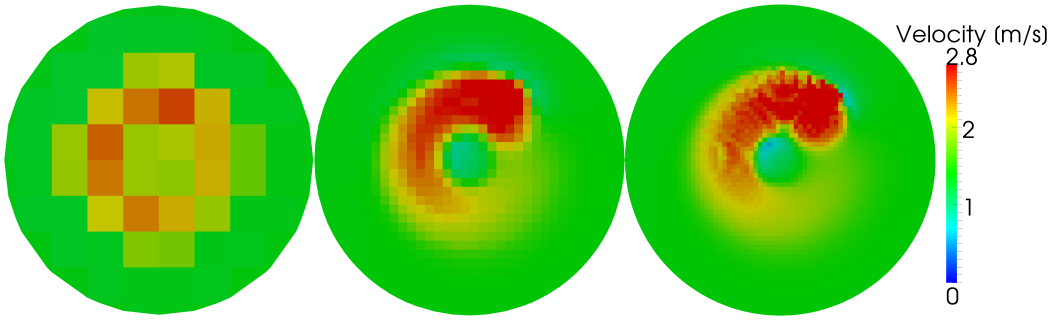

Figure 4.11.: Velocity distribution in the propeller plane for one blade position during a simulation using the coupling algorithm. Comparison between the different *RANSE* grids, with $27k$ (left), $152k$ (middle) and $300k$ cells (right).

and $662k$ cells, respectively. Also, the area in front of the propeller where the velocity field is transferred to the *BEM* lies within the refined volume. The time step of the simulation refers to 3.78° of one propeller rotation. Due to the different discretisation of the flow volume, the propeller forces are distributed on a different number of grid cells. Because the inherited cell-search algorithm (see Brunswig et al. [14] for a description) used to distribute the forces is force-conservative, only a 1%-difference in the computed thrust and torque values can be observed between the coarse grids with $27k$ and $65k$ cells and the finest grid. Already with the very coarse grids, the main features of the coupling algorithm, namely the exchange of a velocity and a force distribution, act in a satisfactory manner and the deviation to the solution obtained with the finest grid is below 10%. The results acquired with the finer grids having between $152k$ and $662k$ cells are within a 1%-range. Thus, the main difference is found for the representation of the local propulsion effects, such as the blades tip vortex, within the *RANSE* domain. In the following the spatial distribution of forces in the *RANSE* domain will be investigated using the velocity distribution in the propeller plane for the different *RANSE* grids depicted in Figure 4.11. The coarsest grid has an edge-length of the volumetric cells of only about 1/5th of the propeller diameter D and an idea of the blade position can only be obtained from the velocity distribution. The medium fine grid already shows the propeller slip stream and a reasonable resolution of the blade, having an edge-length of $D/20$. The fine grid uses a $D/40$ edge-length and the result shows a clear representation of the blade position and a good reproduction of its leading edge geometry. Also, a slow-velocity region at the blade tip can be observed (blue colour), denoting tip vortex effects.

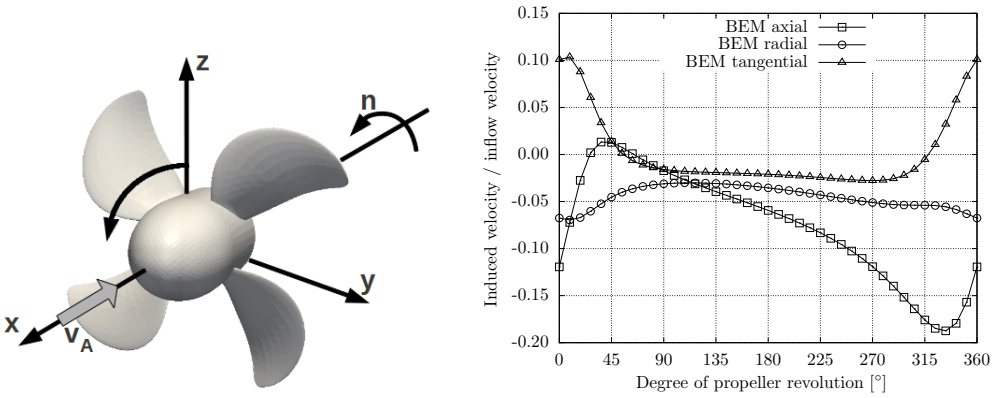

(a) Definition of coordinate system

(b) Induced velocities in the *BEM* ($J = 0.5$, $r = 0.7R, \varphi = 0°, dx = 0.5R, dt \hat{=} 3.78°$)

Figure 4.12.: Single-blade open water case

With grid studies conducted in both involved solvers, a verification study on the induced velocities is given in the following using the 16 x 36 panels *BEM* grid and the $300k$ cells *RANSE* grid. The coordinate system used here is depicted in Figure 4.12a together with an impression of the propeller position inheriting the full propeller. The induced velocities in the axial, radial and tangential direction for the single-bladed case are shown in Figure 4.12b for the single blade located in the topmost position referring to an angle $\varphi = 0°$. For this time-instant, the velocities differing from the inflow velocity are displayed for all positions having the same radius $r = 0.7R$. The trailing edge is situated at $\varphi \approx 340°$ and the leading edge at $\varphi \approx 20°$ and the propeller rotation direction is positive around the x-axis (from left to right in Figure 4.12b). The induced velocities are plotted for the propeller operating at an advance ratio of $J = 0.5$ and a time step referring to 3.78° of one propeller rotation. In Figure 4.12b, a steep increase of the absolute value of axial induced velocities can be observed in the blade area from the leading to the trailing edge having the maximum absolute value near the trailing edge position and showing a smooth decrease behind the blade. A negative value accounts for a suction effect of the blade and only very small positive values occur directly at the leading edge. The absolute value of radial-induced velocities is lower compared to the other directions, with an increase in front of the blade and in the leading edge area, showing only negative values, which lead to a contraction of the propeller slip stream. The tangential-induced velocities are positive in the blade area, accounting for an induction in rotational direction between $\varphi \approx 315°$ and $\varphi \approx 50°$ and showing small negative values for the other angular positions.

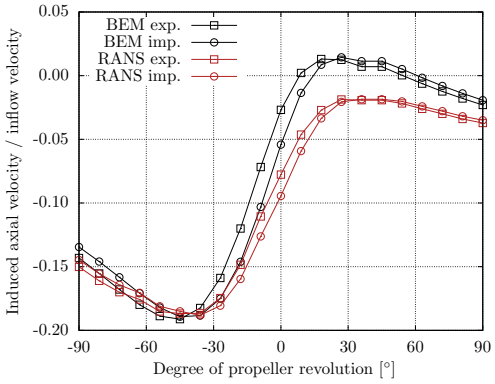

(a) Explicit and implicit scheme
$(J = 0.5, r = 0.7R, dx = 0.5R, dt \;\hat{=}\; 3.78°)$

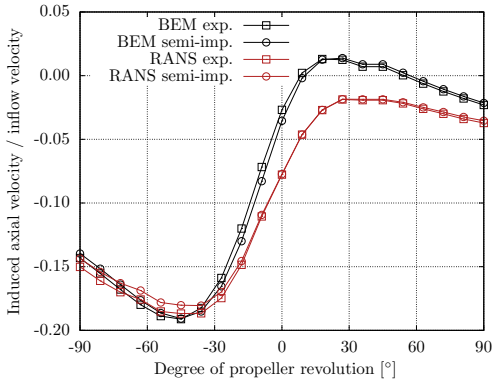

(b) Explicit and semi-implicit scheme
$(J = 0.5, r = 0.7R, dx = 0.5R, dt \;\hat{=}\; 3.78°)$

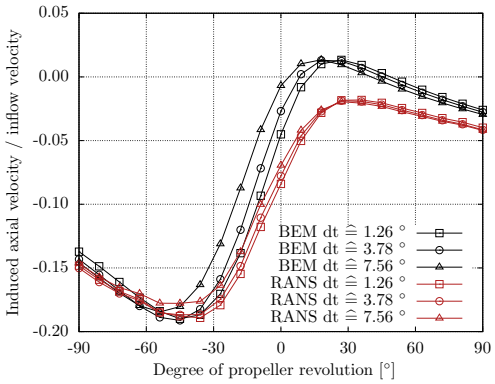

(c) Explicit scheme, variation of time step
$(J = 0.5, r = 0.7R, dx = 0.5R)$

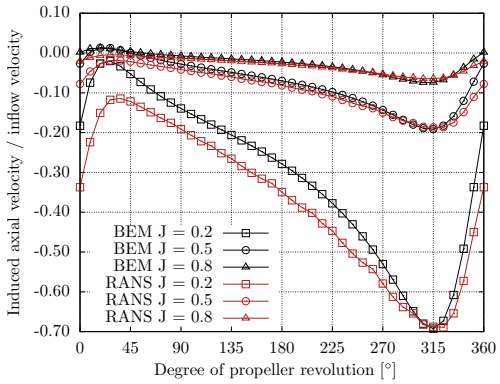

(d) Explicit scheme, variation of advance ratio
$(r = 0.7R, dx = 0.5R, dt \;\hat{=}\; 3.78°)$

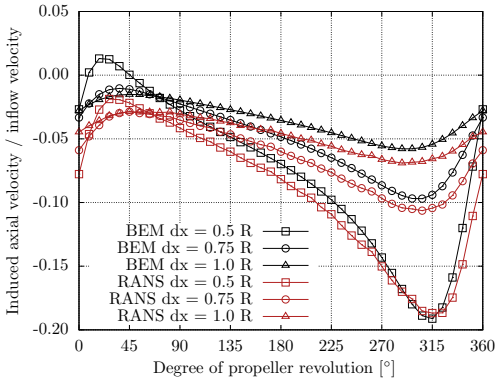

(e) Explicit scheme, variation of plane distance
$(J = 0.5, r = 0.7R, dt \;\hat{=}\; 3.78°)$

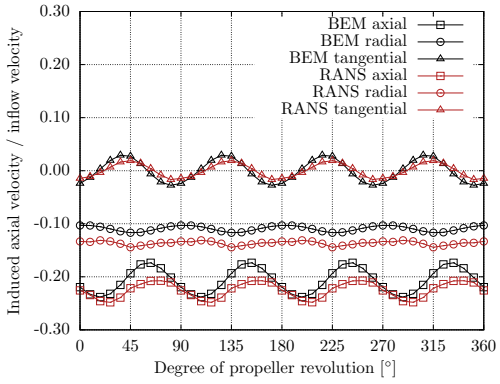

(f) Explicit scheme, four-bladed propeller
$(J = 0.5, r = 0.7R, dx = 0.5R, dt \;\hat{=}\; 3.78°)$

Figure 4.13.: Comparison of induced velocities between the *BEM* and the *RANSE* results in a simulation using the solver coupling method. The blade position is $\varphi = 0°$.

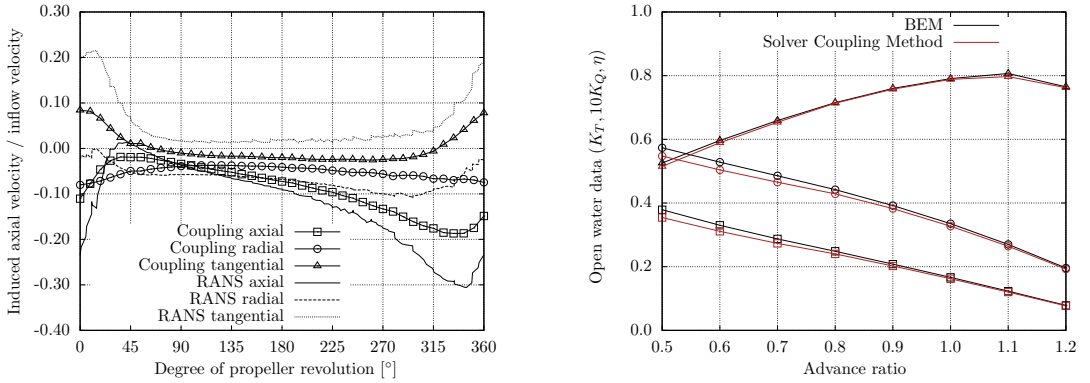

(a) Comparison of computed induced velocities by the coupling algorithm and a *RANSE* simulation ($J = 0.5, r = 0.7R, dx = 0.5R, dt \hat{=} 3.78°$)

(b) Comparison of open water data computed by the coupling algorithm and *BEM* ($n = 18\frac{1}{s}$)

Figure 4.14.: Final results of the validation study conducted with the solver coupling method

In Figure 4.13, an in-depth comparison between the induced velocities in the *BEM* and the *RANSE* solver within a coupled simulation is given. Therefore, in every investigation, one of the determining parameters is varied, while the others are kept constant. In the upper Plots 4.13a and 4.13b, the axial induced velocities computed using the explicit coupling algorithm are compared to the implicit and the semi-implicit. For the sake of a clearer image, the induced velocities are only plotted for the upper half of angular positions. The minimum value of the axial-induced velocities accounting for a strong suction effect at $\varphi \approx -45°$ is met by all plotted curves except for the *RANSE* values in the semi-implicit case. In the implicit case, the decrease in induced velocities and also the increase after the minimum is more steep than in the other cases. This observation could result from the small time lag between the two solvers in the explicit algorithm. In general, the maximum values in front of the blade at $\varphi \approx 20°$ are considerably higher for the *BEM* induced velocities, accounting for a less significant suction effect. This is due to a more rapid increase in suction over the length of the blade section and could result both from a better leading-edge resolution in the *BEM* and numerical damping in *RANSE*.

When looking at the induced axial velocities for the explicit case using different time step sizes in Figure 4.13c, the minimum and maximum values computed with both solvers are not affected by the variation. For smaller time steps, the steepness of the curves along the blade contour increases and the results achieved in the *BEM* and the *RANSE* solver become more similar, which is obvious near the trailing edge of the blade profile between $\varphi \approx -60°$ and $\varphi \approx -30°$. In Figure 4.13d, the results are compared

Parameter	Value
BEM grid	16 x 36 panel grid
RANSE grid	$300k$ cells grid
Coupling sceme	explicit
timestep size	$dt \hat{=} 3.78°$
plane distance	$dx = 0.5R$

Table 4.4.: Simulation parameters obtained from validation study

for different propeller loadings. As expected, the absolute value of the induced velocity is much higher for high loadings, while the relative deviation between the curves of the *BEM* and the *RANSE* solver is comparable between the three J-values computed. The absolute deviation is higher for the low J-value case. Finally, in Figure 4.13e, the distance between the plane in which the velocity distribution is exchanged and the propeller origin is varied. Because the *RANSE* solver supplies significant numerical damping, the induced velocities decay for larger distances to the blade location. In the *BEM*, this effect shows an approximate quadratic relation due to the formulas given in Section 3.2.4. The curves show larger relative deviations for larger distances dx to the propeller origin. When the plane is too close, it may collide with the blade geometry leading to an overstated induction and causing unphysical effects. Therefore, the choice of the right distance is crucial for the result quality, but it is difficult to choose and may be chosen differently for each flow situation.

With the results obtained from the single-blade simulation cases discussed above, an optimum setup for this flow situation is found. This is mainly based on a valid representation of the induced velocities in the involved baseline methods and it is arranged in Table 4.4. With this setup, a simulation with a full, four-bladed propeller is conducted and the results for the total induced velocities are shown in Figure 4.13f. The axial-induced velocities show a suction effect, the radial-induced velocities a stream contraction and no averaged-induced rotational effect can be found upstream of the propeller. This effect is only visible downstream, which is in line with the common scientific state of knowledge[3]. The average absolute value of axial-induced velocity is larger in the *RANSE* domain, which is in line with the results of the single-blade case. The evaluation of the simulations shows that the induced velocities are in reasonable agreement and the propeller faces similar operation conditions in both involved solvers.

[3] It can be compared to the common propeller theories (see e.g. Carlton [20], ch. 8), wherein the propeller develops vortex-systems in its slipstream, but not before it. This is confirmed by all *BEM* and *RANSE* simulations conducted by the author.

Finally, in Figure 4.14a, a comparison between the velocities obtained in the *RANSE*-part of a coupled simulation and those of a purely *RANSE* simulation with geometrically modelled propeller is given. The grid in the *RANSE* simulation is much finer in order to represent the propeller geometry, resulting in about ten times the number of cells compared to the grid used in the coupling case. An encouraging agreement can be observed as the curves show similar characteristics with higher maximum absolute values in the case of the *RANSE* computation. This is as expected because the geometrical details cannot be fully captured by the solver coupling method, but they are important when the total local influence of the propeller, provided by the induced velocities, shall be considered. In Figure 4.14b, the open water results computed by the *BEM* and the explicit coupling algorithm are shown. A comparison is made to the *BEM* results, because a reproduction of those by the results obtained with the coupling method accounts for the numerical accuracy of this algorithm. The difference between the computed values is acceptable showing larger absolute deviations for higher propeller loadings.

4.2. Dynamic Loads acting on Propellers

4.2.1. Propeller Loads in Oblique Inflow Conditions

This section reports on the forces and moments acting on Propeller B in oblique inflow computed with the free wake alignment model described above. The free deformation towards the local velocity direction is important in order to correctly determine the effects due to radial and tangential velocity components of a ship wake field and of wave orbital velocities on the shaft loads. In the first step, unsteady simulations are conducted and the performance of the propeller in open water condition subjected to an inclined inflow is evaluated. A hub is not included in the model scale simulations; the blade grid consists of 16 x 24 panels in order to reduce the simulation costs, the time step refers to 6° and the length of the trailing wake surfaces to 480° of a propeller rotation.

The forces and moments acting on the propeller are determined by averaging the values of the thrust and torque coefficients for six propeller rotations after the forces show a periodic behaviour. The results for different propeller loadings and oblique inflow angles are presented in Figure 4.15. Only positive angles of oblique inflow, denoting negative heading angles around the z'-axis (see Figure 4.2) of the thruster, are taken into account in the simulations. An angle range between straight inflow and 30° is presented for the symmetric case. The coefficients are non-dimensionalised by the value obtained at straight inflow conditions and compared to experimental results given by Amini et al. [4], who also show results of different computational methods, namely a Blade Element

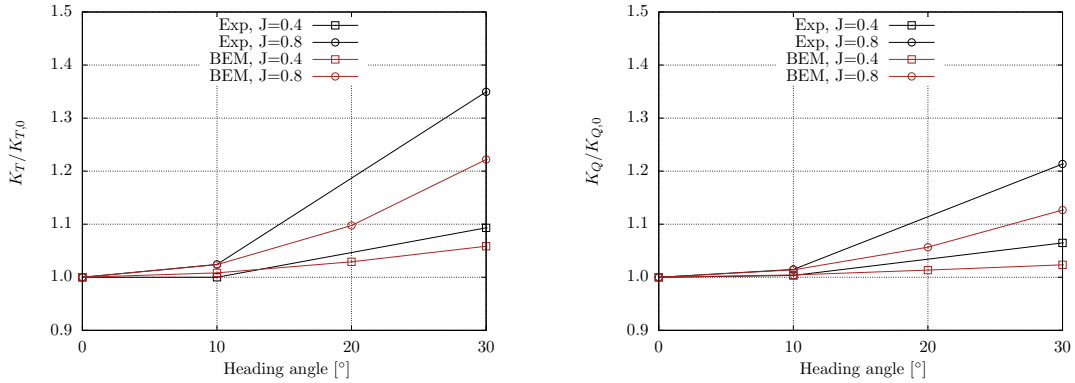

(a) Thrust coefficient

(b) Torque coefficient

Figure 4.15.: Influence of oblique inflow angle on average propeller loading of Propeller B

Momentum Theory[4] (BEMT), a *BEM* and a *RANSE* solver. The results depicted in Figure 4.15 show the same tendency as the *BEM* results presented by Amini et al., which are not depicted here. A clear dependency of the load increase with inclination angle is visible, having a higher percental increase at lower propeller loading. The results obtained with the *BEM* show an underprediction of the load increase when compared to the experimental results. One reason therefore is that the *BEM* forces are in general too small at high loadings when the free wake alignment model is used. A second cause might be the setup, which is not completely equal for the compared cases because the thruster strut has been part of the experimental setup and is neglected in the simulations. The trend is captured well.

The computed values for the averaged single blade loadings are presented in Table 4.5, where the more pronounced increase in thrust and torque values for the higher advance ratio is quantified. When taking the open water diagram in Figure 4.9b into account, the design advance ratio is approx. at $J = 0.8$, where a steep increase of averaged propeller loadings is observed in case of an oblique inflow. With higher loadings the percental increase is lower and the values are below 10% at $J = 0.4$ in the simulation, as well as in the experimental results. The total forces and moments though, are higher in this case.

[4] A description of this method can be found at Carlton [20]. Corrections accounting for oblique inflow conditions are made to the original method, as described by Amini et al. [4].

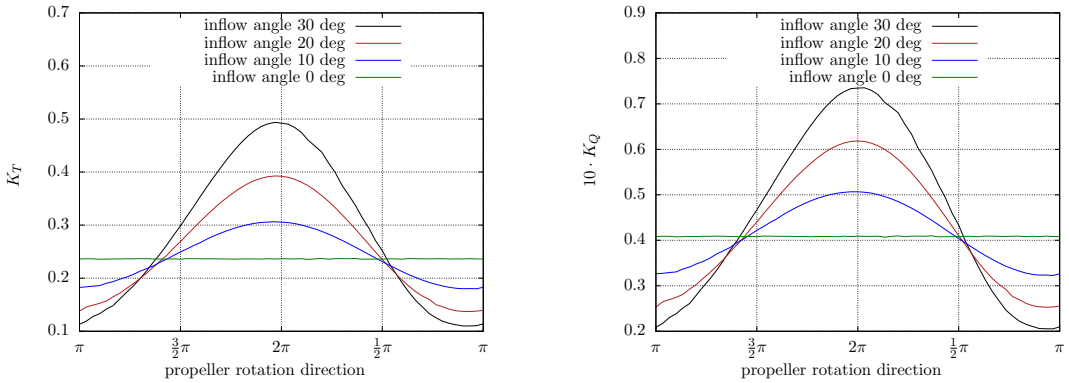

(a) Thrust coefficient K_T (b) Torque coefficient $10 \cdot K_Q$

Figure 4.16.: Single blade load fluctuations on Propeller B at $J = 0.8$

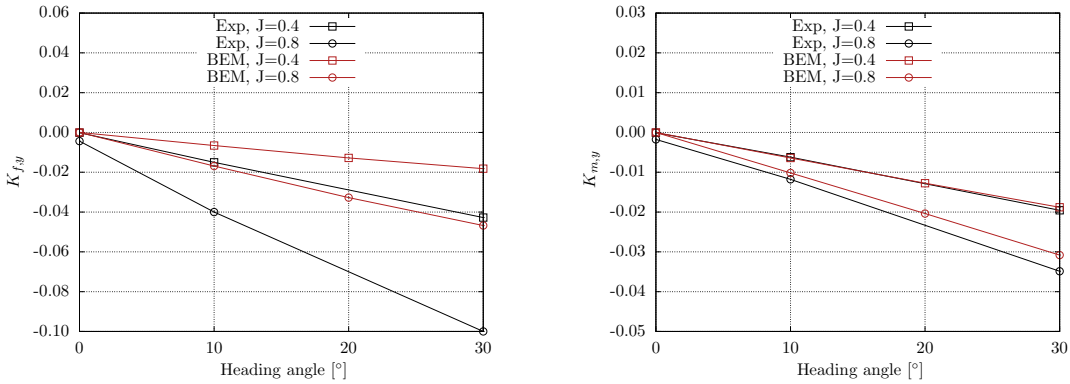

(a) Horizontal side force coefficient (b) Horizontal bending moment

Figure 4.17.: Influence of oblique inflow angle on average shaft loading of Propeller B

	J	unit	0°	10°	20°	30°	%-increase at 30°
T	0.4	$[N]$	51.2	51.6	52.7	54.2	5.9
Q	0.4	$[Nm]$	1.82	1.83	1.84	1.86	2.2
T	0.8	$[N]$	32.2	32.9	35.3	39.3	22.0
Q	0.8	$[Nm]$	1.39	1.41	1.47	1.57	12.9

Table 4.5.: Averaged blade loads on Propeller B at inclined inflow

The single-blade thrust fluctuations are an important measure in the load and fatigue analysis and they show high amplitudes in the case of a propeller subjected to inclined inflow. The values for K_T and $10 \cdot K_Q$ for the simulated cases are shown in Figure 4.16 for one propeller revolution at the advance ratio $J = 0.8$ because the variations are more pronounced in this case than for $J = 0.4$. It is visible that the fluctuations are drastically increasing with the inflow angle. Using the coordinate system defined in Figure 4.2, a negative heading angle of the propeller around the z'-axis leads to a smaller relative tangential velocity at a propeller blade when it is between 90° ($\frac{1}{2}\pi$) and 270° ($\frac{3}{2}\pi$) of a propeller rotation. In this situation, the thrust and torque at the blade reduces, whereas it increases between 270° and 90° when the rotation direction is in line with the flow direction. The lowest dynamic forces can be found around 170° of a propeller rotation for all heading angles and the highest forces at about 355°. This is only short before the minimum and maximum value of the effective inflow velocity at the blade generator line. The small shift of the extrema away from the theoretical values of 0° and 180° can be explained with the blade geometry, mainly the skew, which causes the working point of the thrust not to be located on the generator line. The amplitude of thrust fluctuations increases with heading angle and the largest thrust fluctuations can be found for a heading angle of 30° with a maximum value of 2.1 times the average thrust and 1.8 times the torque obtained at straight inflow.

As described in Section 2.1, the thrust becomes eccentrical for a propeller in a non-uniform inflow and side forces and bending moments occur. These are compared to experimental data obtained by Amini et al. [4] for the cases having a small influence due to the thruster housing and strut, which are included in the experimental setup but not in the *BEM* simulations. The results for the horizontal side force and bending moment coefficient obtained for the propeller coordinate system are presented in Figure 4.17. The tendency of the experimentally determined horizontal side forces given in Figure 4.17a can be reproduced by the *BEM* although they are underpredicted, showing a larger discrepancy at higher oblique inflow angles. The results are in line with the *BEM* results shown by Amini et al. [4]. Both the *BEM*- and experimental-curves show a constant gradient. The values are clearly underpredicted by the *BEM*, showing only about half of the value obtained in the experiments. This does not account for the

Wave Code	Static Propeller Immersion $[mm]$	Wave Height $[mm]$	Wave Period $[s]$	Advance Ratio
8250	250	260	1.5	0.6 / 0.9 / 1.2
8242	250	300	2.0	0.9 / 1.2
8216	250	300	2.5	0.9 / 1.2

Table 4.6.: Overview on simulation cases for Propeller A subjected to a wave potential

horizontal bending moment presented in Figure 4.17b, showing values similar to the experimental results. When the propeller is subjected to large oblique inflow angles, viscous effects, which cannot be determined using the non-viscous and irrotational approach of potential flow, become more pronounced in the flow field around the propeller blades. This makes the maximum oblique inflow angle that the propeller is subjected to an important criterion in evaluating the propeller performance within this thesis.

4.2.2. Propeller Blade Thrust under Consideration of a Wave Potential

In this section, a comparison is given between the thrust fluctuations of one propeller blade of the fully modelled Propeller A in regular waves calculated with the *BEM* and the experimental data acquired by *MARINTEK*. Because the interaction between propeller and free surface is not investigated here, only the cases where the propeller is deeply immersed are taken into account for the comparison. The numerical grid and solver conditions are comparable to those used in Section 4.2.1 and the experimental data is unpublished so far. The waves and propeller loadings considered in the following are given in Table 4.6. Here, the propeller immersion is $0.25m$, resulting in a clearance of $0.15m$ between blade tip and undisturbed free surface. Three different waves with a wave height between $0.26m$ and $0.3m$ and a period between $1.5s$ and $2.5s$ are investigated. A comparison is given only for higher advance ratios, where the free surface influence is small compared to the wave orbital velocities, so the medium value of normalised thrust fluctuations is approx. 1.0. If the propeller loading is higher, which is the case at $J = 0.6$ for the waves 8242 and 8216, the free surface influence is non-negligible and ventilation occurs in the experiments. Nevertheless, the fluctuations observed in the experimental results given in this section are not perfectly periodic. The results obtained for wave 8250 are thoroughly discussed in the following and those for the waves 8242 and 8216 are given in the Appendix B.2 in Figures B.3 to B.6 in order to show a comparison inheriting smaller free surface influences. A brief discussion is given at the end of this section.

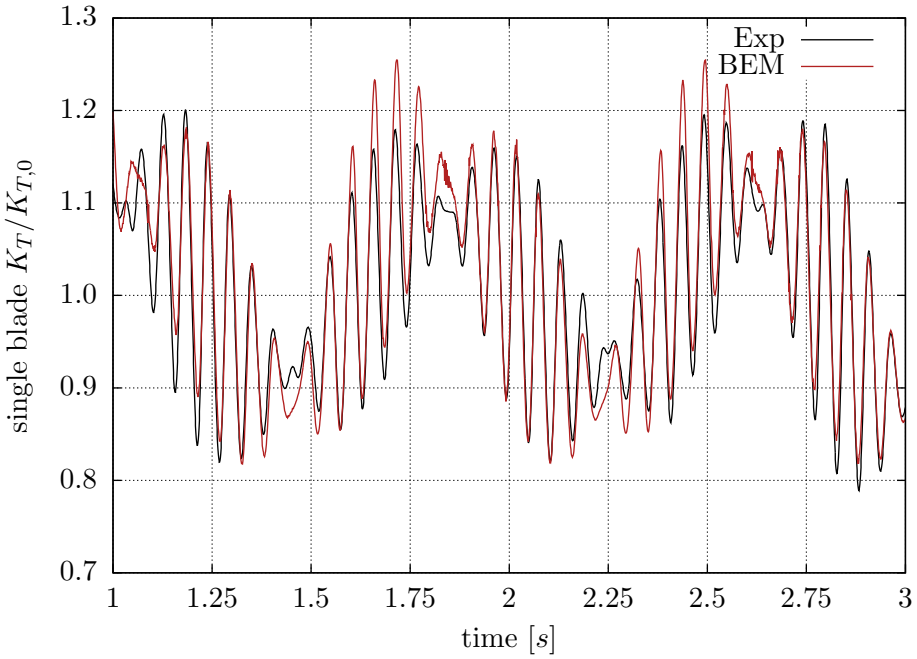

Figure 4.18.: Wave 8250 ($J = 0.6, K_{T,0} = 0.0862$)

In the results obtained for wave 8250, which are presented in Figures 4.18 to 4.20, the small-scale fluctuations refer to the propeller rotation frequency being $18Hz$ for all cases. The large-scale fluctuations show the encounter frequency between propeller advance velocity and wave phase velocity. This increases with a larger propeller advance ratio and depends on the wave period. The experimental data is obtained using a dynamometer with a $1200Hz$ sampling rate and the signal is filtered with a low-pass filter having a cut-off frequency of $160Hz$. The calculated results are not filtered and the time step is $9.26 \cdot 10^{-4}s$, referring to 6° of a propeller rotation. So, the *numerical sampling rate* is approx. $1080Hz$. For each experimental result, a time sequence with a length between $8s$ and $25s$ is provided by *MARINTEK*.

In Figure 4.18, the result for wave 8250 and $J = 0.6$ is displayed. The thrust of one propeller blade is shown non-dimensionalised with the value $K_{T,0}$, obtained for the deeply immersed propeller. Slightly different values $K_{T,0}$ are used for the simulation and the experimental data. For both results, the propeller blade frequency as well as the encounter frequency are clearly visible and in a good agreement. The measured thrust fluctuations are, at some stage of the time series, more pronounced than those of the simulations results, while both vacillate around the same average value. The mean value of both curves is slightly above 1.0, which is not the case in the curves

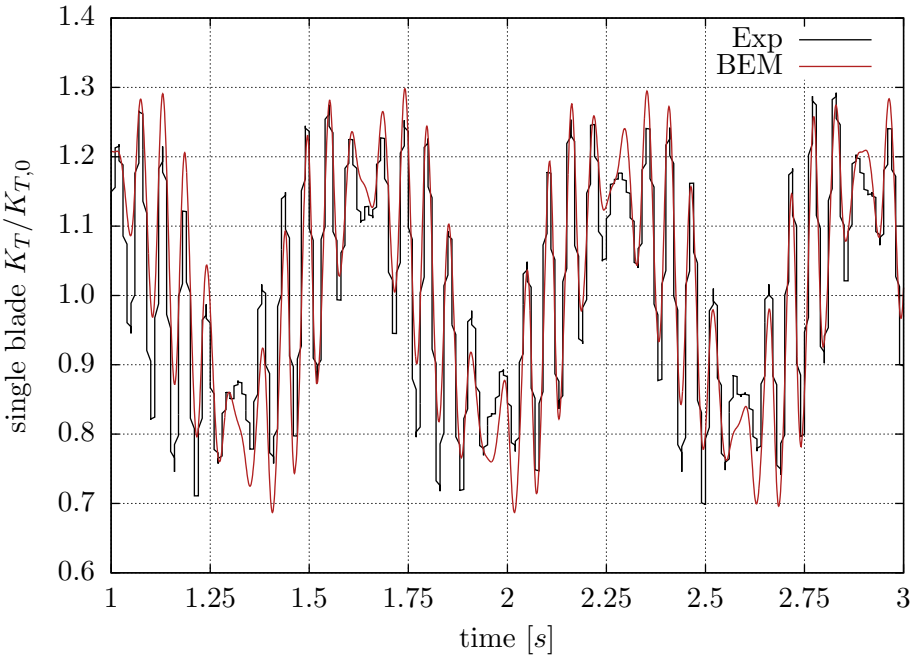

Figure 4.19.: Wave 8250 ($J = 0.9, K_{T,0} = 0.0574$)

for J-values other than 0.6 and the thrust fluctuates with an amplitude of approx. 20% around the medium value. The small-scale fluctuations with propeller rotation frequency are very regular, showing smaller amplitudes only near the min/max-values, where either the propeller is located at a wave crest or a trough. A possible cause may be that the orbital velocities are horizontal directly at the extrema which leads to a constant thrust, whereas the up- or downwards-directed velocity components lead to larger thrust deviations.

Similar to the results presented in Section 4.2.1, the percental thrust fluctuations are larger for a lightly loaded propeller as shown for $J = 0.9$ in Figure 4.19. Here, both the small and large frequency oscillations are larger compared to the $J = 0.6$-case, and again, the values of the latter are more pronounced in the experimental results. The curves showing the measured data are not smooth, denoting a distinct influence of the filtering. This can also be found in the results for $J = 1.2$ shown in Figure 4.20, where similar to the findings described above, the comparison between simulation and experiment is satisfactory. At this propeller loading, an obvious non-periodic behaviour can be observed in the experimental results, of which the most periodic $2s$-chronological sequence is chosen. The amplitude of fluctuations is approx. $30 - 50\%$ for $J = 0.9$ and $100 - 150\%$ for $J = 1.2$ because the absolute value is very low for the lowest loading.

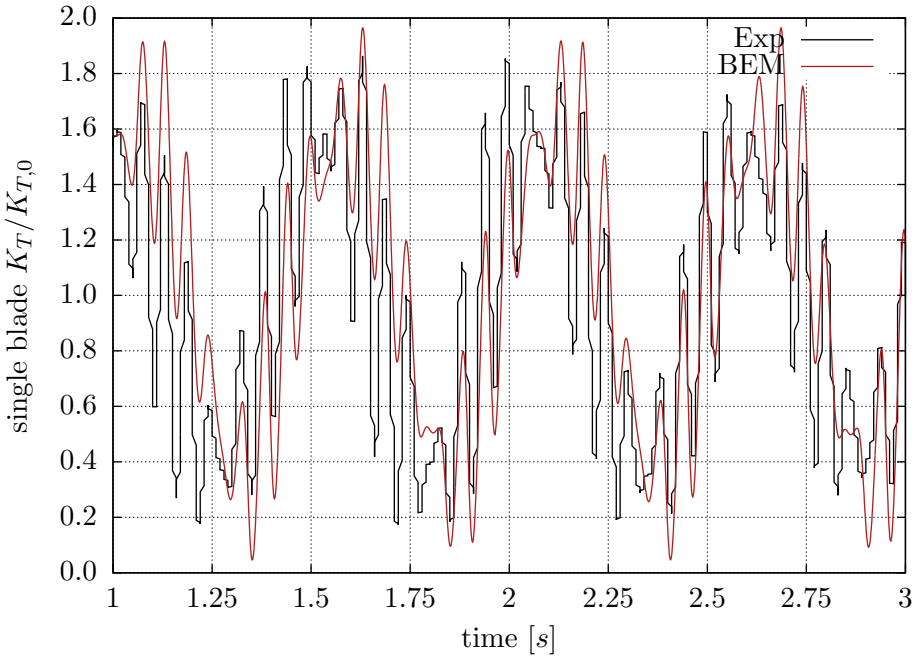

Figure 4.20.: Wave 8250 ($J = 1.2, K_{T,0} = 0.0222$)

When looking at the results of waves 8242 and 8216, the agreement between experimental and numerical results becomes slightly worse with higher wave elevation and a larger wave period. Reasons for this are the more pronounced free surface influence, which is not considered in the simulations in this section and the behaviour near the wave extrema where the measured thrust fluctuates less. The rotation rate-frequency fluctuations are, in general, larger in the experimental results. In the numerical results, these fluctuations are largest directly at or after the min / max values, which could also be observed for wave 8250 but to a smaller extent. In contrast, the measured fluctuations are largest at the wave flanks, where the orbital velocities are directed upwards or downwards. This is due to the fact that the encounter frequency is smaller and the effect of the direction of orbital velocities is more pronounced. As a result, the time-history of thrust forces is not in phase between the experimental and the simulation results when the blade is situated at a wave crest or a wave trough. A possible reason for this is the unsteady wake deformation in the *BEM*, which resulted in an underprediction of the forces, as seen in Section 4.2.1.

4.2.3. Propeller Side Forces under Consideration of a Wave Potential

In this section, the forces acting on Propeller B subjected to wave orbital velocities are compared to experimental data published by Amini et al. [6]. The numerical grid and the *BEM* solver settings can be found in Section 4.2.1. The loads measured by Amini et al. are gained with a dynamometer situated in a fixed position in the thruster strut, referring to the (x', y', z') coordinate system, as displayed in Figure 4.2. They represent the total loads on the thruster including the forces and moments acting on the thruster body and strut. Amini et al. published the unsteady data for the thruster in pushing and pulling condition including forces and moments at the described position for different advance and submergence ratios. In the *BEM* simulations, the largest submergence $H/D = 2.6$ is used for the propulsor in pulling condition, and in contrast to the experiments, the thruster body is not considered. Therefore, only the F_z-component of the force is compared here using the assumption that it is not greatly influenced by the housing. The F_y-component cannot be compared because the rotational slip-stream of the propeller induces a non-negligible effect on the thruster in y-direction, which is inherited by the experimental results. Furthermore, the experimental results are noisy, so the black lines shown in Figure 4.21 are obtained by filtering the original dataset with a low-pass filter with cut-off frequency of 5 Hz. This filter removes the noise together with the blade frequency variation and the wave-encounter frequency (which is lower than 5 Hz) is retained.

In the *BEM*, the propeller is simulated under a *virtual* free surface, meaning that the wave effect on the propeller, namely the orbital velocities, is taken into account, but the effect of the propeller on the free surface is not. This assumption is typical for experimental research, as open water tests are usually performed with this value of static immersion assuming a negligible free surface effect on the propeller. A comparison between experimental and numerical results is given in Figure 4.21. In 4.21a and 4.21b, the instantaneous wave elevation above the propeller position is given, showing the encounter frequency between wave and propeller. In Figures 4.21c and 4.21d, the time-history of the corresponding vertical forces F_z is shown. The *BEM* values are, in contrast to the experimental results, not filtered, showing a noisy characteristic, particularly for the high loading at $J = 0.2$. The phase of the forces is well captured for $J = 1.0$, while the amplitude is underpredicted by the *BEM* results. This is in line with the findings of Section 4.2.1 for the oblique inflow condition. Both curves show a positive average value of the vertical force. In the results for $J = 0.2$, a phase-shift between the measured and simulated values can be recognised together with a smaller amplitude in the *BEM* results, showing a similar deviation as in the $J = 1.0$-case. Here, the average value is approximately zero in the experimental results and shows a positive value in the *BEM* results.

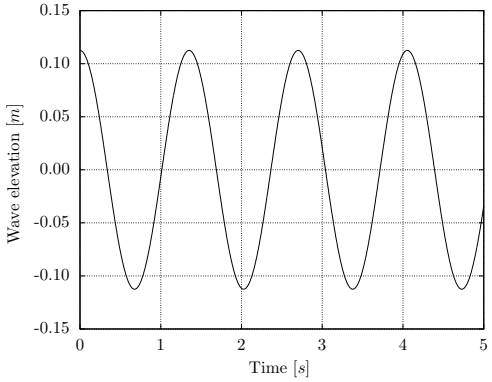

(a) Wave elevation above propeller position showing the encounter frequency ($T_w = 2s, J = 1.0$)

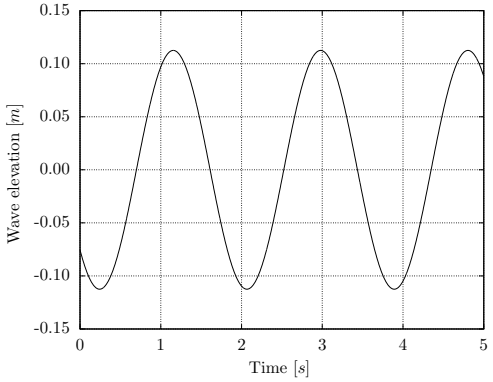

(b) Wave elevation above propeller position showing the encounter frequency ($T_w = 2s, J = 0.2$)

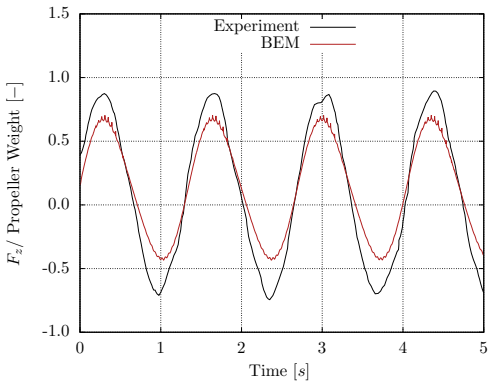

(c) Comparison between experimental and simulation results for vertical loads on propeller ($T_w = 2s, J = 1.0$)

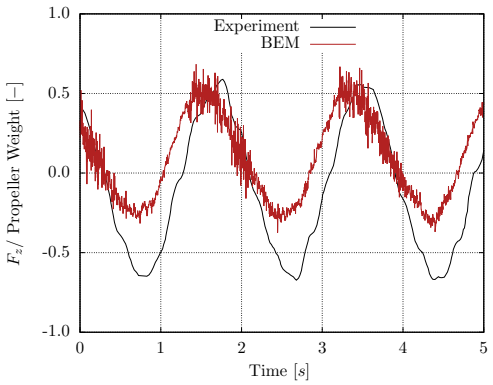

(d) Comparison between experimental and simulation results for vertical loads on propeller ($T_w = 2s, J = 0.2$)

Figure 4.21.: Results for Propeller B subjected to wave orbital velocities

4.3. Interactions with the Free Water Surface

4.3.1. The Effect of a 2D-Hydrofoil under the Free Water Surface

The NACA0012 hydrofoil described above, and for which a grid dependency study is conducted in Section 4.1.1, is investigated in this section in the vicinity of a free water surface. A result of this situation including a steadily moving, shallowly immersed hydrofoil is a wave train consisting of non-breaking waves above and aft of the foil. The grid with 96 panels on the body is used on the two-dimensional setup depicted in Figure 4.22, which is reproduced from experiments conducted by Duncan [25]. The Froude number based on the chord length of the hydrofoil is $F_c = 0.567$ and the immersion of the hydrofoil measured from the trailing edge is $h/c = 1.034$ and $h/c = 1.286$, respectively. The z-axis is pointing upwards and ζ is the actual elevation of the free surface at position x. The angle of attack is 5° nose up.

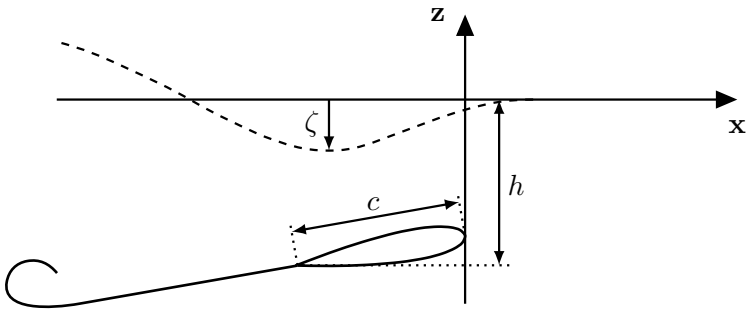

Figure 4.22.: Coordinate definition for NACA0012-hydrofoil under the free surface

At first, a grid dependency study of the free surface grid is conducted and the results in terms of the lift coefficient for both investigated cases are given in Figure 4.23a. The values are non-dimensionalised by the lift coefficient obtained with the finest grid. A monotone convergence with raising panel number can be observed and the grid with 300 panels in x-direction is chosen for further investigations because the error related to the finest grid solution is below 0.25%. This is confirmed by the findings observed in Figure 4.23b, where the free surface elevation is plotted for the different grids. A clear dependency of the elevation on the panel number leading to large differences in amplitude and wavelength can be seen. These differences are small for grid sizes above 200 panels, denoting a resolution of more than 20 panels per wavelength. This study is only depicted for $h/c = 1.034$, but the results are also obtained for the larger immersion at $h/c = 1.286$.

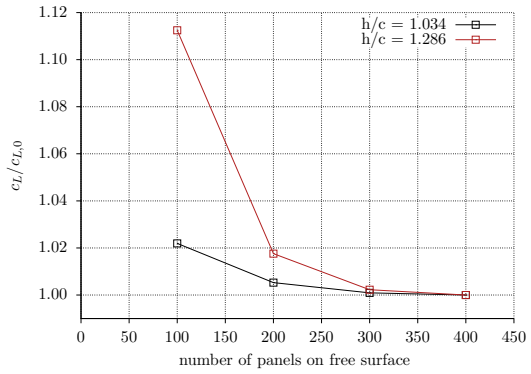

(a) Effect of panel number on lift coefficient

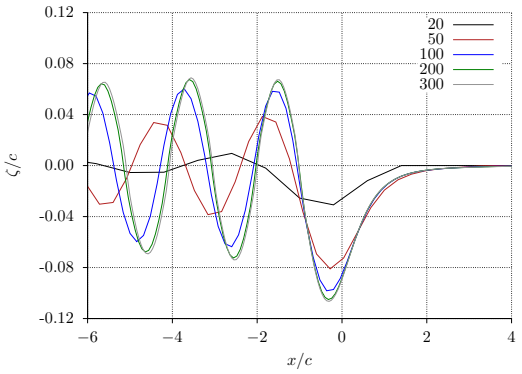

(b) Effect of panel number on free surface elevation ($h/c = 1.034$)

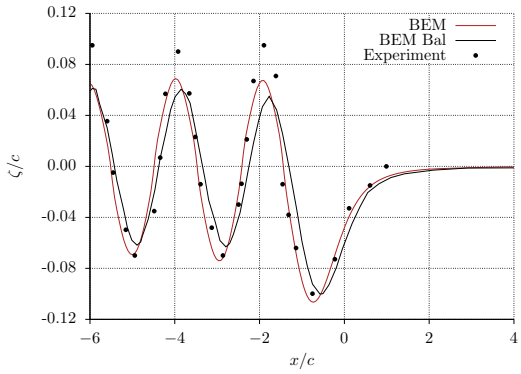

(c) Immersion $h/c = 1.034$

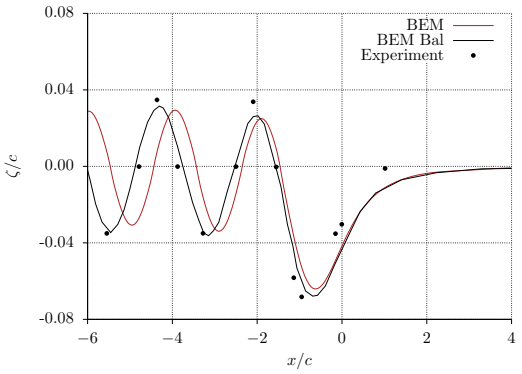

(d) Immersion $h/c = 1.286$

Figure 4.23.: Grid study for NACA0012-hydrofoil under the free surface ((a) and (b)) and *BEM* results for free surface elevation compared to experimental data by Duncan [25] and *BEM* results published by Bal and Kinnas [8] ((c) and (d))

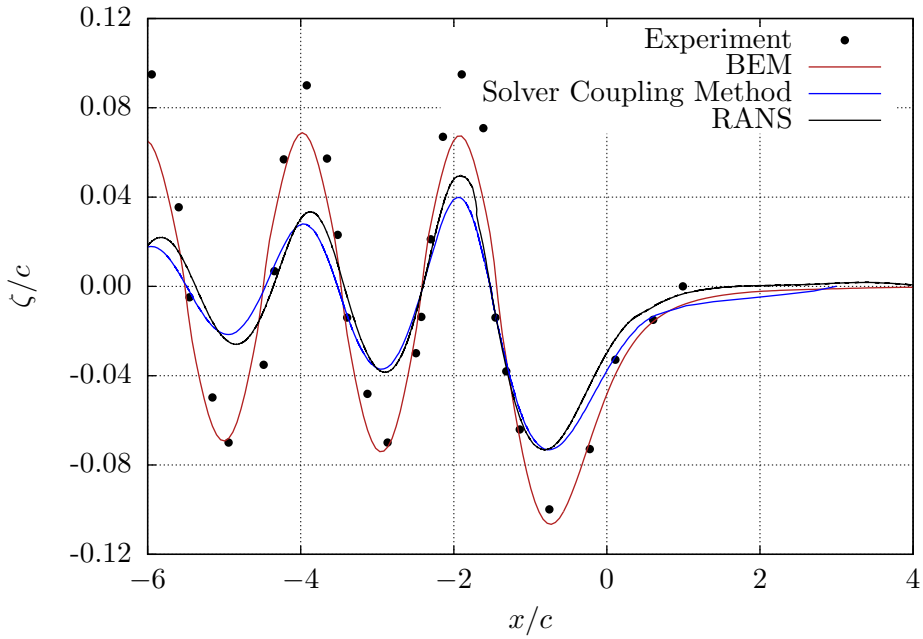

Figure 4.24.: Comparison of free surface elevation computed with the *BEM*, the solver coupling method and *RANSE* to experimental data ($h/c = 1.034$)

In Figures 4.23c and 4.23d, the results are presented and compared to experimental data and *BEM* simulations published by Bal and Kinnas [8]. At the smaller immersion $h/c = 1.034$ shown in Figure 4.23c, the phase and the wavelength of surface elevation is captured and the depth of the wave troughs show good agreement compared to the experimental data. The wave crests are lower than in the experiments, which is also the case for the *BEM* results of Bal and Kinnas. In the results obtained for the larger immersion $h/c = 1.286$ shown in Figure 4.23d, the wavelength is not exactly captured. This leads to a difference compared to the experimental data as well as to the *BEM* results by Bal and Kinnas for the free surface elevation aft of the hydrofoil, which is not captured as good as for the shallow immersion.

For this simulation case, a comparison of the results obtained with the solver coupling method is additionally presented in Figure 4.24. A submerged hydrofoil represents a challenging validation case for a *RANSE* solver using the *Volume-of-Fluid* method[5], so the results obtained by Wöckner-Kluwe [98] and plotted as the black curve are also

[5] This is outlined in several publications, e.g. by Vaz et al. [96], where the *RANSE* results of different solvers are compared against the experimental data and very fine grids are required for a grid-independent solution.

taken into account. The red curve is the same as in Figure 4.23c for comparison; the blue curve shows the results computed with the solver coupling method. The domain size of the *RANSE* grid used is equal for the *RANSE* and the coupling cases, with a length of 18-times the chord length and $4.5 \cdot c$ in front of the hydrofoil. The grid used in the *RANSE* simulation contains $50k$ cells with refinement areas at the undisturbed free surface position and around the hydrofoil and its supposed trailing wake zone. The shape of the volumetric cells in the grid for the coupling simulation is Cartesian in the whole domain because no body is present and the refinement is limited to the free surface position resulting in a grid-size of $45k$ cells. A quite large discrepancy becomes obvious between the *RANSE*-based simulations and the experimental results. Because the results of the solver coupling method are unlikely to be closer to the measurements than the *RANSE* results, these two curves must be compared with each other. They show a good agreement except for small differences at the first wave crest. This is a promising result because the main effects of a lift-producing body on the free surface in a *RANSE* simulation can be reproduced by the coupling procedure.

4.3.2. Wave Drag of a 3D-Spheroid

This section reports on numerical simulations conducted with a three-dimensional spheroid shallowly immersed under a free water surface. The wave drag is compared to numerical results published by Uslu and Bal [95] and experimental results from Chey [23]. A sketch of the simulation case and the length parameters used is given in Figure 4.3. In the first case, the immersion of the spheroid is fixed to 25% of its length ($d/a = 0.5$) and the width ratio a/b is varied between 4.0 and 8.0. In the latter, the width is constant and the immersion ratio is changed between $d/a = 0.25$ and $d/a = 0.5$. The range of Froude numbers is from 0.4 to 0.8 in both cases. In order to present grid-independent results, grid studies are conducted for the spheroid first and for the free surface prior to the validation cases.

The forces acting on a fully submerged spheroid cannot be computed physically correct by a *BEM* because its drag consists only of the frictional resistance and a resistance induced by the wake behind the blunt body. These viscous effects are supressed by the non-viscous and non-rotational numerical method, which is congruent with the fact that a closed and deeply submerged body is not subjected to a resistance force in a potential flow field. The stagnation pressure at the bow is balanced by the same at the stern and therefore, a grid dependency of the solution is a matter of a proper resolution of the spheroid in these areas. When a free water surface is considered above a shallowly submerged spheroid, the body will experience a resistance force because the flow is obstructed between it and the water surface. The pressure reduces on the upper side of the spheroid and a wave system establishes, which in turn changes the pressure on the

body to be non-symmetric between the fore- and aft-part. The stagnation pressure on the stern no longer balances the bow pressure. In this situation, grid dependency has to be studied for both grids, and furthermore, the size of the free surface grid must be chosen according to the problem. The size of the surface is 65 x 40 to prevent boundary influences for a spheroid with a non-dimensional length of 12.

A grid-dependency study of the spheroid case at $Fn = 0.4$ with the presence of a water surface is given in Figure 4.25a. The free surface grid has 65 x 40 panels. The grid of the spheroid is refined in a structured manner, where the longitudinal panel number is $18x + 9$ and the circumferential panel number is $8y + 4$, for $x, y \in [0, 1, 2, 3, 4]$. Because the forces are far from the converged value, the coarsest grid is not shown in Figures 4.25a and 4.25b. A clear dependency of the lift and drag forces on the grid size can be found in Figure 4.25a, while the convergence behaviour for the drag is much better than for the lift. The grid with 900 panels (45 x 20) on the body of the spheroid is chosen for further investigations because the difference of the lift force, as the quantity of interest, is below 1% compared to the finest grid solution. In Figure 4.25b, the results of the subsequent grid study conducted for the free surface grid are shown. The grid size is chosen is such a manner that the initial panel surface area is of quadratic shape. It can be seen that a high number of panels is needed for computing grid-independent results for $Fn = 0.4$. This is due to the fact that the waves produced at slow speeds are short and a specific number of lengthwise panels per wavelength is needed to resolve the wave profile. For this reason, the results for $Fn = 0.8$ converge faster to the finest grid value having a wavelength of approx. half the wavelength computed at $Fn = 0.4$. An exemplary finding is that the result obtained with the grid with 2600 panels (65 x 40) shows a deviation larger than 10% to the finest-grid solution at $Fn = 0.4$, whereas it is only 1.6% for $Fn = 0.8$. In order to constrain the simulation time, this free surface grid is chosen for all further investigations. A possible solution for a faster grid convergence in the slow-speed cases would be to use a grid length related to the Froude number, so a defined number of wavelengths is always computed. Then the panel number could be the same for all cases. When the grid is coarse, the drag is overpredicted for $Fn = 0.4$, while it is underpredicted for the large velocity.

In Figure 4.26, the results for the wave drag coefficient of a spheroid computed with the steady free surface b.c. are presented and compared to the *BEM* results of Uslu and Bal [95] in 4.26a and to experimental values obtained by Chey [23] in 4.26b. Note, that the definition of the wave drag coefficient c_w used here is different to the one used in the publication of Uslu and Bal. The simulations shown in Figure 4.26a are conducted for the spheroid having three different length to diameter (a/b) ratios. The wave drag values obtained are very close to those given by Uslu and Bal [95] for all speeds, except for the slowest speed, referring to $Fn = 0.4$. This deviation results only partly from the too coarse grid, which is discussed above. Differences also occur for the widest body with $a/b = 4.5$ at higher Froude numbers. This is also the case

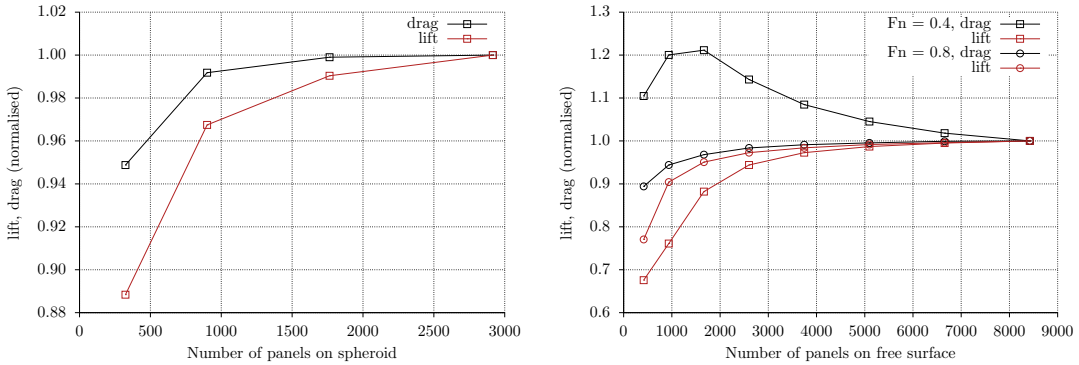

(a) Grid study of spheroid grid ($Fn = 0.4$)

(b) Grid study of free surface grid

Figure 4.25.: Grid dependency studies for spheroid case ($a/b = 6.0, d/a = 0.5$)

in the publication of Uslu and Bal, where the authors compare their results to those obtained with a different numerical method presented by Farell [26]. Because the waves become more steep for a wider body travelling at a higher velocity, this case is more challenging for a numerical method and the steepness of the waves is limited due to the linearity of the steady combined boundary condition. When comparing the simulation results to experimental values obtained by Chey [23] in Figure 4.26b for a spheroid with $a/b = 8.0$ at different immersion rates, the agreement is satisfactory. The *BEM* results show an overprediction of the wave drag values for the larger immersion ratios $d/a = 0.5$ and $d/a = 0.375$, compared to the experimental data. At the smallest immersion rate $d/a = 0.25$, where the clearance between body and undisturbed free surface is equivalent to the smaller radius b, the agreement is better. The overall agreement is satisfactory, in particular for the medium values of the computed range of Froude numbers.

In order to present a validation of the unsteady formulation of the free surface boundary conditions, the stationary case of the immersed spheroid travelling at constant speed is also computed with this b.c. type. The results are obtained with the same numerical grids and are presented in Figure 4.27. One obvious difference to the steady results given in Figure 4.26 is the improved prediction of the $Fn = 0.4$-cases in Figure 4.27a. Here, the values computed show a good agreement compared to the *BEM* results given by Uslu and Bal [95]. The wave drag values presented in Figure 4.27b show a similar overprediction as those computed with the steady formulation for $Fn = 0.6$ and above, when compared to the measured data. A remarkable difference can be found at slow speeds, where the values are considerably below the experimental results and show a contrary trend compared to the stationary data. Overall, a good agreement is found both between the computed values using either the steady or the unsteady formulation and towards the published *BEM* and experimental results.

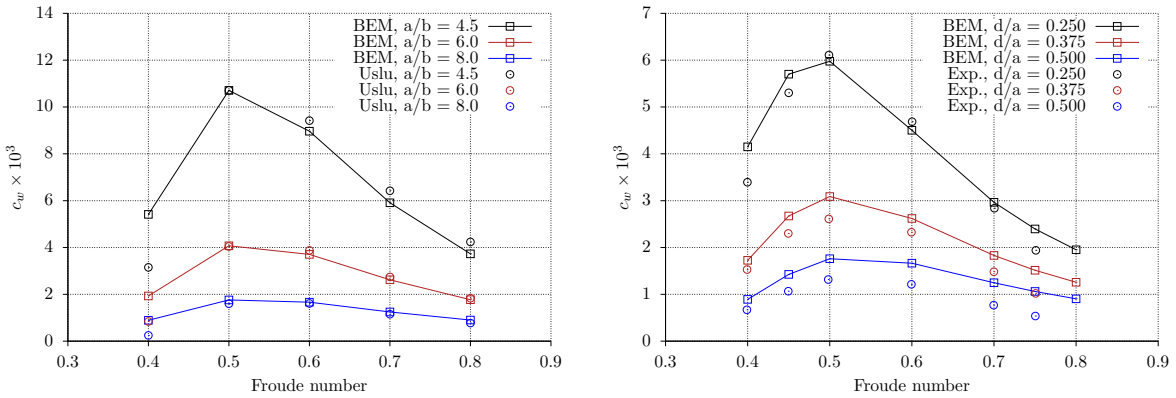

(a) Comparison to *BEM* results from Uslu and Bal [95] for different widths of spheroid ($d/a = 0.5$)

(b) Comparison to experimental results by Chey [23] for different immersion rates of spheroid ($a/b = 8.0$)

Figure 4.26.: Wave drag of spheroid computed with the linear, steady b.c.

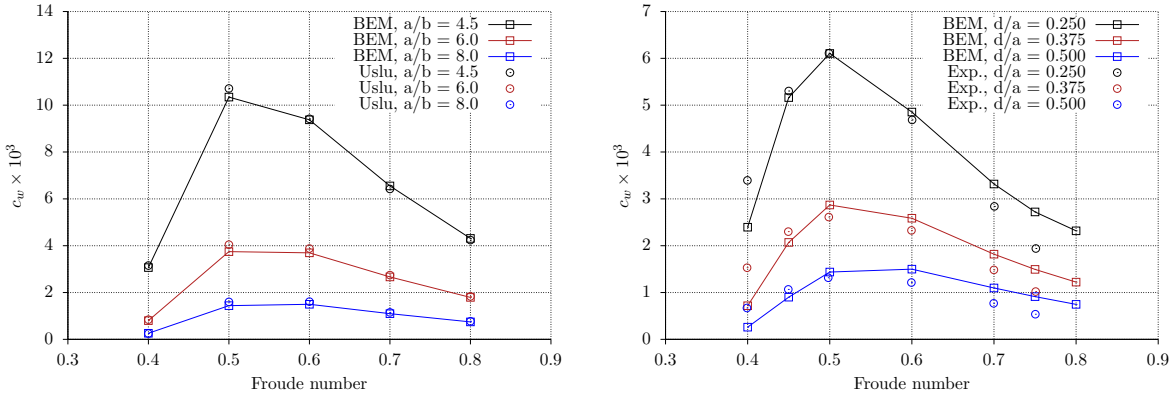

(a) Comparison to *BEM* results from Uslu and Bal [95] for different widths of spheroid ($d/a = 0.5$)

(b) Comparison to experimental results by Chey [23] for different immersion rates of spheroid ($a/b = 8.0$)

Figure 4.27.: Wave drag of spheroid computed with the unsteady b.c.

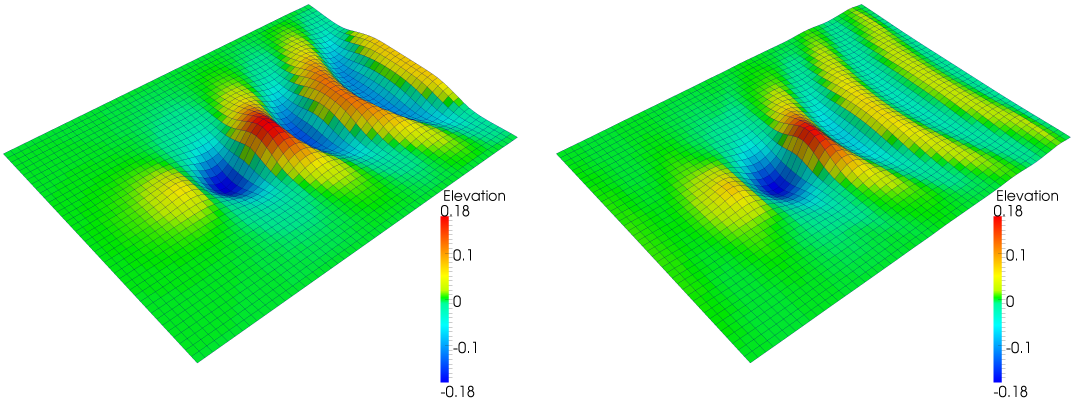

(a) Steady formulation of b.c.

(b) Unsteady formulation of b.c.

Figure 4.28.: Computed wave elevation for the immersed spheroid, representation is 20-times enhanced ($Fn = 0.4, a/b = 6.0, d/a = 0.5$)

In Figures 4.28 and 4.29, two exemplary wave patterns obtained for the submerged spheroid are shown. The grids on the spheroid described above and the free surface with 900 and 2600 panels are used, the immersion rate is $d/a = 0.5$ and the spheroid length ratio is $a/b = 6.0$. A comparison is given between results computed with the steady and the unsteady formulation of the boundary condition. It can be seen that the transport of the disturbance due to the body is more pronounced in the steady case and the wave system is more pronounced. This is a result of the six-point upwind differencing scheme used in the steady formulation. A numerical damping of the free surface elevation is found in the unsteady results, where the transport in the time marching scheme is maintained using central differencing schemes. The waves produced directly above the body, which greatly determine the body's lift and resistance, are very similar. Another finding is that the waves are steeper when using the unsteady formulation, which is not linearised. Furthermore, when looking at the wave elevation for $Fn = 0.8$ in Figure 4.29b, small disturbances occur near the downstream boundary of the discretised part of the free surface. The unsteady simulations are conducted with a damping region upstream of the body and a smoothing of potential and elevation of the free surface.

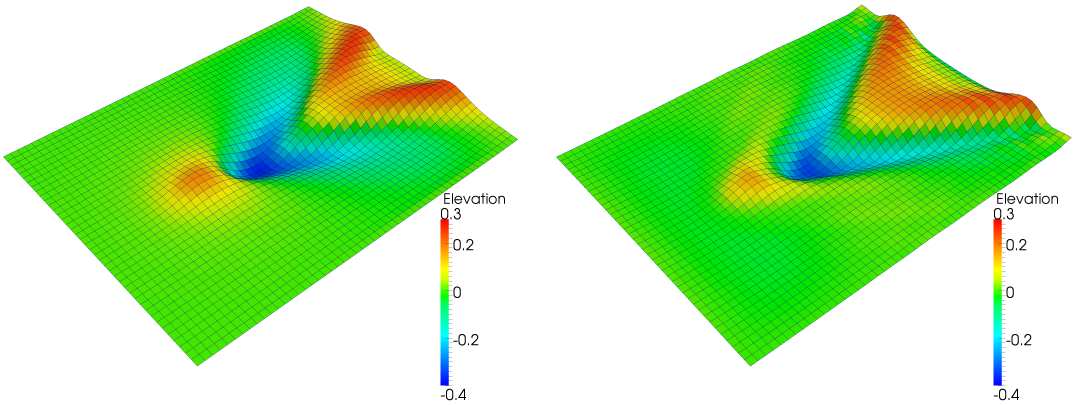

(a) Steady formulation of b.c.

(b) Unsteady formulation of b.c.

Figure 4.29.: Computed wave elevation for the immersed spheroid, representation is 10-times enhanced ($Fn = 0.8, a/b = 6.0, d/a = 0.5$)

4.4. Discussion and Conclusions

In this chapter, a validation of the numerical procedures regarding the relevant physical effects for a propeller under unsteady conditions and in the vicinity of a free water surface is addressed. Therefore, geometries are chosen for which both suitable model-test results are available and the geometry is propeller-like or significantly disturbs the free surface. The chapter is divided into three main parts. In Section 4.1, grid studies are given in order to demonstrate the convergence behaviour of the methods for the relevant geometries. In the second part, three validation cases addressing dynamic propeller loads for deeply submerged propellers are given, and in the last part, the interaction between propellers and other bodies and the free water surface is studied and compared to experimental data.

At first, in Section 4.1.1, simulations are conducted for a two-dimensional hydrofoil, which captures important propeller physics, such as the lift and drag forces resulting in the thrust and torque. A good grid convergence can be observed and the computed pressure distribution for different angles of attack agrees well with experimental validation data. The grid needs to be chosen in order to refine the areas with a steep pressure gradient. They are, in case of a hydrofoil or a propeller, situated near the leading edge, in particular on the suction side where more pronounced pressure extrema occur in contrast to the pressure side. At the trailing edge, the grid refinement is mainly important for capturing the alignment of pressure on both sides of the hydrofoil with a strong influence on the drag value, because the pressure gradient is nearly zero on the pressure side and has a significant value on the suction side. For very fine grids, the pressure extrema determined on suction and pressure side in the experiments is nearly exactly reproduced by the *BEM* simulations. Moreover, the modelling of the wake surfaces is an important issue because the theoretical wake length is infinite. Here, a wake length referring to ten chordlengths is chosen, but a larger value still improves the result quality. But, for more complex geometries, the wake length has a major influence on the simulation time and has to be chosen with caution. If a far-field wake model would be implemented, this issue could be eased. Overall, a linear convergence behaviour of the method can be observed in the grid study in consequence of the linearity of the method.

In a next step, a grid study for a propeller is conducted in 4.1.2 and the open water performance of propellers is determined. This case shows a good grid convergence behaviour and a grid with 28x42 panels on the blade is chosen, referring to 28 panels in radial direction and 21 on each side of the blade. Again, the leading edge area has to be refined for two reasons. The first being that the geometry of the blade, which can be extremely sharp in the upper radii, has to be captured by the grid. Also, the round leading edge having a small radius has to be resolved by the numerical grid. The

second reason was mentioned before and refers to the resolution of the pressure peaks. Moreover, the location of this peak changes with different propeller thrust loadings and different blade radius, so the actual position is initially unknown. Here, an adaption of the refinement can be necessary after reviewing the pressure distribution on the blade. Also, the grid in the *BEM* has to be well chosen and the results treated with caution because there is only negligible numerical damping and hence instabilities can occur. An important part of the blade in this context is furthermore the tip region, where highly distorted panels and numerical errors can occur. This does not account for the hub region of the blade, where the nose radius and the chord length are usually large, but an interaction between the blade and the hub takes place. The propeller hub is taken into account only for computing the open water curves in this work and a study of grid effects is not given. A negative effect is imposed by the hub on the free wake surfaces, as numerical instabilities can occur because the edges of the wake panels, being a vortex ring for integrating the induced properties, can be situated very close to the collocation points of the hub panels. Special care has to be taken in this case.

When deforming the wake panels due to the local velocity, the free wake deformation only works as intended if the grid spacing, having a major influence on both the simulation time and the results, is adjusted to the problem. The wake shape depends on the blade grid, the iteration step size, the blade geometry and the propeller loading. For determining the open water properties, an iteration step size referring to 6° of a propeller rotation is found to be suitable for the two computed propellers. Due to the discussed shortcomings of the *BEM* and other potential-based simulation tools, not all physical effects can be depicted and the thrust and in particular the torque of propellers is underpredicted. Therefore, a fixed-wake approach with prescribed wake pitch is used.

In the third part of Section 4.1, a validation of the coupling procedure is given, starting with grid-studies in both involved solvers, the *BEM* and the *RANSE* solver. The computational case refers to a single-bladed propeller. This simple case is chosen in order to supress unwanted side-effects due to an interaction with other bodies or between the blades of a multi-bladed propeller. The grid studies conducted for both baseline methods show good convergence behaviour and acceptable results for the thrust forces can even be obtained with very coarse grids. The simulation with the *RANSE* grid consisting of an empty cuboid and having only $27k$ cells already produces results within a 10%-range to the finest-grid solution. Details of the flow field, however, can only be captured when using a finer grid. Also, geometrical details, such as the leading edge position, can be represented by the body forces when the *RANSE* grid has a cell edge-length below $D/20$.

A large part of Section 4.1.3 is devoted to investigating the propeller-induced velocities computed by both solvers. A comprehensive study is given for a variation of several

simulation parameters, while the induced velocity components show a good agreement between the methods for a wide range of parameters. The most difficult quantity to determine is the distance of the transfer plane, in which the velocity distribution is passed from the *RANSE* solver to the *BEM*. In order to still capture the correct velocity field the propeller is subjected to, the plane should be located as close as possible to the propeller. But it must not be too close because of the propeller geometry extending in front of its origin and the leading edge vortex, which distorts the propeller-induced velocities. The exact position has to be chosen with care for each simulation case using the solver coupling method. For the investigated case, the distance is $dx = 0.5R$ measured from the propeller origin to the centre of the plane. The induced velocities are in line for both solvers, which is also confirmed in simulations conducted for a four-bladed propeller. When comparing the results to *RANSE* results inheriting a geometrically modelled propeller, differences become obvious. Compared to the far lower computational costs with only a tenth of grid cells involved, these are acceptable. It can be stated from Section 4.1 that the solver coupling method is capable of simulating propeller effects for open water cases. The induced velocities are predicted well, so it is assumed that a computation of the interaction of a propeller with other bodies is possible.

In 4.2, a validation of the dynamic propeller loads computed by the *BEM* is given. At first, the propeller forces when subjected to an inclined inflow are determined and compared to experimental data obtained for a fully equipped thruster propeller in 4.2.1. In the simulations only the propeller blades are modelled and the results show an underpredicted load increase at oblique inflow angles above 10°. This can be partly a result of the simplified computational model and also of increasing viscous effects for higher inflow angles. The angles due to wave orbital velocities are expected to be in the range of 10°, resulting in thrust fluctuations of about ±20% around the value $K_{T,0}$ obtained for straight inflow conditions. This is confirmed by experiments conducted by Koushan et al. [59]. For higher angles, the *BEM* results seem to be underestimated, but the thrust and torque fluctuations observed for a single blade during one propeller rotation are still large. They can reach values of more than twice the value obtained for straight inflow conditions at $J = 0.8$, but they are unlikely to occur when only taking wave orbital velocities into account. Oblique inflow angles above 10° will most likely occur when ship motions are superposed, which is not aimed at here. Such simulations have been conducted using the solver coupling method in the *ProSee* project [2].

In 4.2.2 and 4.2.3, the normalised propeller blade thrust and the side forces due to waves for a deeply immersed propeller are investigated by *BEM* simulations. A comparison is made to experimental data for the cases which are not affected by free surface effects, and the results are promising. The simulations are conducted with a coarser grid than in 4.1.2 and dozens of propeller revolutions and several encounter periods can be simulated within a few hours of simulation time on a standard workstation. When

comparing the side forces, only those little influenced by the thruster housing and strut are compared to the experimental data. The simulations evaluated in 4.2.3 are also conducted at a very high propulsor loading at $J = 0.2$ and still, the numerical results show a similar trend compared to the experimental although the difference is larger and the time-history is not smooth. Overall, the dynamic propeller behaviour can be depicted well, the simulations are stable and the results of the validation simulations show the applicability of the method for wave-influenced propulsors.

Section 4.3 gives three validation cases for the free water surface model implemented in the *BEM*. The first refers to the two-dimensional case of a shallowly submerged NACA0012 hydrofoil, for which a grid study is conducted in 4.1.1. A grid study on the water surface is given for two different immersions of the foil and a comparison between the computed and an experimentally determined free surface profile is presented. Also, *BEM* results published by Bal and Kinnas [8] are taken into consideration. The computed results show a good agreement compared to the measured results in terms of the amplitude and phase of the free surface waves. Furthermore, the wave profile determined with the solver coupling method and a *RANSE* solver are presented, showing a larger deviation because this case seems to be very challenging for *VoF* methods, as e.g. discussed by Vaz et al. [96]. But, the results determined with the solver coupling method are in fair agreement with those of the *RANSE* method obtained with a much finer grid and the geometry of the foil resolved within the simulation. The results of the *BEM* show that the free surface waves need to be resolved by about ten to 15 panels per wavelength, resulting in an approximate 10% difference to the converged value. For a deviation below 2%, 20 or more panels are needed. This can result in a large number of panels in case of a three-dimensional simulation and is due to linear *BEM* formulation. In case of a higher-order formulation, lower panel numbers would be possible, but the costs for determining the induced potential and velocities would be higher. The 2D simulation is very fast and the results of the lift producing body agree well with the experiments.

The last validation case given in Section 4.3.2 is a three-dimensional case inheriting the free water surface and a shallowly immersed spheroid. The results are computed with the steady and the unsteady formulation of the free surface b.c. and compared against experimental results and other *BEM* simulations. The Froude number range is between $Fn = 0.4$ and $Fn = 0.8$ and a grid study on the spheroid and the free surface is conducted first for both limits of the Froude number-range. A good convergence behaviour can be observed, while much finer grids are needed for the slower speed due to the smaller wavelength. This is a known behaviour, and in this case the grid chosen for all further simulation is kept constant. For future investigations, it is recommended to relate the free surface dimensions and the panel spacing to the Fn and the body dimensions, so for each case the same number of wavelengths is inherited and each wave is represented by the same number of panels. Both the steady and the unsteady results

are compared to values taken from the literature and the results show a good agreement. For larger Froude numbers and wide bodies, deviations occur due to more pronounced viscous effects and steep waves. A comparison between the results obtained with the steady and the unsteady b.c. shows only minor differences. When investigating the free surface elevation, a smoother representation in case of the steady simulations compared to the unsteady case becomes obvious. This is due to the directed six-point upwind difference used in the steady formulation. The non-directed central differencing scheme shows point-to-point oscillations in the unsteady simulations, where also a smoothing at the inlet boundary is necessary.

A large difference between the simulations is furthermore the simulation time. A steady calculation typically needs five to ten iteration steps for a converged result because the six-point upwind difference is directly put in and solved in the *SLE*. The physical quantities are transported over the total free surface length in the first solution. When the unsteady formulation is used, the source strength of the free surface panels is solved in the *SLE*, the disturbance is generated directly above the body and has to be transported through the whole domain with the time-stepping procedure. This can take some time depending on the Froude number and often hundreds of time steps are needed. Moreover, the discrepancy is intensified due to restrictions applying to the time step size in unsteady simulations because of the explicit time integration scheme. Using *Courant Numbers* c_r in the range between 0.5 and 1.5 shows good results, while the simulations become unstable outside of this range.

5. Applications

This chapter provides comparisons of propeller blade forces determined with *BEM* simulations and those conducted using the solver coupling method described in Section 3.3. The simulation results are compared to experimental data acquired by *MARINTEK* and made available within the *MARTEC* project *PropSeas*. As a reference, *RANSE* simulations by Wöckner-Kluwe [98] (sec. 5.2 and 5.3) are also taken into account. The unsteady free surface model described above and the panel split technique are utilised.

In Section 5.1, the simulations refer to a propeller with varying immersion in calm water. These cases are comparable to open water propeller cases with a decreased hub-immersion H. The immersion ratios are $H/R = 1.5$, $H/R = 1.0$ and $H/R = 0.0$, respectively. In the most shallow case, the hub-centre of the propeller is at the position of the undisturbed free surface-height. In Section 5.2, the simulations refer to a shallowly immersed propeller operating in long-crested head-waves. Again, the immersion of the propeller hub is variable in conjunction with the wave parameters, which are varied in terms of wave height and period. The experimental data and the *RANSE* simulations utilised in Section 5.1 have been published by Kozlowska et al. [62] in a similar manner. More information on the experimental test set-up for determining the propeller loads presented in Section 5.2 can be found at Amini [3]. The propeller used in both sections refers to Propeller A described at the beginning of Chapter 4.

5.1. Propeller with Varying Immersion

In the following, a comparison between numerical results obtained with different approaches and experimentally determined propeller blade loads is presented. Most of the simulations refer to those conducted with the solver coupling method, while some are obtained using the *BEM* or a *RANSE* solver. The case is Propeller A in model scale operating shallowly immersed in open water conditions at hub immersion rates $H/R = 1.5$, $H/R = 1.0$ and $H/R = 0.0$. These cases are very challenging for all numerical methods, because of a combined occurrence of ventilation and cavitation and a pronounced unsteadiness of the flow field. The results are given in terms of the dimensionless single-blade loads for several propeller rotations over the rotation angle φ, for $\varphi = 0$ referring to the topmost position. The cases simulated are summarised in Table

Immersion rate $H/R[-]$	Advance ratio $J[-]$
1.5	0.15 / 0.3 / 0.6
1.0	0.15 / 0.3 / 0.6 / 0.9
0.0	0.15 / 0.3 / 0.6

Table 5.1.: Simulation cases for shallowly immersed propeller under open water conditions

5.1. Because the *absolute* thrust values K_{T_0} are very low for $J = 0.9$ and $J = 1.2$, the comparison is of little significance and is only given for $H/R = 1.0$ and $J = 0.9$.

The *BEM* simulations are conducted with a blade grid with 16 x 24 panels, a wake length of 200° and a time-increment to 10° of a propeller rotation. These values differ from those used above, in order to reduce the computational costs and because an approx. 5% error in the *BEM* results is accepted assuming that the relative trend of the forces can be reproduced. Again, the wake surfaces are aligned freely towards the local total velocity. The grids used in the simulations put through with the solver coupling method inherit 16 x 34 panels for the *BEM* and $270k$ cells in the *RANSE* domain, including a refinement area in the free surface region. The *BEM* grid is finer in tangential direction in this case in order to get a clearer representation of the leading edge geometry. In the *RANSE* simulations conducted by Wöckner-Kluwe [98], a cylindrical domain with a diameter and a length of $10D$ and inheriting $2.7m$ cells is used. The large number of grid cells results from a necessary refinement of the free water surface altering its position compared to the grid, as the whole cylinder rotates with the propeller. The time step refers to 0.45° of a propeller rotation, resulting from Courant number restrictions of the *VoF* model. This leads to an approximate simulation time of one week when 16 cores of a cluster node are used. The standard $k - \omega$ turbulence model is used. Without the refinement areas at the free water surface, the *RANSE* grid around the propeller inherits $800k$ cells.

The results given below can be compared to experiments and *RANSE* simulations published by Califano [16], who addressed similar cases for Propeller B. He characterised three different types of ventilation, observed in photographs and videos from the experiments (see Califano [16], sec. 1.3). For a propeller showing little ventilation, a *free surface vortex* like a hose from the water surface towards the blade tip is established. For a higher load or a smaller immersion, these cases become *ventilating*, so the blade sucks air into the water and often a long tube is formed keeping its position at the upper blade radii and in some cases being entrained for a whole rotation. Between these two cases, Califano characterises an *intermediate* condition when both situations occur within one test run.

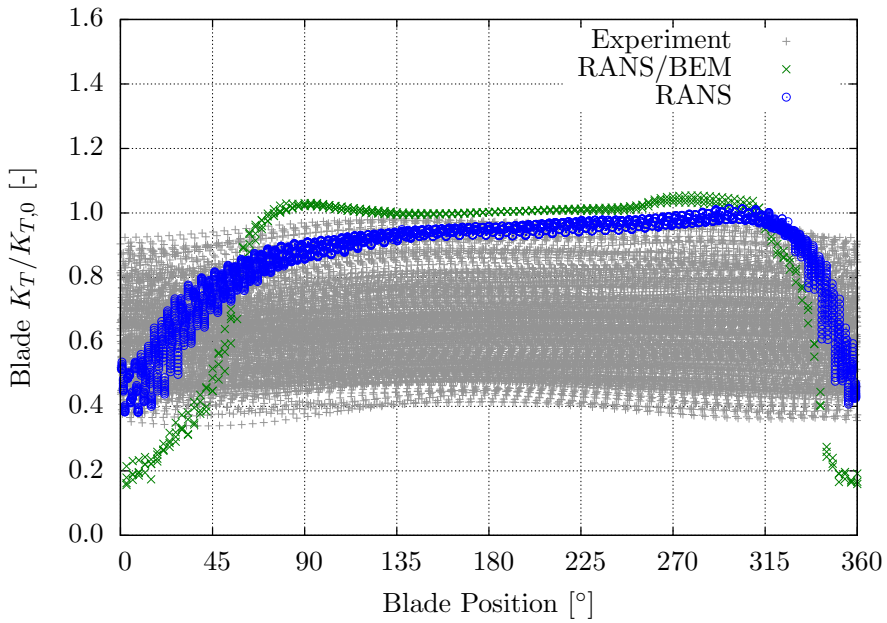

Figure 5.1.: Single blade loads for Propeller A (calm water, $H/R = 1.5, J = 0.15$)

In Figure 5.1, the single blade loads for $H/R = 1.5$ and $J = 0.15$ determined with the solver coupling method and the *RANSE* solver are presented and compared to the measured values. The experimental result refers to an *intermediate* case because the amplitude range is broad and no clear dependency of the thrust on the blade angle can be found. The *RANSE* results depict this intermediate behaviour well, but within every single blade rotation, while the thrust reaches $K_{T,0}$ for the lower and approx. $0.4K_{T,0}$ for the upper blade positions. This means a portion of the blade emerges out of the water in each rotation, but only a little amount of air is sucked downwards by the propeller and stays only a short period of time within the water. This results in a flat increase of thrust in the first half of the rotation compared to the steep decrease starting at 315°. Such an evolution of the thrust can also be found in the results obtained with the solver coupling method, where the force-extrema are more pronounced than in the *RANSE* results, which is an effect of the panel split technique, as explained above. Also, the increase of thrust after the topmost position is steeper in this case because the ventilated air content is not attached to the blade, which is not present. The general agreement between the *RANSE* results and those computed with the solver coupling method is good.

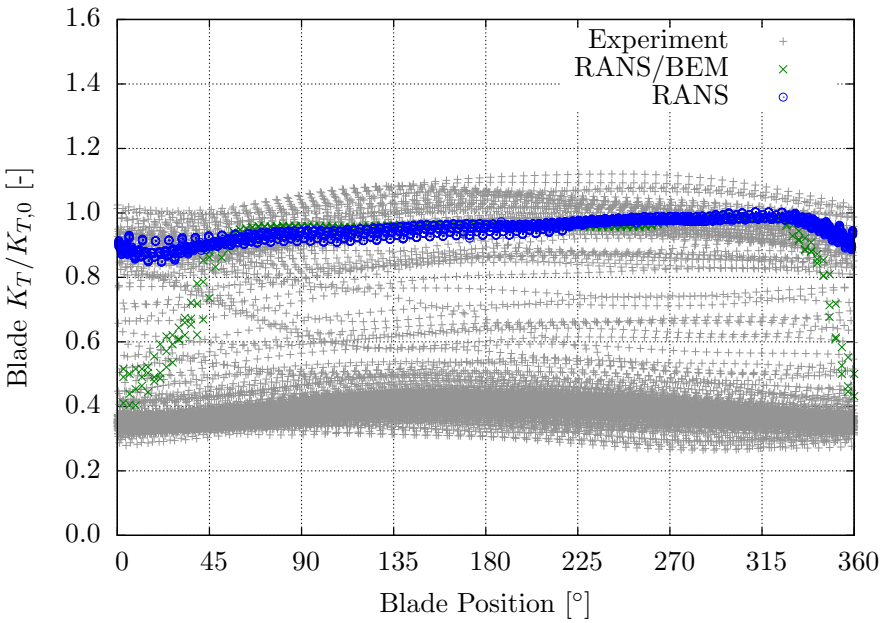

Figure 5.2.: Single blade loads for Propeller A (calm water, $H/R = 1.5, J = 0.3$)

In the results for $H/R = 1.5$ and $J = 0.3$, shown in Figure 5.2, significant differences between the methods and the experimental results become obvious. In the measurements, two main conditions are found, where the first is a non-ventilating case and the second is ventilating with a thrust value of approx. $0.4K_{T,0}$. The second condition dominates the first. Between 50° and 320° of a propeller rotation, the curves of the *RANSE* results and those computed with the solver coupling method perfectly match. For the blade at the topmost position, insignificant ventilation occurs in the *RANSE* simulations, while a strong thrust-decrease is found in the coupling results. The amplitude of the latter for one propeller rotation depicts, similar to $J = 0.15$ in Figure 5.1, the envelope of the measured results quite well. The angle at which the ventilation occurs agrees well between the two computational methods.

In Figure 5.3, *BEM* results are also given for comparison. The results are all similar, showing only little amounts of ventilation, referring to a situation with a free surface vortex. This case cannot be depicted well by the *BEM* and the results show the largest deviations from the experiments because a more pronounced wave trough occurs above the propeller position. Within the *BEM*, the free surface cannot form a vortical structure; only the blade can emerge out of the water with the panel split technique. The thrust fluctuations within the experimental and the other numerical results are very small compared to $K_{T,0}$, only minor free surface effects occur.

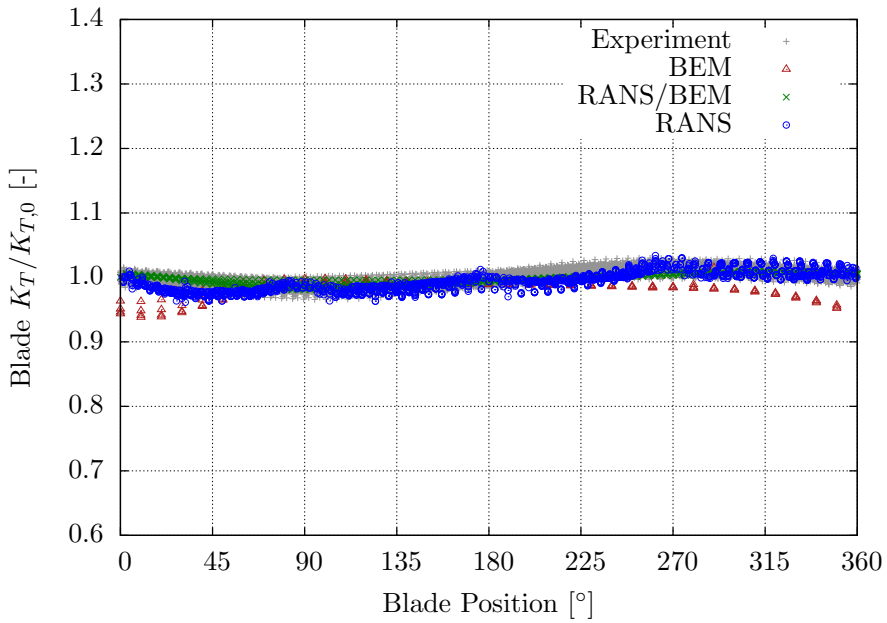

Figure 5.3.: Single blade loads for Propeller A (calm water, $H/R = 1.5, J = 0.6$)

A comparison between the free surface elevation and the air-volume-fraction in the computational domain of the *RANSE* part within simulations conducted with the solver coupling method is given in Figure 5.4 for $J = 0.15$ and $J = 0.6$. The cells containing propeller body-forces are coloured blue, so the geometry of the propeller and an impression of the *RANSE* grid is given. It can be seen that the finite volume grid is much coarser compared to typical *RANSE* simulations with geometrically resolved propeller. In Figure 5.4a, given for the higher thrust loading, a strong suction effect of the propeller on the water surface becomes obvious, so this is sucked downwards and the upper part of the blade emerges. In this part, no blade forces are transferred from the *BEM* to the *RANSE* domain because of the panel split technique as well as the free surface being present in the *BEM*. Because there is no geometry present in the *RANSE* domain, no air seems to be transported with the blades in rotation direction and the trough above the propeller is symmetrical. This also accounts for the $J = 0.6$-case in Figure 5.4b, in which the complete blade stays wetted due to smaller suction effect. The situation displayed in Figure 5.4 coincides with the thrust forces displayed in figures 5.1 and 5.3.

A comparison of numerical to experimental single blade thrust values for the different propeller loadings is given in Figures 5.5 to 5.8 for the solver coupling method and the *RANSE* solver at the propeller immersion ratio $H/R = 1.0$. In Figure 5.5, again the

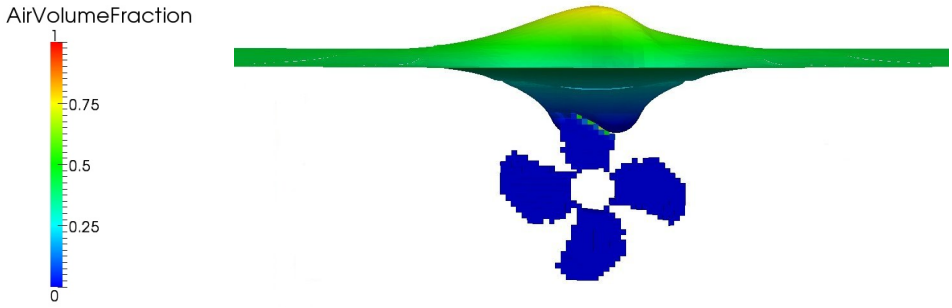

(a) $J = 0.15$

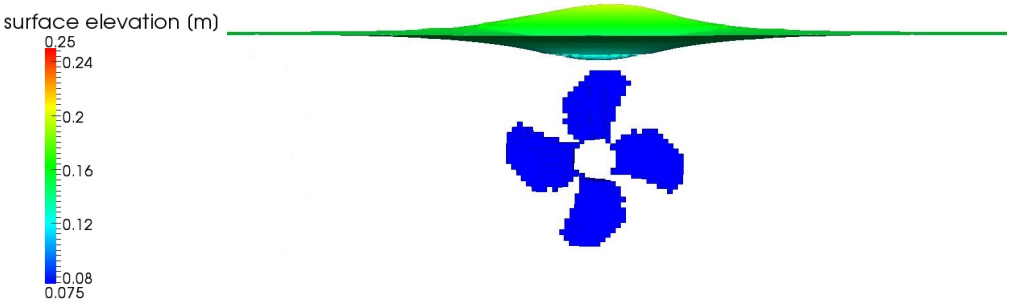

(b) $J = 0.6$

Figure 5.4.: Comparison of numerical results for free surface elevation and blade immersion at $H/R = 1.5$ and the blade at the topmost position

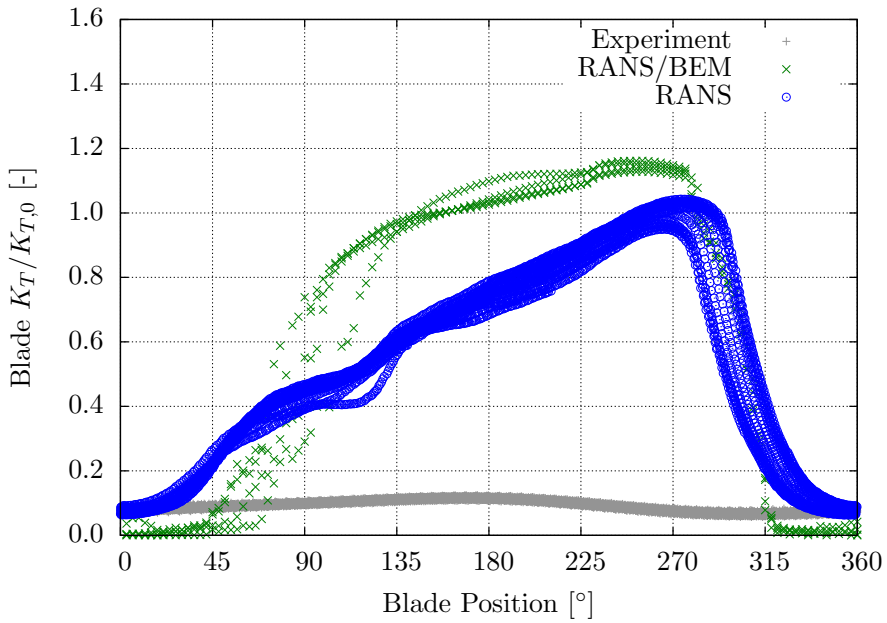

Figure 5.5.: Single blade loads for Propeller A (calm water, $H/R = 1.0, J = 0.15$)

computed thrust only depicts the measured values in the upper part of the propeller rotation. The simulation results clearly show an emerging event of the blade in every propeller rotation and a re-entrance, which can be quite abrupt (solver coupling method) or more smooth (*RANSE*). The experimentally determined thrust is nearly zero for all blade positions. So, the propeller operates in a fluid with high air-content in the experiment. A figure showing a similar situation is given later in Figure 5.15b. A significant effect is an overshoot of the computed thrust values after the re-entrance of the blade, which is more pronounced in the results computed by the solver coupling method. This is a possible cause of the panel split technique.

At the higher advance ratio $J = 0.3$, the propeller is again completely ventilating in the experiments, producing a thrust of approx. $0.1K_{T,0}$. This value is well predicted by both simulation methods when the blade is in the range between 330° and 30°. Apart of this, in the lower part of the rotation, the blade is fully wetted in the results of the computational methods and hence produces nearly the same amount of thrust compared to the deeply immersed case. The results of both simulation methods correlate for $J = 0.6$, as shown in Figure 5.7, except for the upright blade position, where the solver coupling method perfectly predicts the measured thrust, while the *RANSE* results are slightly above.

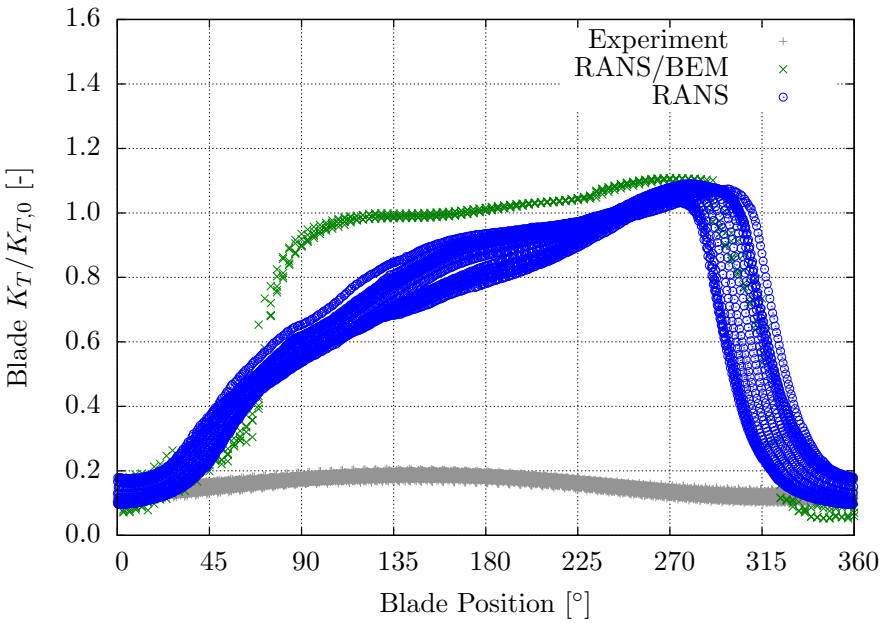

Figure 5.6.: Single blade loads for Propeller A (calm water, $H/R = 1.0, J = 0.3$)

In the simulations, the blade is fully wetted between 60° and 320° of the propeller revolution, whereas the propeller is fully ventilating for the complete rotation in the experiments and the thrust reaches approx. 30% of the deeply immersed value.

For $J = 0.9$, the propeller does not ventilate in the experiments and the thrust is near $K_{T,0}$ for the whole propeller rotation. This is also reproduced in the *RANSE* simulations, for which a small thrust increase can be found before the propeller emerges out of the water at about 310°, and a slightly lower thrust can be observed thereafter. This finding is confirmed by the experimentally determined forces, but is less pronounced than in the numerical results. A possible reason for this is a grid effect, due to the rotating cylindrical domain. In the results computed with the solver coupling method, ventilation events can be found for the blade between 340° and 40° and the single blade thrust reduces to $0.5K_{T,0}$ short after the topmost position. This situation is near or in the transition region from the ventilating to the non-ventilating case, which is confirmed by the results of the solver coupling method displayed in Figure 5.9b. Here, the water surface shows only small deformation because of the little amount of thrust produced by the propeller. This is significantly different in the results for $J = 0.15$ shown in Figure 5.9a, in which the free surface is highly deformed. In this case, the suction effect of the propeller blades transports a large portion of the water surface downwards in a non-symmetrical fashion to $\varphi \approx 135°$, which again matches well with

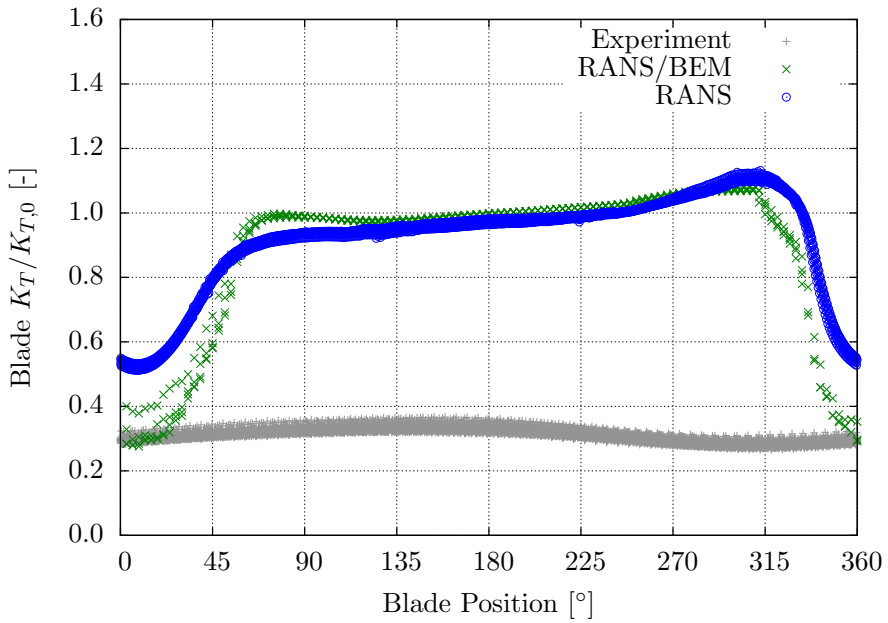

Figure 5.7.: Single blade loads for Propeller A (calm water, $H/R = 1.0, J = 0.6$)

the force-evolution displayed in Figure 5.5 where $K_{T,0}$ is reached at the same blade-angle. Because this case is challenging for the interface sharpening algorithm employed in the *RANSE* solver, some non-physical appearing wave crests can be observed above the still waterline. They are supposed to have a minor influence on the results.

At the immersion rate $H/R = 0.0$, extreme cases of ventilation can be observed in the force evolution plots given in Figures 5.10 to 5.12. Here, the blades are only immersed in the lower part of the rotation in the simulation results, while they ventilate over the whole rotation in case of the experiments, showing zero thrust in the upper part and 0.1 to $0.3K_{T,0}$ in the lower part of the revolution. In the latter, higher thrust values are computed by the simulation tools, especially by the solver coupling method, where $1.0K_{T,0}$ is attained for a short time-period around 180° for all propeller loadings. In the *RANSE* simulations, the trough in the water surface is more pronounced and the single blade thrust reaches values of $0.5K_{T,0}$, $0.6K_{T,0}$ and $1.0K_{T,0}$, respectively. The position where the blade emerges out of the water and immerses again is more or less at the initial free surface height, which is also the case in the experiments for $J = 0.15$. At smaller thrust loadings, the region showing zero-thrust becomes smaller and the blade seems to produce a small portion of thrust over the whole revolution at $J = 0.6$ in the experimental results.

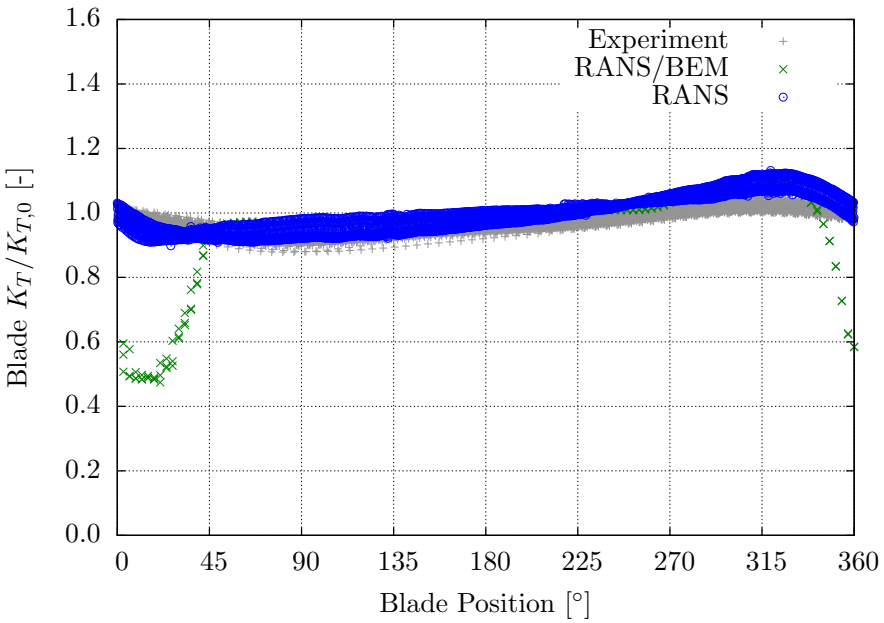

Figure 5.8.: Single blade loads for Propeller A (calm water, $H/R = 1.0, J = 0.9$)

A comparison of the computed free surface profile and the blade immersion determined in the *RANSE* domain of a simulation with the solver coupling method is given in Figure 5.13 for $J = 0.15$ and $J = 0.6$. As already found in the blade thrust results, the free surface trough above the propeller is small and approximately symmetrical for the latter case shown in Figure 5.13b, whereas for the high propeller loading the blade entrance to the water surface results in a more pronounced trough in Figure 5.13a.

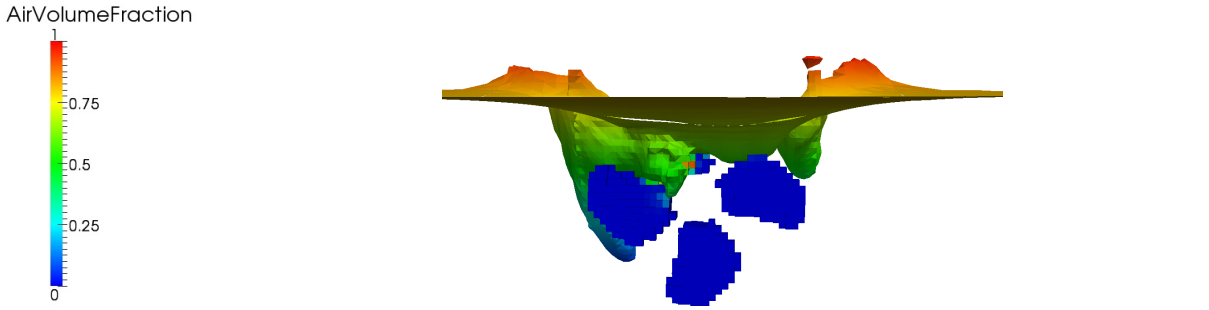

(a) $J = 0.15$

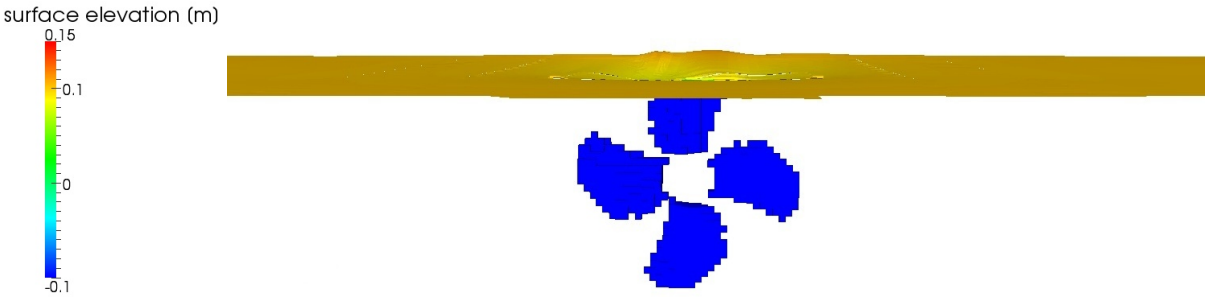

(b) $J = 0.9$

Figure 5.9.: Comparison of numerical results for free surface elevation and blade immersion at $H/R = 1.0$ and the blade at the topmost position

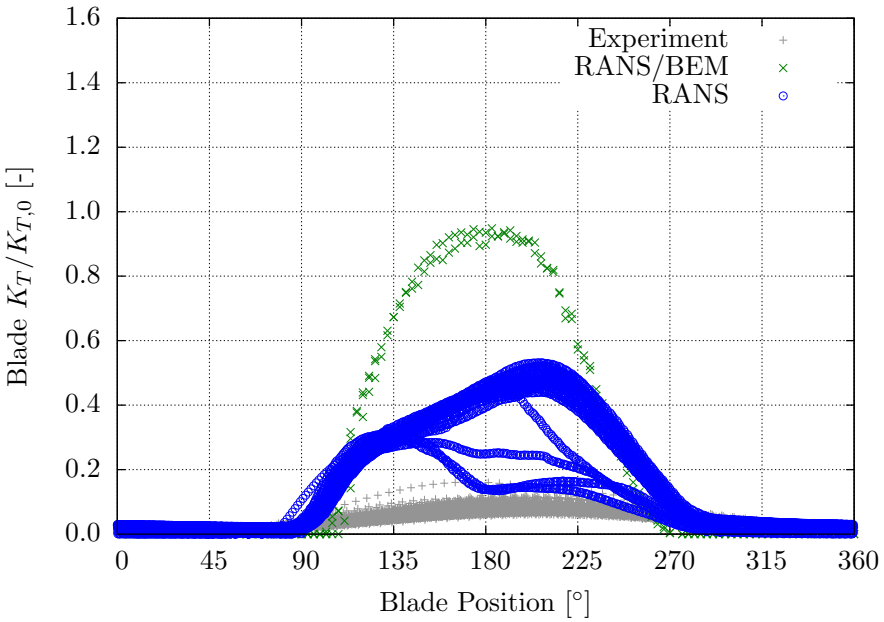

Figure 5.10.: Single blade loads for Propeller A (calm water, $H/R = 0.0, J = 0.15$)

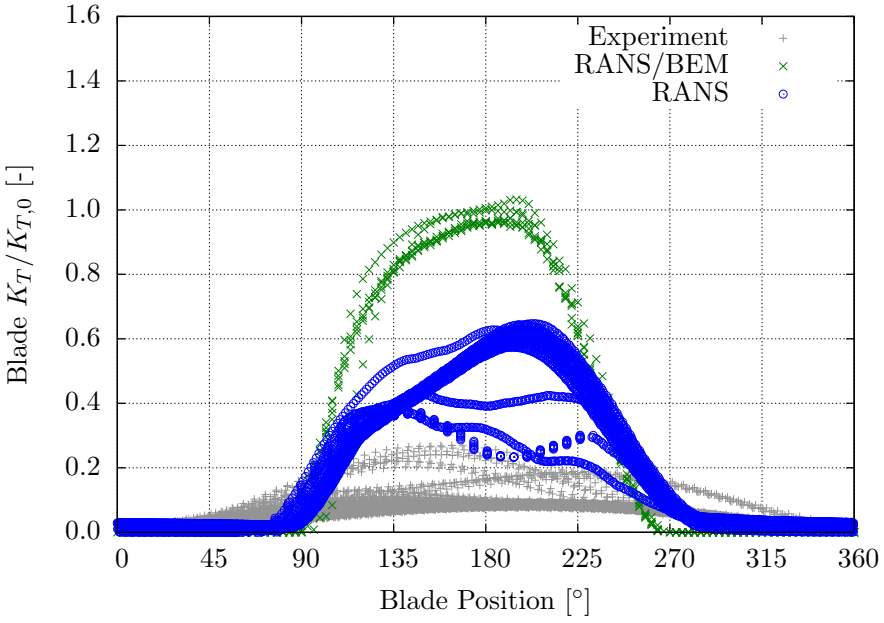

Figure 5.11.: Single blade loads for Propeller A (calm water, $H/R = 0.0, J = 0.3$)

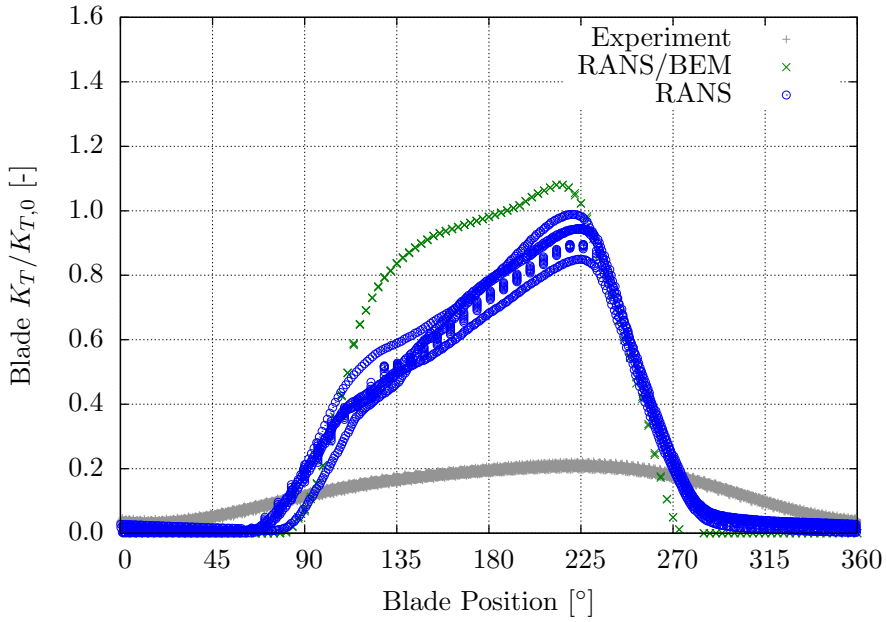

Figure 5.12.: Single blade loads for Propeller A (calm water, $H/R = 0.0, J = 0.6$)

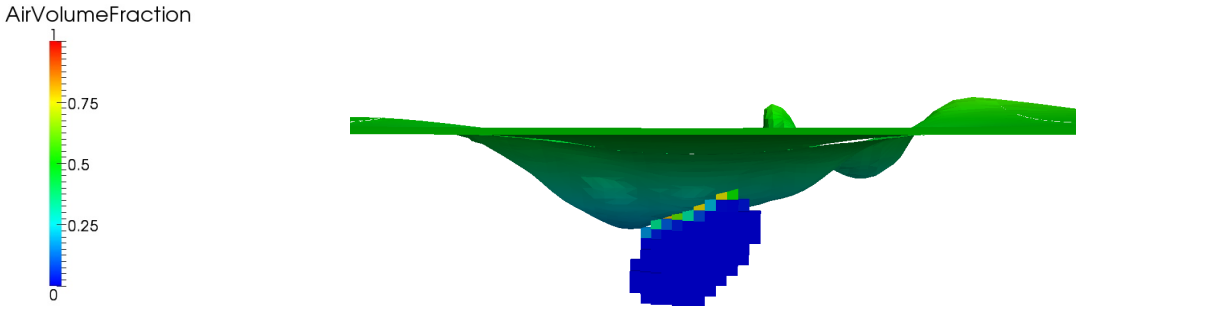

(a) $J = 0.15$

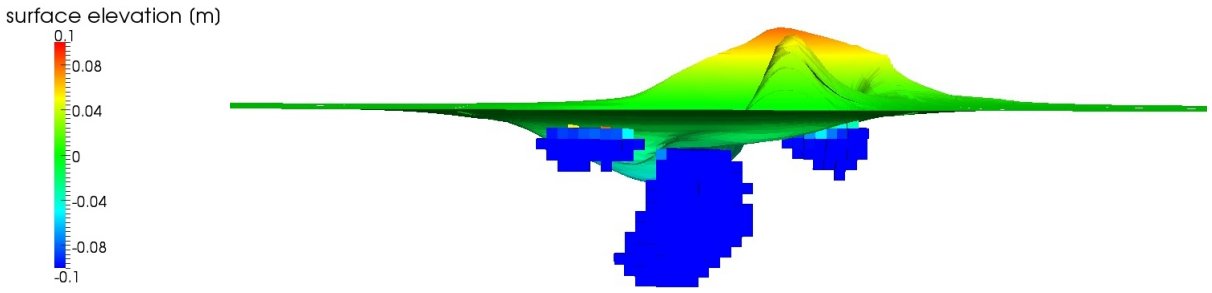

(b) $J = 0.6$

Figure 5.13.: Comparison of numerical results for free surface elevation and blade immersion at $H/R = 0.0$ and the blade at the topmost position

5.2. Propeller with Wave Influence and Varying Immersion

This section reports on a comparison of the unsteady wave loads acting on propeller blades in an open water situation between numerical simulations and experimental results. The simulations refer to the *BEM* with wave potential and panel split technique, which are conducted for three different waves, as shown in Table 5.2. The *BEM* grid has 16 x 24 panels per blade, the time step size refers to 6° of a propeller rotation, the wake length to 480° and it is deformed freely. For one case, simulation results obtained with the solver coupling method are also added for comparison. The experimental data is available for advance ratios $J = 0.3$, 0.6, 0.9 and 1.2, while the results for the latter are only given in Appendix C.1 and will not be discussed further in this context because the propeller loading and the open water thrust is small and this operating point is close to the feathering condition. For this reason, the free water surface influence is small and the agreement between the measured and computed *relative* thrust is of little significance.

Wave Code	Static Propeller Immersion $[mm]$	Wave Height $[mm]$	Wave Period $[s]$	Advance Ratio
8242	250	300	2.0	0.3 / 0.6 / 0.9 / 1.2
8211	100	100	1.5	0.6 / 0.9 / 1.2
8221	100	200	1.5	0.3 / 0.6 / 0.9 / 1.2

Table 5.2.: Overview of simulation cases for Propeller A subjected to a wave potential

In all of the following plots that show the normalised blade thrust for two seconds of real-time, two main frequencies become obvious. The first, higher frequency refers to the propeller blade frequency. The thrust alternates because of the different value of orbital velocities the blade is subjected to when it is in the down- or upmost position of one revolution. Even more pronounced is the influence of the vertically directed fractions of the orbital velocities, in particular at low propeller loadings. This can be seen e.g. in Figure 5.17, where the thrust fluctuations are smaller for the blade in a crest/trough-situation (at approx. $0.2s/0.75s$) than at the wave flanks (at approx. $0.45s/0.95s$). These effects are comparable to those occurring at a propeller operating in the wake field of a single-screw ship. The second, lower frequency, which can be seen in the following plots, is the encounter frequency between propeller and wave. The most significant effect of it is, that the blade shows more pronounced ventilation or emerging when subjected to a wave trough, which is the dominating finding in the results shown in Figure 5.22.

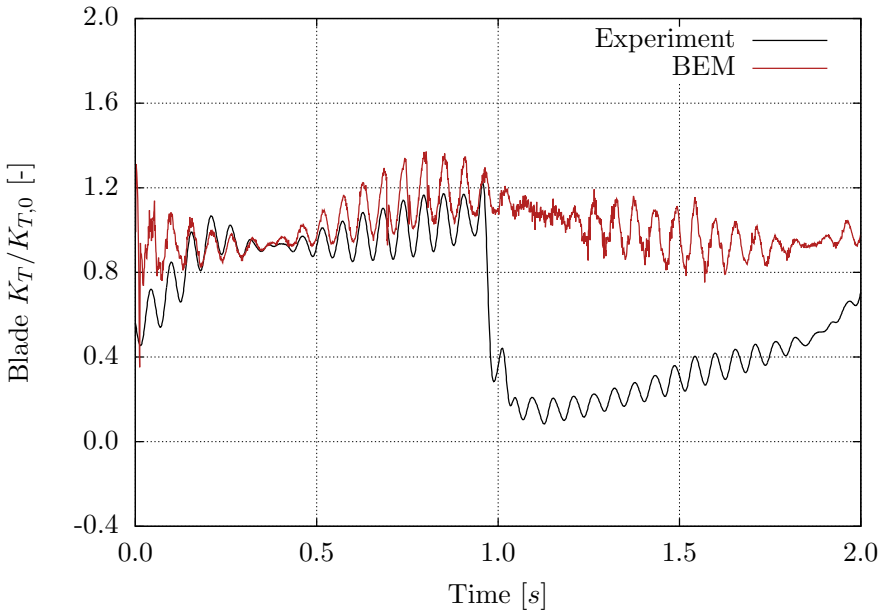

Figure 5.14.: Single blade loads for Propeller A
(wave 8242, $H/R = 2.5, J = 0.3, T_w = 2.0s, H_w = 0.3m$)

In the first series investigated, the propeller hub immersion is $0.25m$ and the wave 8242 is imposed. So, the clearance between the blade-tip and the undisturbed free water surface in a wave-trough-situation is *zero*. A comparison between the simulation and experimentally determined results is given in Figures 5.14, 5.16 and 5.17. The computed normalised blade thrust for the highest propeller loading presented in Figure 5.14 shows obvious differences compared to the measured data. When the propeller operates under a wave crest at approx. $0.4s$ and under the wave flank towards the trough, the agreement is satisfactory and the blade-frequency fluctuations show a similar amplitude. The mean value computed by the *BEM* is above the experimental results, though. An exemplary image of such a flow situation around the propeller taken from the *MARINTEK* experiments is shown in Figure 5.15a. Here, cavitating tip-vortices and a funnel-shape of the water surface above the propeller can be observed due to the suction effect. This image is typical for shallowly immersed propellers at moderate loads.

At the wave flank towards the wave trough, which is at approx. $1.0s$ of simulation time, a sudden and steep decrease of the blade thrust can be observed in the experimental results displayed Figure 5.14. This effect is due to ventilation, which is not represented in the numerical approach, although a reduction of the mean thrust can also be seen for

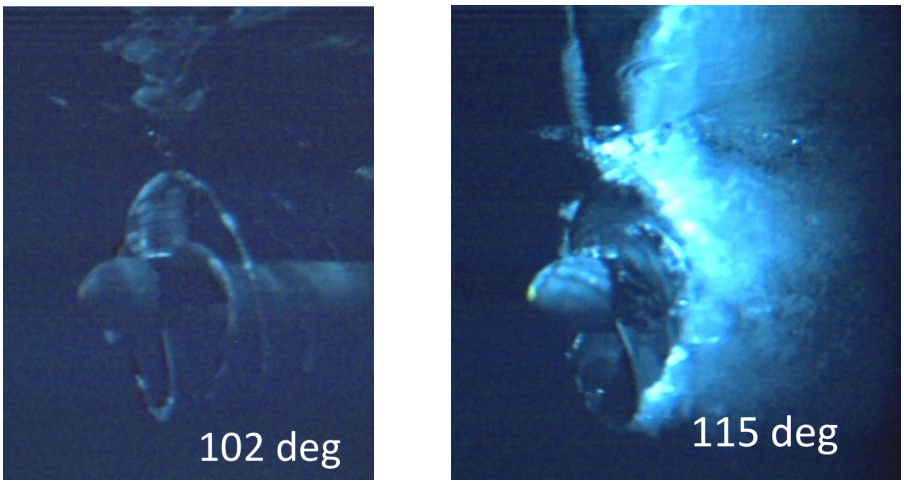

(a) Non-ventilating case (b) Fully ventilating case

Figure 5.15.: Exemplary images of the flow regime around the propeller in the *MARINTEK* experiments (published by Kozlowska et al. [62])

the simulation results but to a much smaller extent. In the experiment, the propeller experiences nearly *zero* thrust beneath a wave trough, although the time-instant at which the ventilation event occurs is not equal for each encounter peroid. The ventilated air content is kept within the water surrounding the propeller blade until short before the next wave crest. Due to the highly unsteady flow field, the thrust breakdown and the disappearance of ventilation happen at different stages for the different encounter periods, which are passed through in the experiment. A typical situation for which a thrust breakdown can be observed is presented in a picture taken from the *MARINTEK*-campaign in Figure 5.15b. In such cases, when significant ventilation occurs at the propeller, the thrust determined in the experiments suddenly breaks down.

When comparing the normalised single blade thrust for wave 8242 at a propeller advance ratio of $J = 0.6$ in Figure 5.16, a good agreement between simulation and experiment can be found. Due to the moderate blade loading, no ventilation seems to occur in the experiments and the mean thrust fluctuates in a narrow band around the thrust $K_{T,0}$ obtained for the deeply immersed propeller. The time-history of forces obtained in the experiments is somewhat angular and seems to be filtered, as already explained in Section 4.2.2 for a similar case. Here, the effect of the axially directed fractions of the wave orbital velocities is clearly visible. When the propeller operates under a wave crest, the fluctuations are small and the medium blade thrust is smaller than $K_{T,0}$ because the axial orbital velocity components are in line with the inflow velocity towards the propeller. This can be seen at approx. $0.25s$ and $1.5s$ of Figure 5.16 and it

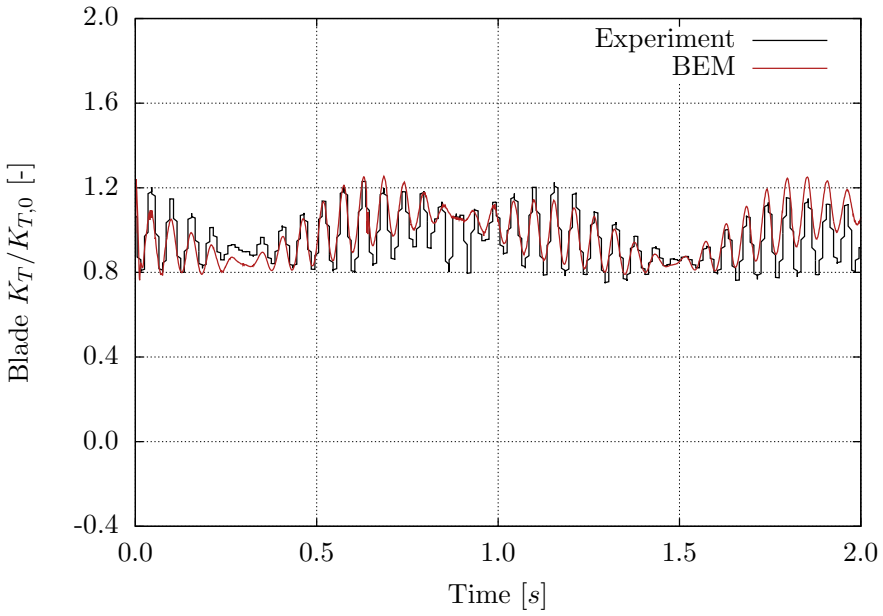

Figure 5.16.: Single blade loads for Propeller A
(wave 8242, $H/R = 2.5, J = 0.6, T_w = 2.0s, H_w = 0.3m$)

results in a *virtually* higher advance ratio. When the propeller is subjected to a wave trough (at approx. $0.85s$), the axial wave orbital velocities are directed against the propeller inflow and the *virtual* advance ratio is smaller, resulting in a larger thrust. Both situations are very well represented by the *BEM*, while smaller deviations can be seen in the wave-trough situation, where possible surface influences occur in the experiments.

In Figure 5.17, the results for wave 8242 and $J = 0.9$ are displayed. When taking into account that the absolute value of thrust for the deeply immersed propeller $K_{T,0}$ is low, the agreement of the relative thrust is surprisingly well between simulation and experiment. The effect of the axial component of the orbital velocities is depicted nicely, whereas smaller deviations occur at the wave flanks, where a large portion of the orbital velocities is directed vertically. This is explained above and is represented by the *BEM*, but is obviously delayed because both the amplitude of and the de-/increase in the forces follow those of the experimental results only from about half of the wave flank. In a crest-to-trough situation, the mean forces computed by the *BEM* are smaller compared to the measured forces, while they are larger in a trough-to-crest situation.

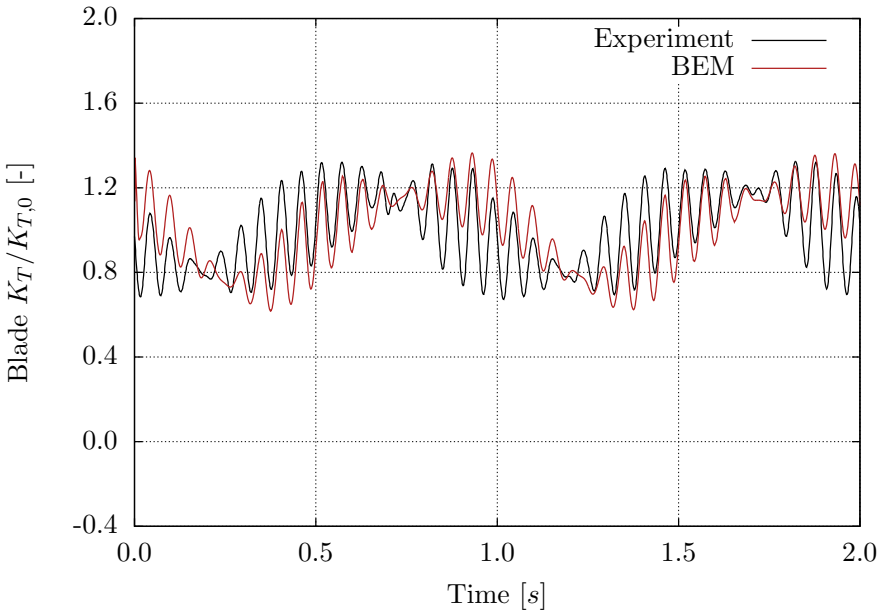

Figure 5.17.: Single blade loads for Propeller A
(wave 8242, $H/R = 2.5, J = 0.9, T_w = 2.0s, H_w = 0.3m$)

In the following cases, the propeller hub immersion is reduced to only one radius, so every wave trough leads automatically to emerging blades and to a ventilation event when the blade re-enters the free water surface. In Figures 5.18 and 5.19, the results are displayed for $J = 0.6$ and $J = 0.9$, respectively. In the first case, a similar trend like at $J = 0.3$ for wave 8242 (Figure 5.14) can be observed, but the measured thrust is in the range of $0.3K_{T,0}$ for the complete encounter period. Again, an air-water mixture as shown in Figure 5.15b is present around the propeller, which does not change significantly if under a wave crest or trough. In the simulation results, ventilation events can be observed when the blade is near a wave trough. When emerged, the blade thrust is zero and even below, which results from an overshoot noticed for the panel split technique. This overshoot can also be found in the opposite direction, when thrust values up to $1.3K_{T,0}$ are reached for the re-entering blade. The agreement is not satisfying in this case.

The results for the lower blade load at $J = 0.9$, are presented in Figure 5.19 and the agreement is again good, as single ventilation events can also be observed in the experimental results. The characteristics of the *BEM* results are nearly identical to $J = 0.6$, but those of the measurements are totally different. The thrust loss due to ventilation is a bit smaller in the experimental results and goes down to approx.

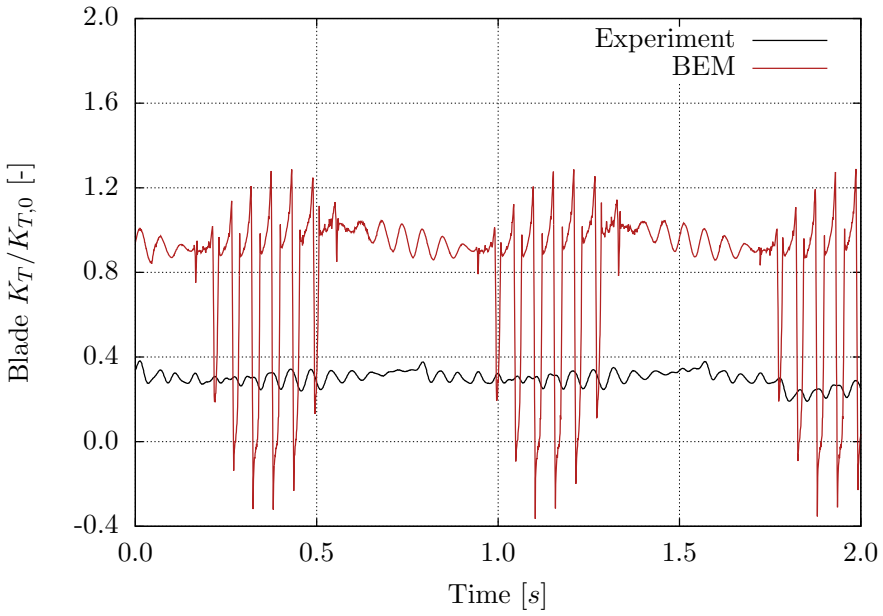

Figure 5.18.: Single blade loads for Propeller A
(wave 8211, $H/R = 1.0, J = 0.6, T_w = 1.5s, H_w = 0.1m$)

$0.1K_{T,0}$, whereas the simulations again show an overshoot down to approx. $-0.3K_{T,0}$. The trend and also the number of ventilation events is well predicted by the *BEM*.

In the last case shown here, comparisons are made for a propeller hub immersion of $H/R = 1.0$ and wave 8221 for the advance ratios $J = 0.3$, $J = 0.6$ and $J = 0.9$. For the highest propeller loading, simulations also using the solver coupling method are conducted and the results are presented in Figure 5.20. The comparison between experimental results and those obtained with the *BEM* shows similar differences to those observed in Figure 5.18. The measured normalised thrust coefficient for the propeller operating beneath a wave crest fluctuates in the range between *zero* and $0.2K_{T,0}$, while with the numerical methods it is about $K_{T,0}$. The thrust taken in the experiments shows a dependency on the wave position and is larger for the wave-crest situation. Due to the interaction between propeller and free water surface in the solver coupling results, the ventilation events occur earlier than those in the *BEM*. This can be seen at $0.25s$ and $1.25s$ of the time-history. The effect is depicted in Figure 5.21 for a better understanding. The pictures refer to snapshots taken from the *RANSE* simulation domain at different time-instants during one encounter period from a simulation using the solver coupling method. The situation discussed is depicted in Figure 5.21d, where a significant suction effect resulting in a lowering of the free surface

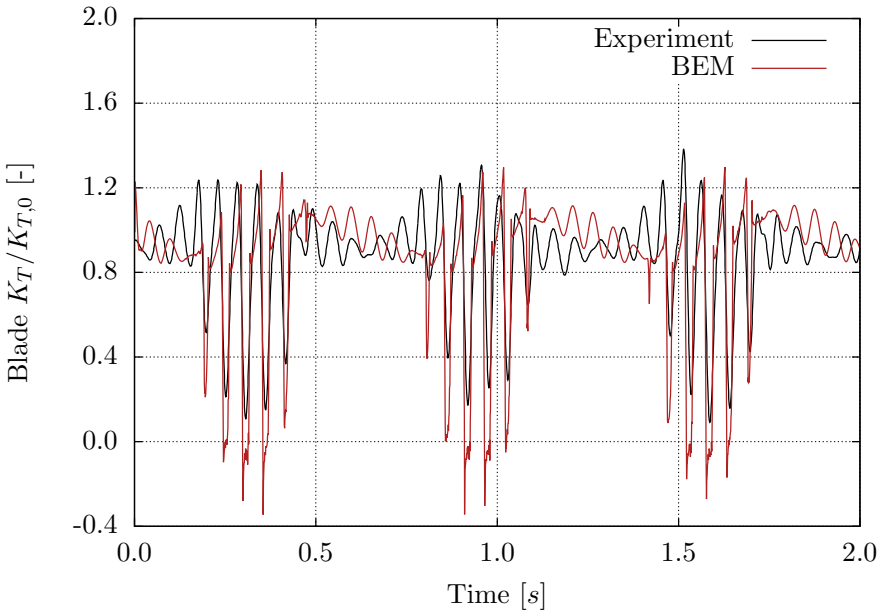

Figure 5.19.: Single blade loads for Propeller A
(wave 8211, $H/R = 1.0, J = 0.9, T_w = 1.5s, H_w = 0.1m$)

above the propeller is visible. A pronounced interaction is also visible for the other time-instants. The suction effect can be seen in Figure 5.21a in line with effects leading to a higher elevation aft of the propeller. Figure 5.21b refers to the situation at $0.75s$, where the ventilated air-content is still present in the water but soon vanishes due to the rising free water surface. This flow situation, characterised by a pronounced ventilation regime, is more stable in the experimental results.

In Figure 5.20, an overshoot, as observed in the *BEM* results, is not present in the solver coupling results. When the blade does not ventilate, at approx. $1.0s$ of simulation time, the fluctuations around $K_{T,0}$ show a different behaviour between the solver coupling method and the *BEM*, having different frequencies. This could be due to a pronounced interaction between the blade, the wave orbital velocities and the free water surface.

The results for $J = 0.6$ and wave 8221 are displayed in Figure 5.22. Here, the agreement is good, showing ventilation events in both the experimental and the numerical results. The number of those events is about the same, but the ventilated air regime seems to stay longer around the propeller in the experiment. This can be explained by the unsteady interaction with the free surface due to the propeller suction effect. The experimentally determined forces are not periodic, which is a measure for the pronounced unsteadiness of the cases investigated here. When focusing on the wave-crest area, only

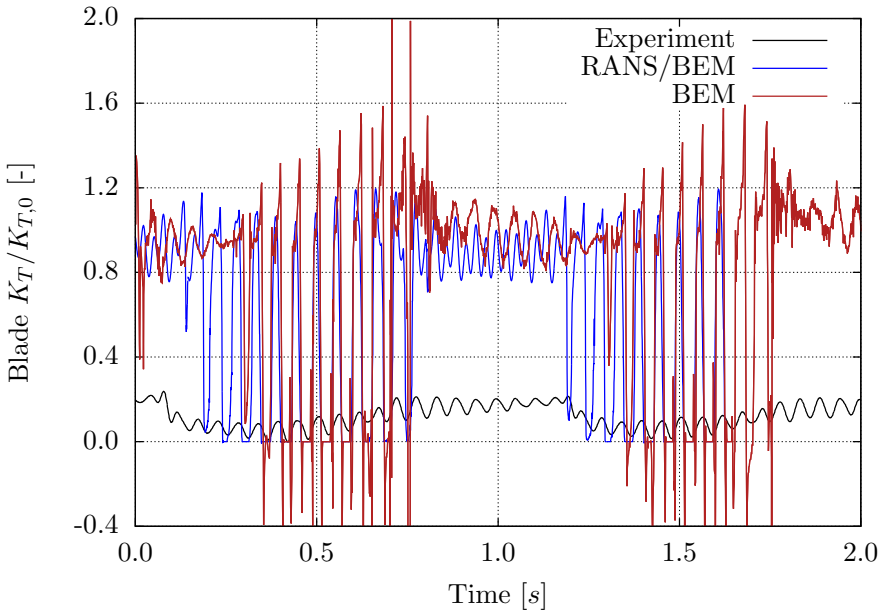

Figure 5.20.: Single blade loads for Propeller A
(wave 8221, $H/R = 1.0, J = 0.3, T_w = 1.5s, H_w = 0.2m$)

a small time-instant at approx. $0.7s$ and $1.45s$ can be found, where the amplitudes and frequencies between the *BEM* results and the experiments match. Besides this time-instant, the interaction between propeller and free water surface is large, which cannot be depicted by the *BEM* computations[1]. Similar findings can be made in Figure 5.23 for the same wave at an advance ratio of $J = 0.9$. Here, due to the smaller absolute thrust value, the overshoot in the *BEM* results is even more pronounced, resulting in normalised blade loads between $-0.5K_{T,0}$ and $1.8K_{T,0}$.

[1] This is a possible explanation for the differences observed in Figure 5.20 between the solver coupling method and the *BEM*.

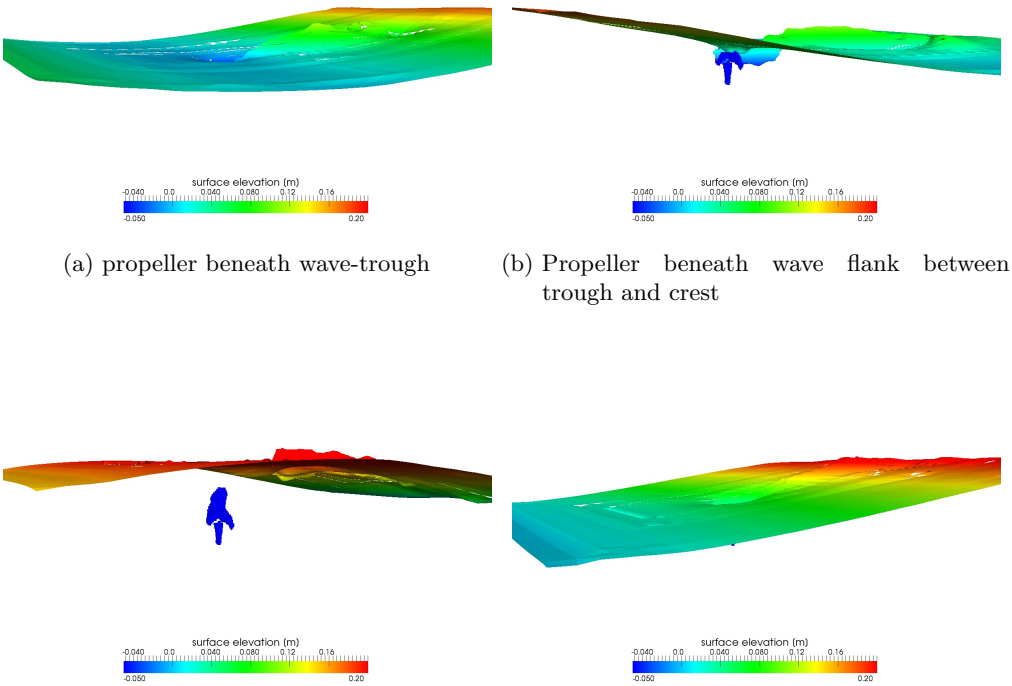

(a) propeller beneath wave-trough

(b) Propeller beneath wave flank between trough and crest

(c) Propeller beneath wave-crest

(d) Propeller beneath wave flank between crest and trough

Figure 5.21.: Volumetric propeller forces (blue) and free water surface elevation for different time-instants during one encounter period computed with the solver coupling method

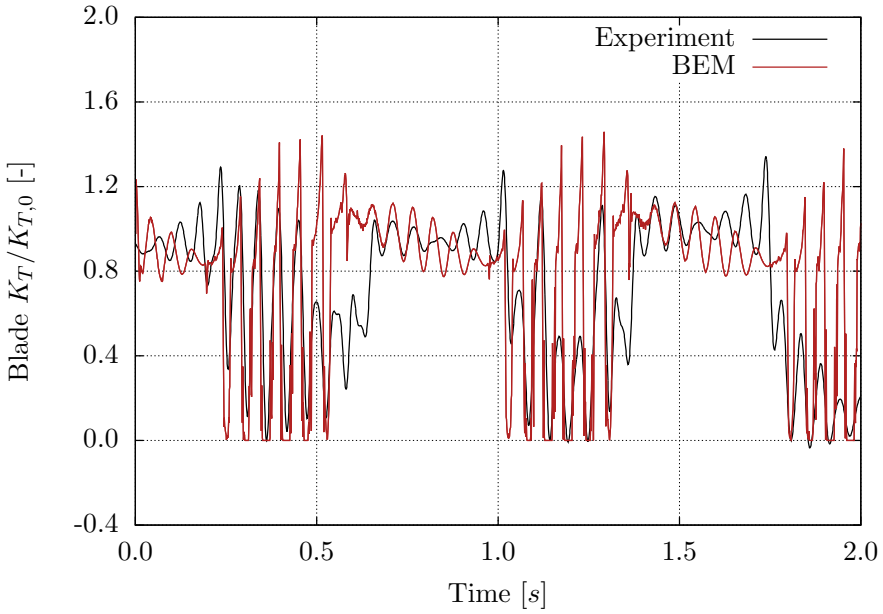

Figure 5.22.: Single blade loads for Propeller A
(wave 8221, $H/R = 1.0, J = 0.6, T_w = 1.5s, H_w = 0.2m$)

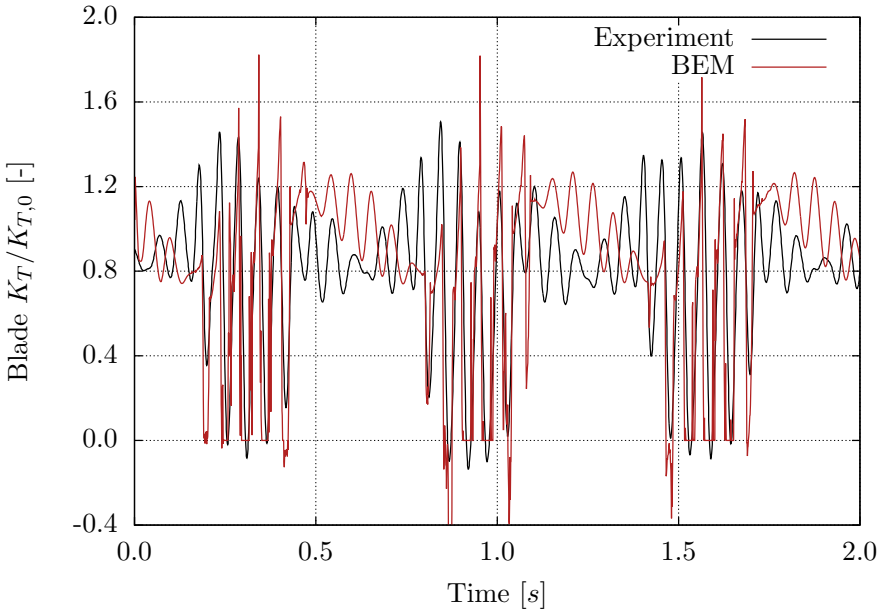

Figure 5.23.: Single blade loads for Propeller A
(wave 8221, $H/R = 1.0, J = 0.9, T_w = 1.5s, H_w = 0.2m$)

5.3. Discussion and Conclusions

In Chapter 5, application examples for the developed numerical methods are given. The first in 5.1 refers to a shallowly immersed propeller in an open water setup. Most of the results are computed with the solver coupling method, but also some with the *BEM*. A comparison of the normalised blade forces for several propeller rotations is given towards experimentally determined values. The *BEM* results refer to the propeller having the largest immersion ratio of $H/R = 1.5$, where the interaction between propeller and free water surface is less noticeable. For smaller H/R-ratios, a strong smoothing would have to be applied at the water surface, leading to a violation of the b.c.. This is discarded because a flow field showing a small-scale mixture of air and water and often pronounced vortex structures cannot be regarded as a potential flow field. Also, the intermediate state defined by Califano [16], where a vortex tube develops from the free water surface towards the blade tip, cannot be reproduced by *BEM* simulations. In the simulations, numerical instabilities occur, when the end of the discretised part of the wake sheet interferes with the free surface. To prevent this, the water surface is only modelled up to a position shortly behind the propeller and the wake surfaces extend further. The position up to which the water is discretised depends on the advance ratio.

The described shortcomings do not account for the solver coupling method, which makes a simulation of propeller ventilation possible. The computational effort is manageable compared to *RANSE* simulations and several propeller revolutions can be simulated in a few hours of simulation time. When a blade is wetted for most of the revolution and emerges only in the upper part of the rotation, the agreement towards the measured thrust characteristics is satisfying. This flow situation is presumably dominating for most of the ventilation events occurring at a propeller at an ocean going ship. Moreover, the dynamic load fluctuations in this case are supposed to be higher than for a completely ventilating propeller. When the propeller load is high and the immersion is small, pronounced ventilation occurs and the course of thrust force obtained in the model-scale experiments is constant with a value well below $K_{T,0}$. This situation is neither computed correctly with the solver coupling method, nor with the *RANSE* solver.

A comparison between the free surface elevation computed by the solver coupling method and the *RANSE* solver is given in Figure 5.24 for an immersion ratio of $H/R = 1.5$ and $J = 0.15$. A significant difference is the height of the water surface elevation in front of the propeller. In the *RANSE* simulations, the wave crest results from the rotating grid approach described by Wöckner-Kluwe [98]. The whole numerical grid is rotated with the propeller in order to capture more of the ventilation phenomena, which is an approach similar to the rotating cylinder connected via sliding mesh with a surrounding stationary grid used by Califano [16]. In case of the

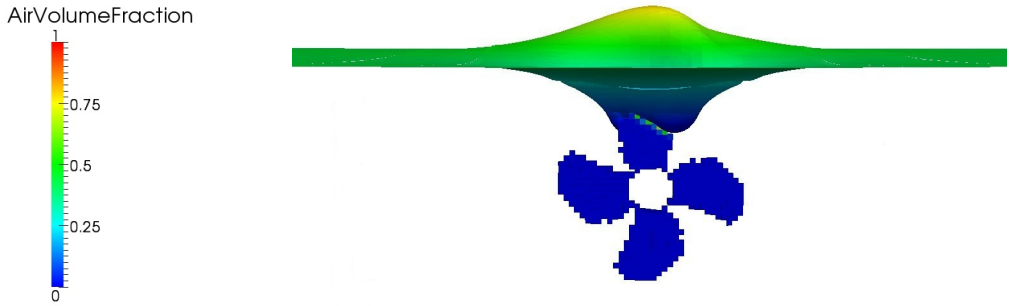

(a) Results of the solver coupling method

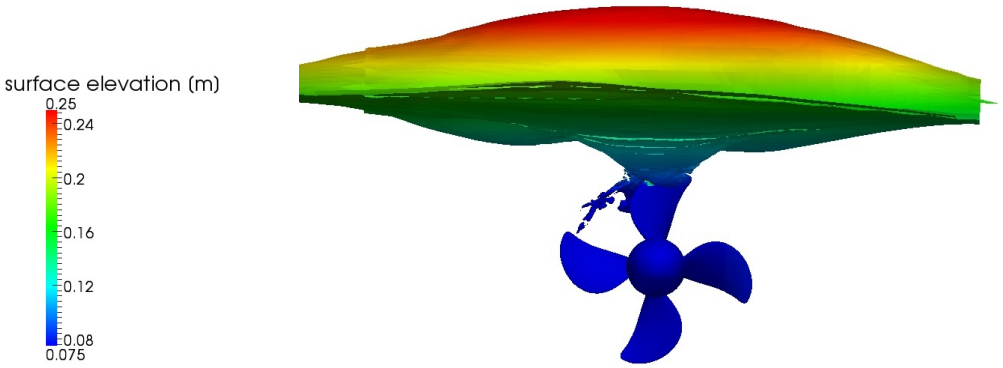

(b) *RANSE* results

Figure 5.24.: Comparison of numerical results for free surface elevation and blade immersion at $H/R = 1.5$, and $J = 0.15$ and the blade at the topmost position

solver coupling method, the numerical grid identifiable from the body forces displayed in Figure 5.24a is not moving because the force field is moving. It is much coarser than the *RANSE* simulations in Figure 5.24b, as the body does not have to be resolved and a selective refinement in the free surface region can be made. The *RANSE* grids are perfectly rectangular in the cases computed with the solver coupling method. In the simulation results, the wave trough directly above the propeller is similar when comparing both methods. The crest is slightly deeper and unsymmetrical in the results obtained with the solver coupling method, an effect maybe resulting from the panel split technique inherited here. The body force representation of the propeller can obviously not suck portions of air into the water, which can be seen for the geometrically modelled propeller in the lower picture. This ventilated air content is considerably lower than in the pictures taken from the experiments.

The above findings in the results computed with both *RANSE*-based methods are similar to those described by Califano [16] (sec. 5.2f), who made several attempts in under-

relaxing the equations used in the *RANSE* solver. The results show a large dependency of the ventilation patterns on the numerical parameters and unstable simulations are reported. This does not account for the solver coupling method used here, which leads to an overestimation of the forces, as also found by Califano.

Both numerical methods compared here to the experimental results depict the maximum thrust breakdown well and the amplitude of the single blade thrust signal could be further used for simulating the mechanical loads and deformations of the propeller blades. A question not addressed in this investigation is weather the results can be easily transferred to full-scale propellers. This accounts also for the model scale test results. A numerical investigation on scale effects is given by Wöckner-Kluwe [98], in which problems are left unsolved.

In 5.2, the influence of waves and a varying propeller immersion on the single blade loads is investigated for several propeller revolutions and for more than one encounter period between propeller and wave. A single comparison is given for the solver coupling method, while all other simulations are conducted with the *BEM* because the simulation effort is excessive in case of the *RANSE*-based simulations. The results can be divided in three parts. When the propeller does not ventilate, the unsteady forces nearly perfectly match between the simulated and measured data. The thrust fluctuations and the different behaviour under a wave flank or a crest/trough can be depicted well by the *BEM*. When the propeller is fully ventilating and the thrust is a lot smaller than $K_{T,0}$ for the whole simulation, the forces cannot be computed correctly with the *BEM* because of the reasons discussed above. Here, the strong ventilation in combination with possible cavitation acts similar to a reduction of the fluid density. This is a possible starting point for future numerical developments and it cannot be solved with the current method, as the interface between water and air is always sharp and the density is constant. Another approach would be a modification of the panel split technique in a way that all panels subjected to a ventilating flow regime could be assigned a *split factor* smaller than one. The simulations can reproduce the propeller ventilating due to a wave trough and the thrust fluctuations show an acceptable agreement towards the measurements.

One factor complicating a comparison between numerical and experimental results is the pronounced unsteady behaviour of the forces in the measurements. The *bubbly flow* can be around the propeller for quite a while, even for several encounter periods, and suddenly disappear - an effect, hardly to be simulated with a numerical method. These effects can originate from the non-reproducible towing-tank environment and are certainly due to the unsteady flow situation. This refers to the unstable transition region from either non-ventilating or partially ventilating cases to the fully ventilating condition, as described by Califano [16] (sec. 2.4). One time-history of forces is about 15 to 20s long and the course is sometimes altering between different conditions. In some

cases, the experimental results can be questionable, e.g. for wave 8221 and $J = 0.6$, the propeller only partly ventilates, whereas for 8211 and $J = 0.6$, it is completely ventilating, although the second wave is more shallow.

Finally, it should be noted that the solver coupling method can be used in order to capture details of the flow field around propellers and a strong interaction between propeller and free water surface is possible. However, the ventilated air-content cannot be sustained in the water in *RANSE*-based simulations (the *RANSE* and the solver coupling method simulations) because the bubbles or a tube towards the water surface are never established in contrast to in the experiments and furthermore vanish due to a free surface-sharpening by the *VoF*-model. When computing wave-influences, the simulation time of the solver coupling method is too large and the *BEM* in combination with a wave potential is used. The results are satisfying for cases with low to moderate thrust loadings and $J >= 0.6$, even when the blades significantly emerge out of the water. For higher loadings or an extreme low propeller immersion, the agreement to the experimental data becomes worse.

6. Conclusions

This thesis reports on the development of two methods for simulating propellers in the vicinity of a free water surface. They refer to a Boundary Element Method, in which boundary conditions are integrated and to a solver coupling method to a *RANSE* method, for which the *BEM*-part is modelled.

The solution of the flow problem using a *BEM* is explained and the equations are derived. This includes different treatment of the free surface boundary conditions in case of a steady and an unsteady simulation. In the steady case, both boundary conditions are combined and solved in the equation system. A six point upwind differencing scheme is used requiring a specified dominating flow direction and resulting in a fast convergence behaviour. The free surface elevation is determined after solving the equation system. In the unsteady case, both boundary conditions are treated separately. The kinematic boundary condition is solved in the *SLE* and the dynamic is determined in line with the free surface elevation using a time-stepping scheme. For implementing the solver coupling method, an interface for the transfer of physical quantities, mainly the viscous velocity distribution and the potential based propeller forces, is developed in the *BEM*.

An in-depth validation and verification of the numerical methods is undertaken in Chapter 4, separately addressing the different physical effects occurring at an operating propeller. Grid studies are given for the different geometries showing the geometrical convergence of the method. Results are evaluated for hydrofoils and propellers in undisturbed inflow computed by the *BEM* and the solver coupling method. A validation towards the computed lift forces and the pressure distribution is presented for a hydrofoil and towards the open water data for two propellers. For the solver coupling method, a verification study on determining the induced velocities computed by both involved solvers is given in order to test the accuracy of the solution strategy. The dynamic loads are validated using experimental data from *MARINTEK*, for propellers operating in oblique flow conditions and in waves. The results obtained with the *BEM* and the solver coupling method are satisfying for an oblique inflow up to 10°. Above this value, further improvements are necessary, in order to determine loads acting on propulsors of ships operating in harsh weather conditions, leading to pronounced ship motions. The third part of the validation is devoted to an investigation of the interaction between bodies and a free water surface. It starts with simulations of a two-dimensional

hydrofoil under a free surface, and gives a comparison of the wave drag of spheroids and the propeller blade thrust breakdown when subjected to a shallow immersion. The validation shows very good results for the grid convergence and the forces computed by the baseline program. Also, the wave drag and the wave profile for submerged bodies are computed accurately.

The application chapter reports on two large simulation campaigns with shallowly immersed propellers operating under free surface influence. The first refers to a propeller in calm water with different immersion and thrust loading, for which the normalised single blade thrust forces are determined, plotted over the blade angle and compared to measured values. The results mainly computed with the solver coupling method show a good accordance to the experimental results for cases with small free surface influence. For the propeller subjected to significant ventilation, the characteristics of the thrust curves show differences, while the amplitude of thrust losses can be captured well by the algorithm. For an immersion at which the hub is located at the undisturbed free surface position, the curves become more similar but the forces computed are still above those taken from the experiments. The results obtained with the solver coupling method show a good agreement to the *RANSE* data; although losing some of the details, it reproduces the trend with a massive reduction in simulation time. The solver coupling method shows a numerically robust behaviour. This fact makes it possible to perform even long simulations, such as several encounter periods for a propeller operating in waves. Nevertheless, most of these simulations are undertaken in the second part of the application chapter using the *BEM*, due to a significantly shorter simulation time. The results again show a very good agreement to experimental values for cases with negligible ventilation. Also, the computed thrust forces for partly ventilating conditions under a wave trough are determined showing only minor deviations to the measured data. When the propeller is completely ventilating under a wave crest, the nearly total thrust loss cannot be captured with the simulations.

The forces for propellers operating in waves and with shallow immersion, which are computed with the methods developed in this thesis, can be regarded as reliable and can be used in a design process of the different parts of the propulsion system. Future work could be related to more accurately predict the loads on strongly ventilating propellers. In order to do this, the panel split technique could be enhanced in a way that the numerical grid is adapted to the local geometry of the body and the deformed free water surface. With a grid adaption, non-vertical panels on a body piercing the free surface could be accounted for and also the simulation results for highly loadad propellers in the vicinity of the free water surface could be improved. Also, a numerical damping could be implemented in order to reduce the observed overshoots in the unsteady forces for a re-entering blade. Furthermore, methods could be developed that supress the strong interaction between the free water surface and the propeller wake, which would result in stable simulations at shallow immersion.

Future developments can also be related to the prediction of the wave resistance of ships or submarines. Therefore, a non-linear stationary formulation of the free surface boundary conditions could be implemented. With the developed methods described in this thesis, also propellers and rudders could be included in such simulations.

A. Computational Model

A.1. Panel Influence Functions for a Source Distribution

The potential induced by a constant strength source panel is composed of four parts:

$$\begin{aligned}\phi_S =& \frac{-\sigma}{4\pi}\left[\frac{(\xi-\xi_0)(\eta_1-\eta_0)-(\eta-\eta_0)(\xi_1-\xi_0)}{d_{01}} ln\frac{r_0+r_1+d_{01}}{r_0+r_1-d_{01}}\right.\\ &+\frac{(\xi-\xi_1)(\eta_2-\eta_1)-(\eta-\eta_1)(\xi_2-\xi_1)}{d_{12}} ln\frac{r_1+r_2+d_{12}}{r_1+r_2-d_{12}}\\ &+\frac{(\xi-\xi_2)(\eta_3-\eta_2)-(\eta-\eta_2)(\xi_3-\xi_2)}{d_{23}} ln\frac{r_2+r_3+d_{23}}{r_2+r_3-d_{23}}\\ &\left.+\frac{(\xi-\xi_3)(\eta_0-\eta_3)-(\eta-\eta_3)(\xi_0-\xi_3)}{d_{30}} ln\frac{r_3+r_0+d_{30}}{r_3+r_0-d_{30}}\right]\\ &-\frac{\sigma}{4\pi}|\psi|\left[tan^{-1}\left(\frac{m_{01}e_0-h_0}{\psi r_0}\right)-tan^{-1}\left(\frac{m_{01}e_1-h_1}{\psi r_1}\right)\right.\\ &+tan^{-1}\left(\frac{m_{12}e_1-h_1}{\psi r_1}\right)-tan^{-1}\left(\frac{m_{12}e_2-h_2}{\psi r_2}\right)\\ &+tan^{-1}\left(\frac{m_{23}e_2-h_2}{\psi r_2}\right)-tan^{-1}\left(\frac{m_{23}e_3-h_3}{\psi r_3}\right)\\ &\left.+tan^{-1}\left(\frac{m_{30}e_3-h_3}{\psi r_3}\right)-tan^{-1}\left(\frac{m_{30}e_0-h_0}{\psi r_0}\right)\right],\end{aligned} \tag{A.1}$$

using the corner coordinates $P_i(\xi_i, \eta_i, \psi_i)$ for $i \in [0;3]$ and the distances from P to the corners r_i. The variables e_i and h_i refer to projected distances and they read

$$r_i = \sqrt{(\xi-\xi_i)^2+(\eta-\eta_i)^2+\psi^2}, \tag{A.2}$$

$$e_i = (\xi-\xi_i)^2+\psi^2, \tag{A.3}$$

$$h_i = (\xi-\xi_i)+(\eta-\eta_i). \tag{A.4}$$

The edge quantities used in Equation (A.1) are the edge length $d_{(i)(i+1)}$ and the local edge direction $m_{(i)(i+1)}$ for the edge i between the corners i and $i+1$

$$d_{(i)(i+1)} = \sqrt{(\xi_{i+1} - \xi_i)^2 + (\eta_{i+1} - \eta_i)^2}, \tag{A.5}$$

$$m_{(i)(i+1)} = \frac{\eta_{i+1} - \eta_i}{\xi_{i+1} - \xi_i}. \tag{A.6}$$

The velocity components induced by the panel are derived by differentiating the velocity potential in the three coordinate directions read

$$\begin{aligned} u_S = \frac{\sigma}{4\pi} \Bigg[& \frac{\eta_1 - \eta_0}{d_{01}} ln \frac{r_0 + r_1 - d_{01}}{r_0 + r_1 + d_{01}} + \frac{\eta_2 - \eta_1}{d_{12}} ln \frac{r_1 + r_2 - d_{12}}{r_1 + r_2 + d_{12}} \\ & + \frac{\eta_3 - \eta_2}{d_{23}} ln \frac{r_2 + r_3 - d_{23}}{r_2 + r_3 + d_{23}} + \frac{\eta_0 - \eta_3}{d_{30}} ln \frac{r_3 + r_0 - d_{30}}{r_3 + r_0 + d_{30}} \Bigg], \end{aligned} \tag{A.7}$$

$$\begin{aligned} v_S = \frac{\sigma}{4\pi} \Bigg[& \frac{\xi_0 - \xi_1}{d_{01}} ln \frac{r_0 + r_1 - d_{01}}{r_0 + r_1 + d_{01}} + \frac{\xi_1 - \xi_2}{d_{12}} ln \frac{r_1 + r_2 - d_{12}}{r_1 + r_2 + d_{12}} \\ & + \frac{\xi_2 - \xi_3}{d_{23}} ln \frac{r_2 + r_3 - d_{23}}{r_2 + r_3 + d_{23}} + \frac{\xi_3 - \xi_0}{d_{30}} ln \frac{r_3 + r_0 - d_{30}}{r_3 + r_0 + d_{30}} \Bigg], \end{aligned} \tag{A.8}$$

$$\begin{aligned} w_S = \frac{\sigma}{4\pi} \Bigg[& tan^{-1} \left(\frac{m_{01} e_0 - h_0}{\psi r_0} \right) - tan^{-1} \left(\frac{m_{01} e_1 - h_1}{\psi r_1} \right) \\ & + tan^{-1} \left(\frac{m_{12} e_1 - h_1}{\psi r_1} \right) - tan^{-1} \left(\frac{m_{12} e_2 - h_2}{\psi r_2} \right) \\ & + tan^{-1} \left(\frac{m_{23} e_2 - h_2}{\psi r_2} \right) - tan^{-1} \left(\frac{m_{23} e_3 - h_3}{\psi r_3} \right) \\ & + tan^{-1} \left(\frac{m_{30} e_3 - h_3}{\psi r_3} \right) - tan^{-1} \left(\frac{m_{30} e_0 - h_0}{\psi r_0} \right) \Bigg]. \end{aligned} \tag{A.9}$$

A.2. Panel Influence Functions for a Doublet Distribution

The edge-based formulation for a panel with constant doublet distribution reads

$$\begin{aligned} \phi_D = \frac{\mu}{4\pi} \Bigg[& tan^{-1} \left(\frac{m_{01} e_0 - h_0}{\psi r_0} \right) - tan^{-1} \left(\frac{m_{01} e_1 - h_1}{\psi r_1} \right) \\ & + tan^{-1} \left(\frac{m_{12} e_1 - h_1}{\psi r_1} \right) - tan^{-1} \left(\frac{m_{12} e_2 - h_2}{\psi r_2} \right) \\ & + tan^{-1} \left(\frac{m_{23} e_2 - h_2}{\psi r_2} \right) - tan^{-1} \left(\frac{m_{23} e_3 - h_3}{\psi r_3} \right) \\ & + tan^{-1} \left(\frac{m_{30} e_3 - h_3}{\psi r_3} \right) - tan^{-1} \left(\frac{m_{30} e_0 - h_0}{\psi r_0} \right) \Bigg]. \end{aligned} \tag{A.10}$$

The velocity components become

$$\begin{aligned} u_D = \frac{\mu}{4\pi}\Bigg[& \frac{\psi(\eta_0-\eta_1)(r_0+r_1)}{r_0r_1\{r_0r_1-[(\xi-\xi_0)(\xi-\xi_1)+(\eta-\eta_0)(\eta-\eta_1)+\psi^2]\}} \\ & + \frac{\psi(\eta_1-\eta_2)(r_1+r_2)}{r_1r_2\{r_1r_2-[(\xi-\xi_1)(\xi-\xi_2)+(\eta-\eta_1)(\eta-\eta_2)+\psi^2]\}} \\ & + \frac{\psi(\eta_2-\eta_3)(r_2+r_3)}{r_2r_3\{r_2r_3-[(\xi-\xi_2)(\xi-\xi_3)+(\eta-\eta_2)(\eta-\eta_3)+\psi^2]\}} \\ & + \frac{\psi(\eta_3-\eta_0)(r_3+r_0)}{r_3r_0\{r_3r_0-[(\xi-\xi_3)(\xi-\xi_0)+(\eta-\eta_3)(\eta-\eta_0)+\psi^2]\}}\Bigg], \end{aligned} \tag{A.11}$$

$$\begin{aligned} v_D = \frac{\mu}{4\pi}\Bigg[& \frac{\psi(\xi_1-\xi_0)(r_0+r_1)}{r_0r_1\{r_0r_1-[(\xi-\xi_0)(\xi-\xi_1)+(\eta-\eta_0)(\eta-\eta_1)+\psi^2]\}} \\ & + \frac{\psi(\xi_2-\xi_1)(r_1+r_2)}{r_1r_2\{r_1r_2-[(\xi-\xi_1)(\xi-\xi_2)+(\eta-\eta_1)(\eta-\eta_2)+\psi^2]\}} \\ & + \frac{\psi(\xi_3-\xi_2)(r_2+r_3)}{r_2r_3\{r_2r_3-[(\xi-\xi_2)(\xi-\xi_3)+(\eta-\eta_2)(\eta-\eta_3)+\psi^2]\}} \\ & + \frac{\psi(\xi_0-\xi_3)(r_3+r_0)}{r_3r_0\{r_3r_0-[(\xi-\xi_3)(\xi-\xi_0)+(\eta-\eta_3)(\eta-\eta_0)+\psi^2]\}}\Bigg], \end{aligned} \tag{A.12}$$

$$\begin{aligned} w_D = \frac{\mu}{4\pi}\Bigg[& \frac{[(\xi-\xi_1)(\eta-\eta_0)-(\xi-\xi_0)(\eta-\eta_1)]\,(r_0+r_1)}{r_0r_1\{r_0r_1-[(\xi-\xi_0)(\xi-\xi_1)+(\eta-\eta_0)(\eta-\eta_1)+\psi^2]\}} \\ & + \frac{[(\xi-\xi_2)(\eta-\eta_1)-(\xi-\xi_1)(\eta-\eta_2)]\,(r_1+r_2)}{r_1r_2\{r_1r_2-[(\xi-\xi_1)(\xi-\xi_2)+(\eta-\eta_1)(\eta-\eta_2)+\psi^2]\}} \\ & + \frac{[(\xi-\xi_3)(\eta-\eta_2)-(\xi-\xi_2)(\eta-\eta_3)]\,(r_2+r_3)}{r_2r_3\{r_2r_3-[(\xi-\xi_2)(\xi-\xi_3)+(\eta-\eta_2)(\eta-\eta_3)+\psi^2]\}} \\ & + \frac{[(\xi-\xi_0)(\eta-\eta_3)-(\xi-\xi_3)(\eta-\eta_0)]\,(r_3+r_0)}{r_3r_0\{r_3r_0-[(\xi-\xi_3)(\xi-\xi_0)+(\eta-\eta_3)(\eta-\eta_3)+\psi^2]\}}\Bigg]. \end{aligned} \tag{A.13}$$

A.3. Near Field Influence Functions

The induced velocities due to a point source are

$$\begin{aligned} u_S &= \frac{\sigma(\xi-\xi_0)A_0}{4\pi[(\xi-\xi_0)^2+(\eta-\eta_0)^2+\psi^2]^{\frac{3}{2}}}, \\ v_S &= \frac{\sigma(\eta-\eta_0)A_0}{4\pi[(\xi-\xi_0)^2+(\eta-\eta_0)^2+\psi^2]^{\frac{3}{2}}}, \\ w_S &= \frac{\sigma(\psi-\psi_0)A_0}{4\pi[(\xi-\xi_0)^2+(\eta-\eta_0)^2+\psi^2]^{\frac{3}{2}}}. \end{aligned} \tag{A.14}$$

The induced velocities due to a point doublet are

$$
\begin{aligned}
u_D &= \frac{3\mu\psi(\xi-\xi_0)A_0}{4\pi[(\xi-\xi_0)^2+(\eta-\eta_0)^2+\psi^2]^{\frac{5}{2}}},\\
v_D &= \frac{3\mu\psi(\eta-\eta_0)A_0}{4\pi[(\xi-\xi_0)^2+(\eta-\eta_0)^2+\psi^2]^{\frac{5}{2}}},\\
w_D &= \frac{-\mu[(\xi-\xi_0)^2+(\eta-\eta_0)^2-2\psi^2]A_0}{4\pi[(\xi-\xi_0)^2+(\eta-\eta_0)^2+\psi^2]^{\frac{5}{2}}}.
\end{aligned}
\tag{A.15}
$$

B. Validation

B.1. Grid Study on a 2-D Hydrofoil

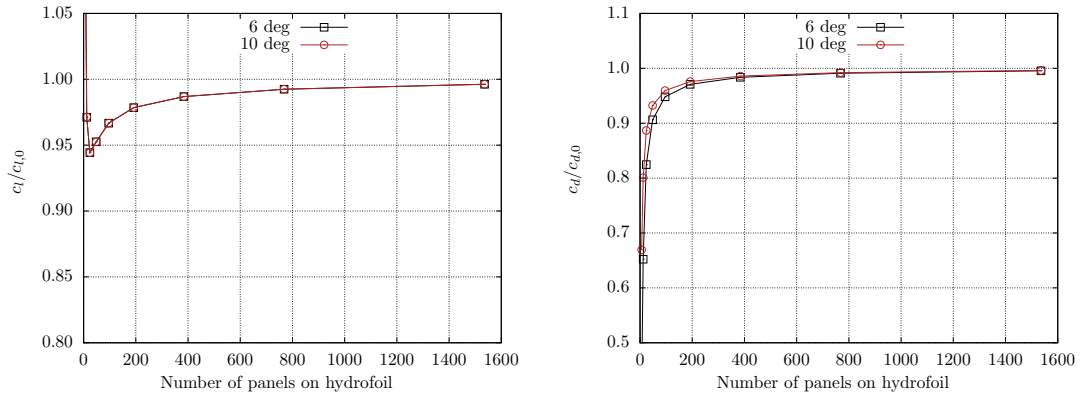

Figure B.1.: Lift (left) and drag (right) forces acting on the NACA0012-hydrofoil for different grid resolutions

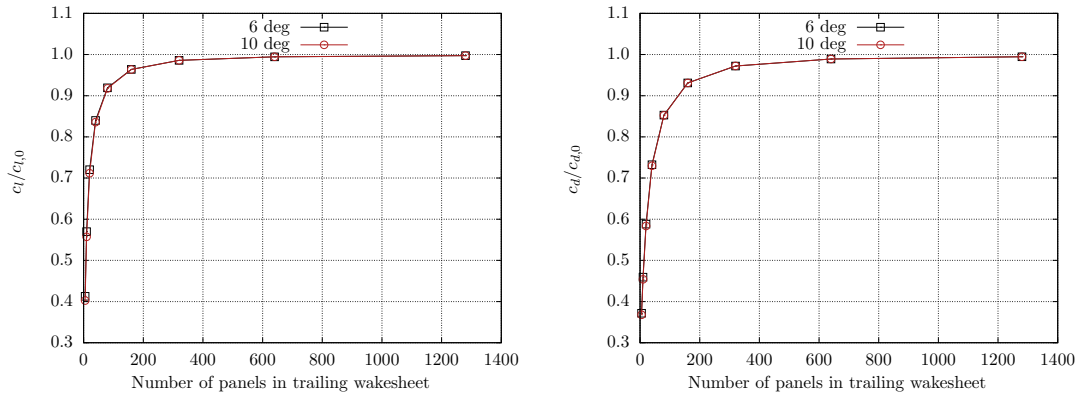

Figure B.2.: Lift (left) and drag (right) forces acting on the NACA0012-hydrofoil for different lengths of the trailing wake sheet

B.2. Propeller Blade Thrust under Consideration of a Wave Potential

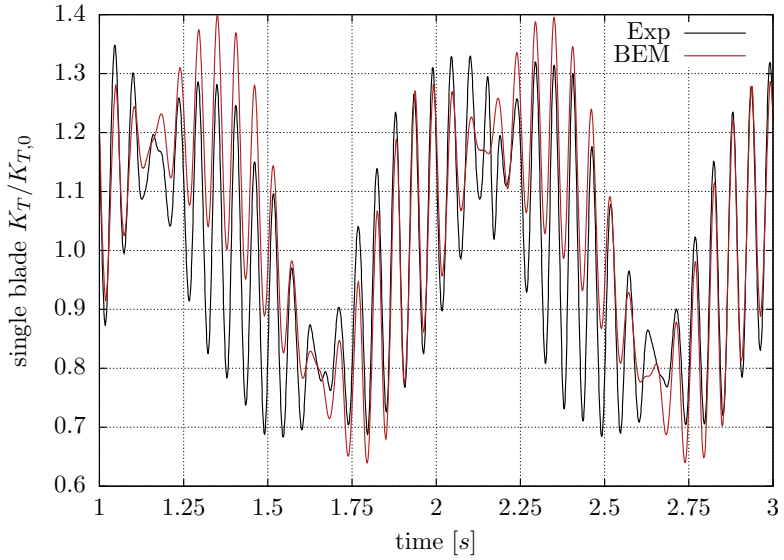

Figure B.3.: Wave 8242 ($J = 0.9, K_{T,0} = 0.0574$)

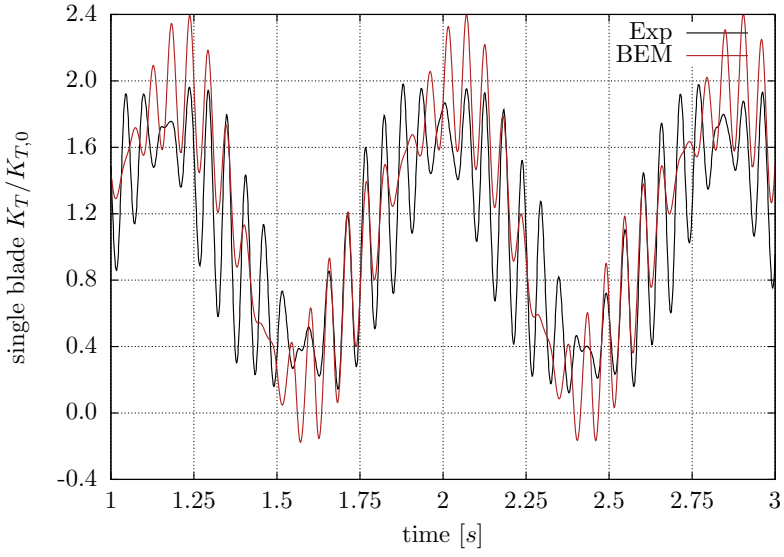

Figure B.4.: Wave 8242 ($J = 1.2, K_{T,0} = 0.0222$)

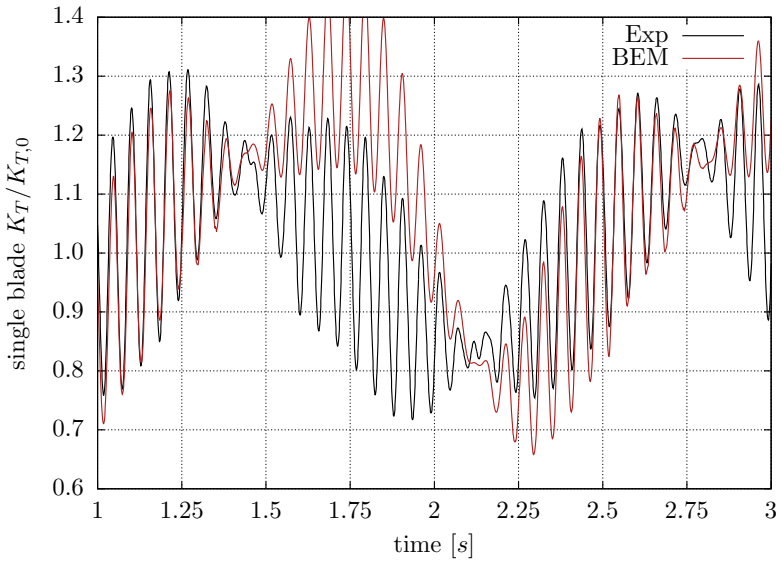

Figure B.5.: Wave 8216 ($J = 0.9, K_{T,0} = 0.0574$)

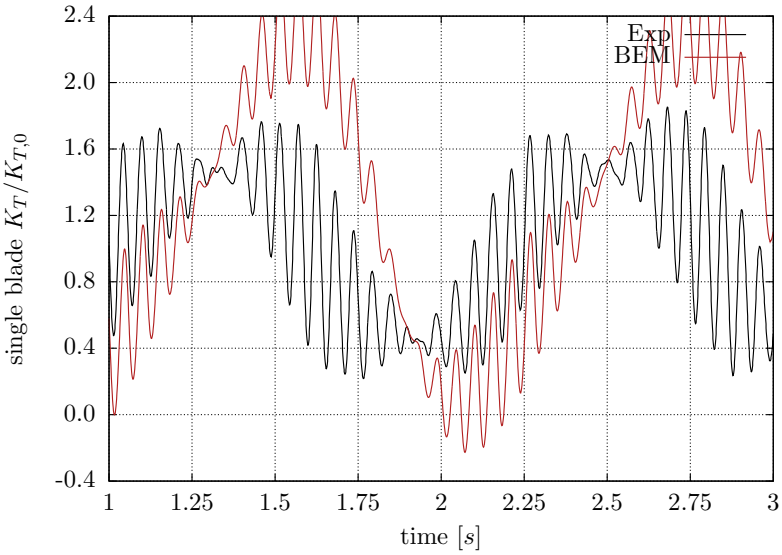

Figure B.6.: Wave 8216 ($J = 1.2, K_{T,0} = 0.0222$)

C. Applications

C.1. Propeller with Wave Influence and Varying Immersion

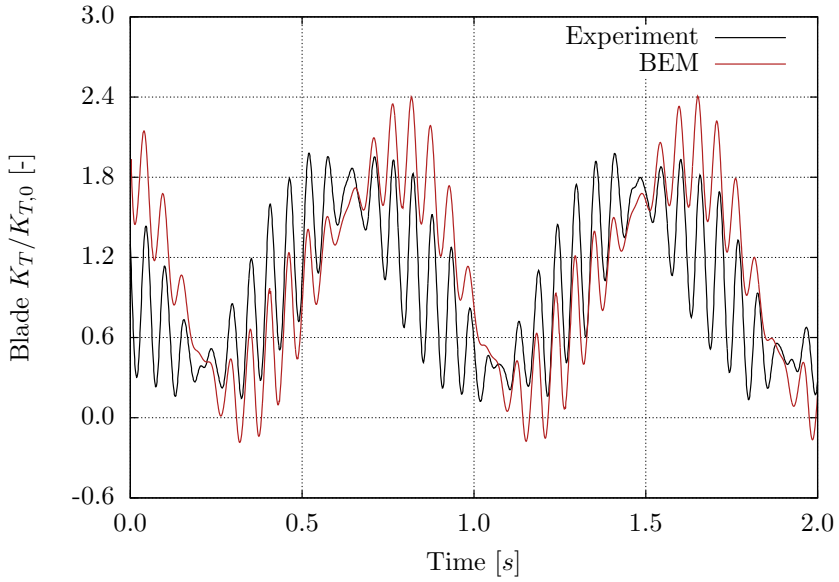

Figure C.1.: Single blade loads for Propeller A
(wave 8242, $H/R = 2.5, J = 1.2, T_w = 2.0s, H_w = 0.3m$)

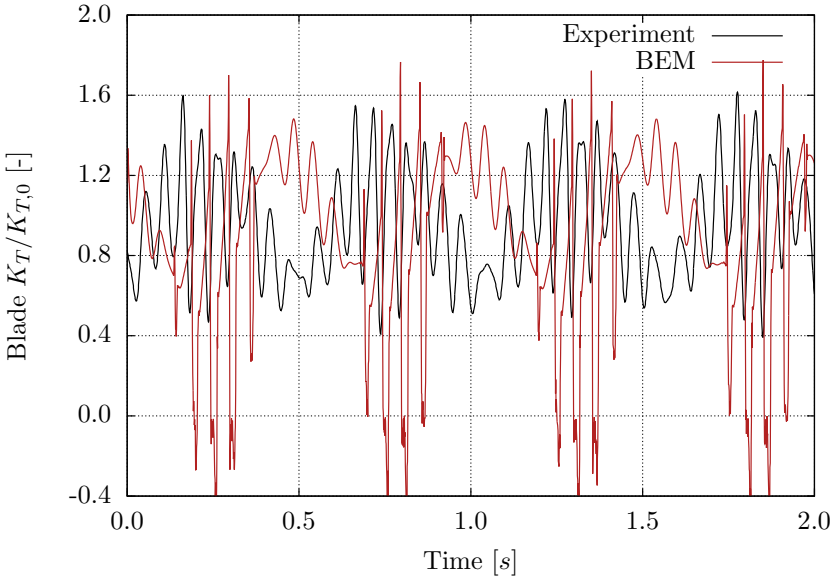

Figure C.2.: Single blade loads for Propeller A
(wave 8211, $H/R = 1.0, J = 1.2, T_w = 1.5s, H_w = 0.1m$)

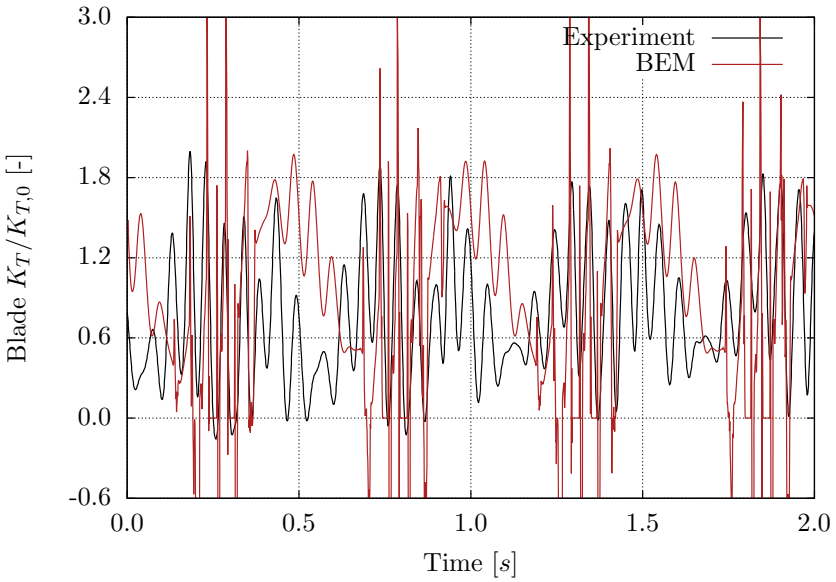

Figure C.3.: Single blade loads for Propeller A
(wave 8221, $H/R = 1.0, J = 1.2, T_w = 1.5s, H_w = 0.2m$)

Bibliography

[1] I. H. Abbott and A. E. von Doenhoff. *Theory of Wing Sections*. Dover Publications Inc., 1959.

[2] M. Abdel-Maksoud, T. Rung, M. Greve, and K. Woeckner-Kluwe. Numerische Untersuchung der Propellerbelastungen im Seegang. Final Report of BMWi 03SX268B, Institute for Fluid Dynamics and Ship Theory, Hamburg University of Technology, 2012. In German.

[3] H. Amini. *Azimuth propulsors in off-design conditions*. PhD thesis, Norwegian University of Science and Technology, Department of Marine Technology, 2011.

[4] H. Amini, L. Sileo, and S. Steen. Numerical calculations of propeller shaft loads on azimuth propulsors in oblique inflow. *Journal of Marine Science and Technology*, 17:403–421, 2012.

[5] H. Amini and S. Steen. Shaft Loads on Azimuth Propulsors in Oblique Flow and Waves. *International Journal of Maritime Engineering*, 153(A1), 2011.

[6] H. Amini, S. Steen, and S. Spence. Shaft Side Force and Bending Moment on Steerable Thrusters in Off-design Conditions. In *Proceedings of International Symposium on practical design of ships and other floating structures*, 2010.

[7] J. D. Anderson. *Fundamentals of Aerodynamics*. Mc Graw Hill, 2001.

[8] S. Bal and S. A. Kinnas. A BEM for the prediction of free surface effects on cavitating hydrofoils. *Computational Mechanics*, 28:260–274, 2002.

[9] W.E. Ball and J.S. Carlton. Podded propulsor shaft loads from free-running model experiments in calm-water and waves. *International Journal of Maritime Engineering*, 2006.

[10] W.E. Ball and J.S. Carlton. Podded propulsor shaft loads from model experiments for berthing manoeuvres. *International Journal of Maritime Engineering*, 2006.

[11] R. Bednarzik. Untersuchungen über die Belastungsschwankungen am Einzelflügel schräg angeströmter Propeller. *Schiffbauforschung*, 8:57–80, 1969.

[12] I.N. Bronstein, K.A. Semendjajew, G. Musiol, and H. Mühlig. *Taschenbuch der Mathematik*. Verlag Harri Deutsch, 2001.

[13] J. Brouwer and G Hagesteijn. Experimental investigation of the effect of waves and ventilation in depressurised conditions on a POD-propeller of a cruise liner model. In *Proceedings of the Third International Symposium on Marine Propulsors*, 2013.

[14] J. Brunswig, M. Manzke, and T. Rung. Explicit and Implicit Coupling Strategies for Overset Grids. In *Proceedings of the 10th Symposium on Overset Composite Grids and Solution Strategies*, 2010.

[15] J. C. Butcher. *The Numerical Analysis of Ordinary Differential Equations*. John Wiley and Sons, 1987.

[16] A. Califano. *Dynamic loads on marine propellers due to intermittent ventilation*. PhD thesis, Norwegian University of Science and Technology, 2010.

[17] A. Califano and S. Steen. Analysis of different propeller ventilation mechanisms by means of RANS simulations. In *Proceedings of the First International Symposium on Marine Propulsors*, 2009.

[18] M. Caponnetto and P. Rolla. Theoretical and practical Experience in developing and Tuning Codes for the Design and Analysis of Propellers. In *Proceedings of CFD'99, The International CFD Conference*, 1999.

[19] M. Caponnetto and P. Rolla. Validation of Panel Methods for Propeller Flow Analysis. In *Proceedings of the Second Numerical Towing Tank Symposium, Rome, Italy*, 1999.

[20] J. S. Carlton. *Marine Propellers and Propulsion*. Butterworth-Heinemann Ltd, 1994.

[21] P.M. Carrica, A. M. Castro, and F. Stern. Self-propulsion computations using a speed controller and a discretized propeller with dynamic overset grids. *Journal of Marine Science and Technology*, 2010.

[22] P.M. Carrica, K.-J. Paik, H.S. Hosseini, and F. Stern. URANS analysis of a broaching event in irregular quartering seas. *Journal of Marine Science and Technology*, (13):395–407, 2008.

[23] Y. H. Chey. The Consistent Second-Order Wave Theory and Its Application to a Submerged Spheroid. *Journal of Ship Research*, 14(1):23–51, 1970.

[24] C. W. Dawson. A Practical Computer Method for Solving Ship-Wave Problems. In *Proceedings of 2nd Conference on Numerical Ship Hydrodynamics*, 1977.

[25] J. H. Duncan. The breaking and non-breaking wave resistance of a two-dimensional hydrofoil. *Journal of Fluid Mechanics*, 126:507–520, 1983.

[26] C. Farell. On the Wave Resistance of a Submerged Spheroid. *Journal of Ship Research*, 1973.

[27] C. Farell and O. Güven. On the Experimental Determination of the Resistance Components of a Submerged Spheroid. *Journal of Ship Research*, 17(2):72–79, 1973.

[28] H. J. Ferziger and M. Peric. *Numerische Strömungsmechanik*. Springer-Verlag, Berlin, 2008.

[29] N. E. Fine. *Nonlinear Analysis of Cavitating Propellers in Nonuniform Flow*. PhD thesis, Massachusetts Institute of Technology, Department of Ocean Engineering, 1992.

[30] U. Göttsche. Implementierung der instationären Randbedingung an der freien Wasseroberfläche in einem Randelementverfahren. Master's thesis, Hamburg University of Technology, 2014. In German.

[31] W. Graff. Über den Einfluß ungleichförmiger Anströmung auf die Schraubenwirkung. *JSTG*, page S. 248, 1935. In German.

[32] L. Greco, F. Salvatore, and F. Di Felice. Validation of a Quasi-potential Flow Model for the Analysis of Marine Propellers Wake. In *Proceedings of the 25th Symposium on Naval Hydrodynamics*, 2004.

[33] D. S. Greeley and J. E. Kerwin. Numerical Methods for Propeller Design and Analysis in Steady Flow. *SNAME Transactions*, 90:415–453, 1982.

[34] N. Gregory and C. L. O'Reilly. Low-Speed Aerodynamic Characteristics of NACA 0012 Aerofoil Section, including the Effects of Upper-Surface Roughness Simulating Hoar Frost. Technical report, Aerodynamics Division, N.P.L., 1970.

[35] M. Greve, K. Wöckner-Kluwe, M. Abdel-Maksoud, and T. Rung. Effiziente Simulation der Schiffspropulsion in regelmäßigen Wellen. *Jahrbuch der Schiffbautechnischen Gesellschaft*, 106:78–85, 2012. In German.

[36] M. Greve, K. Wöckner-Kluwe, M Abdel-Maksoud, and T. Rung. Viscous-Inviscid Coupling Methods for Advanced Marine Propeller Applications. *International Journal of Rotating Machinery*, 2012.

[37] S. T. Grilli. A fully non-linear model for three-dimensional overturning waves over an arbitrary bottom. *International Journal for Numerical Methods in Fluids*, 35:829–867, 2001.

[38] F. Gutsche. Untersuchung von Schiffsschrauben in schräger Anströmung. *Schiffbauforschung*, 3:97–122, 1964. In German.

[39] L. He. *Numerical Simulation of Unsteady Rotor/Stator Interaction and Application to Propeller/Rudder Combination.* PhD thesis, The University of Texas at Austin, 2010.

[40] H. J. Heinke. Investigation about the forces and moments at podded drives. In *Proceedings of the First International Conference on Technological Advances in Podded Propulsion, Newcastle University, UK*, pages 305–320, 2004.

[41] J. L. Hess. Calculation of Potential Flow About Arbitrary Three-Dimensional Lifting Bodies. Technical report, Douglas Aircraft Division, Long Beach, California, 1972.

[42] J. L. Hess and A. M. O. Smith. Calculation of Non-Lifting Potential Flow about arbitrary Three-Dimensional Bodies. Technical report, Douglas Aircraft Division, Long Beach, California, 1962.

[43] J. L. Hess and W. O. Valarezo. Calculation of Steady Flow About Propellers by Means of a Surface Panel Method. In *Proceedings of AIAA 23rd Aerospace Sciences Meeting*, 1985.

[44] C.-Y. Hsin. *Development and Analysis of Panel Methods for Propellers in Unsteady Flow.* PhD thesis, Massachusetts Institute of Technology, 1990.

[45] J. Hundemer. *Entwicklung eines Verfahrens zur Berechnung der instationären potenzialtheoretischen Propellerumströmung.* PhD thesis, Hamburg University of Technology, 2013. In German.

[46] W. H. Isay. Zur Theorie des Propellers mit aus dem Wasser herausschlagenden Flügeln. 1966. In German.

[47] M. F. Islam, A. Akinturk, B. Veitch, and P. Lui. Performance Characteristics of Static and Dynamic Azimuthing Podded Propulsor. In *Proceedings of the First International Symposium on Marine Propulsors*, 2009.

[48] C. E. Janson. *Potential Flow Panel Methods for the Calculation of Free-surface Flows with Lift.* PhD thesis, Chalmers University of Technology, 1997.

[49] G. Jensen. Berechnung der stationären Potentialströmung um ein Schiff unter Berücksichtigung der nichtlinearen Randbedingungen an der Wasseroberfläche. *Schriftenreihe Schiffbau*, No. 484, 1988. In German.

[50] J.M.J. Journée and W.W. Massie. *Offshore Hydromechanics.* Delft University of Technology, 2001.

[51] J. Katz and A. Plotkin. *Low-Speed Aerodynamics*. Cambridge University Press, 2001.

[52] J. E. Kerwin, S. A. Kinnas, J.-T. Lee, and W.-Z. Shih. A Surface Panel Method for the Hydrodynamic Analysis of Ducted Propellers. *SNAME Transactions*, 95:93–122, 1987.

[53] S. A. Kinnas and C.-Y. Hsin. Boundary Element Method for the Analysis of the Unsteady Flow Around Extreme Propeller Geometries. *AIAA Journal*, 30(3):688–696, 1992.

[54] S. A. Kinnas, C.-Y. Hsin, and D. Keenan. A Potential Based Panel Method for the Unsteady Flow Around Open and Ducted Propellers. In *18th Symposium on Naval Hydrodynamics*, 1991.

[55] S. A. Kinnas, H. Lee, and Y. L. Young. Modeling of Unsteady Sheet Cavitation on Marine Propeller Blades. *International Journal of Rotating Machinery*, 9:263–277, 2003.

[56] S. A. Kinnas and Y. L. Young. Modeling of cavitating or ventilated flows using BEM. *International Journal of Numerical Methods for Heat & Fluid Flow*, 13:672–697, 2003.

[57] N. Kornev. *Vorlesungsmanuskript, Propellertheorie*. 2009. In German.

[58] K. Koushan. Dynamics of Ventilated Propeller Blade Loading on Thrusters Due to Forced Sinusoidal Heave Motion. In *Proceedings of the 26th Symposium on Naval Hydrodynamics*, 2006.

[59] K. Koushan, S. J. B. Spence, and T. Hamstad. Experimental Investigation of the Effect of Waves and Ventilation on Thruster Loadings. In *Proceedings of the First International Symposium on Marine Propulsors*, 2009.

[60] K. Koushan, S. J. B. Spence, and L. Savio. Ventilated Propeller Blade Loadings and Spindle Moment of a Thruster in Calm Water and Waves. In *Proceedings of the Second International Symposium on Marine Propulsors*, 2011.

[61] K. Koyama. Comparative Calculations of Propellers by Surface Panel Method. Workshop organized by 20th ITTC Propulsor Committee, Ship Research Institute, Seoul, Korea, 1993.

[62] A. M. Kozlowska, K. Wöckner-Kluwe, S. Steen, T. Rung, K. Koushan, and S. J. B. Spence. Numerical and Experimental Study of Propeller Ventilation. In *Proceedings of the Second International Symposium on Marine Propulsors*, 2011.

[63] S. Krüger. *Vorlesungsmanuskript, Schiffspropeller*. 2005. In German.

[64] L. Larsson, F. Stern, and M. Visonneau, editors. *Gothenburg 2010, A Workshop on Numerical Ship Hydrodynamics*, volume 2, 2010.

[65] J. B. le Rond d'Alembert. Essai d'une nouvelle théorie de la résistance des fluides. 1752. In French.

[66] H. Lee. *Modeling of Unsteady Wake Alignment and Developed Tip Vortex Cavitation.* PhD thesis, The University of Texas at Austin, 2002.

[67] P. Liu, M. Islam, and B. Veitch. Some Unsteady Propulsive Characteristics of a Podded Propeller Unit under Manoeuvering Operation. In *Proceedings of the First International Symposium on Marine Propulsors*, 2009.

[68] M. MackAldener. *Tooth Interior Fatigue Fracture & Robustness of Gears.* PhD thesis, Royal Institute of Technology, Department of Machine Design, 2001.

[69] M. Manzke, J.-P. Voss, and T. Rung. Sub-cycling strategies for maritime two-phase flows. *Notes on Numerical Fluid Mechanics*, 120:237–251, 2012.

[70] L. Morino and C.-C. Kuo. Subsonic Potential Aerodynamics for Complex Configurations: A General Theory. *AIAA Journal*, 12(2):191–197, 1974.

[71] S.-B. Müller, M. Steden, J. Neugebauer, M-F. El-Haddad, and M. Abdel-Maksoud. Comparing a Propeller Model with a Rotating Propeller in an CFD-simulation of the Viscous Flow around a Ship. Technical report, Institute of Ship Technology and Transport Systems, University of Duisburg-Essen, 2006.

[72] R. Muscari and A. Di Mascio. Numerical simulation of the flow past a rotating propeller behind a hull. In *Proceedings of the Second International Symposium on Marine Propulsors*, 2011.

[73] J. N. Newman. Distributions of sources and normal dipoles over a quadrilateral panel. *Journal of Engineering Mathematics*, 20:113–126, 1986.

[74] S.-Y. Ni. *Higher-order panel methods for potential flows with linear or nonlinear free-surface boundary conditions.* PhD thesis, Chalmers University of Technology, 1987.

[75] A. B. Phillips, S. R. Turnock, and M. Furlong. Evaluation of Manoeuvring Coefficients of a Self-Propelled Ship using a Blade Element Momentum Propeller Model Coupled to a Reynolds Averaged Navier Stokes Flow Solver. *Ocean Engineering*, 36:1217–1225, 2009.

[76] G. K. Politis. Simulation of unsteady motion of a propeller in a fluid including free wake modeling. *Engineering Analysis with Boundary Elements*, 28:633–653, 2004.

[77] H. C. Raven. Nonlinear Ship Wave Calculations Using the RAPID Method. In *Proceedings of the 6th international Conference on Numerical Ship Hydrodynamics*, 1994.

[78] H. C. Raven. *A solution method for the nonlinear ship wave resistance problem.* PhD thesis, Technische Universiteit Delft, 1996.

[79] H. E. Saunders. *Hydrodynamics in Ship Design*, volume 1. The Society of Naval Architects and Marine Engineers, 1957.

[80] L. Savio, S. J. B. Spence, K. Koushan, and S. Steen. Full Scale and Model Scale Propeller Ventilation Behind Ship. In *Proceedings of the Third International Symposium on Marine Propulsors*, 2013.

[81] L. Savio and S. Steen. Identification and Analysis of Full Scale Ventilation Events. *International Journal of Rotating Machinery*, 2012.

[82] J. A. Schetz and S. Favin. Numerical Solution for the Near Wake of a Body with Propeller. *Journal of Hydronautics*, Vol. 11, No. 4, 1977.

[83] J. A. Schetz and S. Favin. Numerical Solution of a Body-Propeller Combination Flow Including Swirl and Comparisons with Data. *Journal of Hydronautics*, Vol. 13, No. 2, 1979.

[84] A. Sharma, L. He, and S. A. Kinnas. Numerical Modeling of a Hydrofoil or a Marine Propeller Undergoing Unsteady Motion. In *Proceedings of the Second International Symposium on Marine Propulsors*, 2011.

[85] H. Söding. Towards Fully Non-Linear Floating Body Simulations by a Potential Method. In *Proceedings of the 31st International Conference on Ocean, Offshore and Arctic Engineering*, 2012.

[86] J. A. Sparenberg. On the Potential Theory of the Interaction of an Actuator Disc and a Body. *Journal of Ship Research*, Vol. 16, No. 4, 1972.

[87] J. A. Sparenberg. On the Linear Theory of an Actuator Disc in a Viscous Fluid. *Journal of Ship Research*, Vol. 18, No. 1, 1974.

[88] A. Stück and T. Rung. Adjoint complement to viscous finite-volume pressure-correction methods. *Journal of Computational Physics*, 248:402–419, 2013.

[89] F. Stern, H.T. Kim, V.C. Patel, and H.C. Chen. A Viscous-Flow Approach to the Computation of Propeller-Hull Interaction. *Journal of Ship Research*, Vol. 32, No. 4, 1988.

[90] J. Stoeckert and H. Gatzer. Hydrodynamic effects on the propeller of a ship in regular waves. *Schiffbauforschung*, 26:125–131, 1987.

[91] J. A. Szantyr. Hydrodynamic model experiments with pod propulsor. *Oceanic Engineering International*, 5(2):95–103, 2001.

[92] A. C. Takinaci and M. Atlar. On the importance of boundary layer calculations instead of viscous correction in heavily loaded marine propellers while using a surface panel method. *Journal of Ocean Engineering*, 28:519–536, 2001.

[93] W.-T. Tsai and D. K. P. Yue. Computation of nonlinear free-surface flows. *Annual Review of Fluid Mechanics*, 28:249–278, 1996.

[94] M. Ueno, Y. Tsukada, and K. Tanizawa. Estimation and prediction of effective inflow velocity to propeller in waves. *Journal of Marine Science and Technology*, 18:339–348, 2013.

[95] Y. Uslu and Ş. Bal. Numerical Prediction of Wave Drag of 2-d and 3-d Bodies under or on a Free Surface. Technical report, Delta Marine, Istanbul and Department of Naval Architecture and Marine Engineering, Istanbul Technical University, 2008.

[96] G. Vaz, F. Jaouen, and M Hoekstra. Free-Surface Viscous Flow Computations. Validation of URANS Code FRESCO. In *Proceedings of the 28th International Conference on Ocean, Offshore and Arctic Engineering*, 2009.

[97] V. Vinayan. *A Boundary Element Method for the Strongly Nonlinear Analysis of Ventilating Water-entry and Wave-body Interaction Problems.* PhD thesis, The University of Texas at Austin, 2009.

[98] K. Wöckner-Kluwe. *Evaluation of the unsteady propeller performance behind ships in waves.* PhD thesis, Hamburg University of Technology, 2012.

[99] S. Yakubov, B. Cankurt, T. Maquil, P. Schiller, M. Abdel-Maksoud, and T. Rung. *Advanced Approaches to Cavitation Modelling in Marine Applications.* Number 29 in Computational Methods in Applied Sciences. 2013.

[100] Y. L. Young. *Numerical Modeling of Supercavitating and Surface-Piercing Propellers.* PhD thesis, The University of Texas at Austin, 2002.